

Experimental and Numerical Investigation of the Integrated Solar Combined Cycle

**vom Fachbereich Maschinenbau
der Technischen Universität Darmstadt**

zur Erlangung des akademischen Grades
Doktor–Ingenieur (Dr.–Ing.)

genehmigte DISSERTATION

von

M.Sc. Ayman Lotfy Kabel Temraz

Erstgutachter: Prof. Dr.–Ing. Bernd Epple

Zweitgutachter: Prof. Dr. rer. nat. Amsini Sadiki

Tag der mündlichen Prüfung: 23. 11. 2021

Darmstadt 2021

D 17

Experimental and Numerical Investigation of the Integrated Solar Combined Cycle

Genehmigte Dissertation von M.Sc. Ayman Lotfy Kabel Temraz

Erstgutachter: Prof. Dr.–Ing. Bernd Epple

Zweitgutachter: Prof. Dr. rer. nat. Amsini Sadiki

Tag der mündlichen Prüfung: 23. 11. 2021

Darmstadt, Technische Universität Darmstadt

Dieses Dokument wird bereitgestellt von TUpriints,

E-Publishing-Service der TU Darmstadt

<http://tuprints.ulb.tu-darmstadt.de>

tuprints@ulb.tu-darmstadt.de

URN: [urn:nbn:de:tuda-tuprints-202233](https://nbn-resolving.org/urn:nbn:de:tuda-tuprints-202233)

Jahr der Veröffentlichung der Dissertation auf TUpriints: 2021

Veröffentlicht unter CC BY-SA 4.0 International

<https://creativecommons.org/licenses/>

Preface

The work of the present doctoral thesis “Experimental and Numerical Investigation of the Integrated Solar Combined Cycle” started in November 2018 and was carried out at the Institute of Energy Systems and Technology (EST), Department of Mechanical Engineering, Technical University of Darmstadt. Three years of full-time work and deep research made this work possible. However, this work came out in its final form through the support of many people. One student made a doctoral degree from this thesis, but not alone did him all the work. This thesis is a result of wise supervising, scientific guiding, and loving family support. The main supervision was done by **Prof. Dr.-Ing. Bernd Epple** and the co-supervision was done by **Prof. Dr. rer. nat. Amsini Sadiki**.

A team of qualified supervisors took over the responsibility of guiding me through my work on the doctoral degree. At the head of this team **Prof. Dr.-Ing. Bernd Epple** whose academic experience is greatly appreciated. Thanks go to **Priv.-Doz. Dr.-Ing. habil. Falah Alobaid** for spending much of his valuable time guiding me step by step suggestions and comments in my research. I am especially grateful for the feedback and support of **EST staff** at Technical University of Darmstadt who made my time in the institute a memorable and valuable experience. I am thankful to all engineers and technicians in the ISCC power plant in Kuraymat, Egypt who made my visits to the plant a memorable and valuable experience.

Last but not least, I would like to express my deepest feelings to **my parents** for their continuous encouragement, understanding, and support and **my wife** who endured my stress and provided much-needed support during the research. My god bestows health and happiness to all of them.

I dedicate this work to my lovely **wife** and wonderful **daughters**.

Ayman Temraz

Erklärung

Hiermit erkläre ich, dass ich die vorliegende Arbeit, abgesehen von den in ihr ausdrücklich genannten Hilfen, selbständig verfasst habe.

Darmstadt, den 18. Juni 2021

Ayman Temraz

(Ayman Lotfy Kabel Temraz)

Kurzfassung

Der integrierte solare Kombikreislauf (ISKK) kombiniert die Vorteile erneuerbarer, sauberer Energie mit Gas- und Dampfturbinenkraftwerken (GuD-Kraftwerk). GuD-Kraftwerke sind dank ihrer hohen Effizienz, schneller Startfähigkeit und relativ geringer Umweltbelastung weltweit anerkannte thermische Kraftwerke. Zusätzlich unterstützt ihr flexibler blockbasierter Redispatch den Anteil an erneuerbarer Energie, was zur Reduzierung des Kohlenstoffausstoßes beiträgt. Die ISKK-Kraftwerke kombinieren ein Solarfeld mit einem GuD-Kraftwerk, um den Effizienzgrad von Solarkraftwerken zu erhöhen und gleichzeitig die CO₂-Emissionen von GuD-Kraftwerken zu senken. In dieser Arbeit wurden experimentelle und numerische Untersuchungen des ISKK für ein bestehendes ISKK-Kraftwerk in Kuraymat, Ägypten, durchgeführt. Hierbei wurde zum einen eine numerische Untersuchung durch Energie- und Exergieanalyse und eine dynamische Prozesssimulation durchgeführt. Zusätzlich wurden diese Betrachtungen durch experimentelle Untersuchungen von zweiphasigen dynamische Instabilitäten im Abhitzedampferzeuger (AHDE) ergänzt.

In der Energie- und Exergieanalyse wurden der thermische Gesamtwirkungsgrad und der exergetische Wirkungsgrad jeder Komponente im ISKK-Kraftwerk für unterschiedliche solare Wärmeeinträge und Umgebungstemperaturen berechnet. Die Analyse ergab, dass der exergetische Wirkungsgrad der Anlagenkomponenten seinen niedrigsten Wert im Solarfeld hat, gefolgt von der Brennkammer. Weiterhin nehmen der thermische Wirkungsgrad und der exergetische Wirkungsgrad des ISKK-Kraftwerks insgesamt mit steigender Umgebungstemperatur ab und erreichen ihre höchsten Werte im kombinierten Betriebsmodus. Aufgrund dieser Ergebnisse wurde eine Untersuchung zu den Quellen der Exergievernichtung im Solarfeld durchgeführt. Um die Grenzen und Möglichkeiten von ISKK-Kraftwerken und deren Regelungsstrukturen zu bewerten, wurde anschließend ein anspruchsvolles dynamisches Prozessmodell der Anlage mit der Software APROS entwickelt. Das Modell beschreibt die Anlage mit einem hohen Detaillierungsgrad, einschließlich des Solarfelds, des Abhitzedampferzeugers und der Regelungsstrukturen. Das entwickelte Modell wurde unter Verwendung der betrieblichen Auslegungsdaten abgestimmt und anhand tatsächlicher Messungen validiert. Es wurde eine dynamische Analyse von vier verschiedenen Tagen durchgeführt. Anschließend wurden die Simulationsergebnisse präsentiert und mit den realen Messungen verglichen. Der Vergleich zeigte, dass der Verlauf der realen Messungen mit hoher Genauigkeit vorhergesagt werden konnte. Folglich kann das validierte Modell das dynamische Verhalten des ISKK-Kraftwerks mit einem hohen Grad an Genauigkeit simulieren und bei zukünftigen Planungsentscheidungen berücksichtigt werden.

Schließlich wurden die dynamischen Instabilitäten der Zweiphasenströmung im AHDE untersucht, indem Experimente mit demineralisiertem Wasser in einem Zweiphasenströmungsprüfstand mit einem horizontalen Verdampferrohr durchgeführt wurden. Die experimentellen Ergebnisse für die drei Haupttypen der dynamischen Instabilitäten (Dichtewellenschwingung, Druckabfallschwingung und thermische Schwingung) wurden vorgestellt und im Zeit- und Frequenzbereich verglichen. Die Vergleichsstudie zeigte, dass die Dichtewellenschwingungen einen höheren Frequenzbereich haben, von etwa 0,04 bis 0,1 Hz, verglichen mit den Druckabfallschwingungen, die einen Frequenzbereich von etwa 0,012 bis 0,024 Hz haben. Die Druckabfallschwingungen haben mit ihren niedrigeren Frequenzen im Vergleich zu den

Dichtewellenschwingungen einen stärkeren Einfluss auf die thermischen Schwingungen und erhöhen die Wahrscheinlichkeit des Auftretens eines Rohrbrands, da die Amplitude der Oberflächentemperaturschwingungen entlang des Verdampferrohrs, die mit der Druckabfallschwingungen verbunden sind, bis zu 60 °C erreichte.

Abstract

The Integrated Solar Combined Cycle (ISCC) features the advantages of renewable clean energy with combined cycle. The combined cycle gas turbine (CCGT) power plants are the most recognized thermal power plants for their high efficiency, fast start-up capability and relatively low environmental impact. Moreover, their flexible unit dispatch supports the share of renewable energy, which contributes to carbon mitigation. The ISCC power plants integrate a solar field with a CCGT power plant to increase the efficiency of solar power plants while decreasing the CO₂ emissions of CCGT power plants. In this thesis, experimental and numerical investigations of the ISCC were performed for an existing ISCC power plant in Kuraymat, Egypt. On one hand, energy and exergy analyses as well as dynamic process simulations were carried out. On the other hand, an experimental investigation was performed for two-phase dynamic instabilities in the Heat Recovery Steam Generator (HRSG).

In the energy and exergy analysis, the overall thermal efficiency and the exergetic efficiency of each component in the ISCC power plant were calculated for different solar heat inputs and ambient temperatures. The analysis indicated that the exergetic efficiency of the plant components has its lowest value in the solar field followed by the combustion chamber. Further, the thermal efficiency and the exergetic efficiency of the ISCC power plant as a whole decrease with increasing ambient temperature and have their highest values in the combined cycle regime of operation. Owing to these results, an investigation on the sources of exergy destruction in the solar field was conducted. Then, to evaluate the limitations and capabilities of ISCC power plants and their control structures, a sophisticated dynamic process model of the plant has been developed using APROS software. The model describes the plant with a high level of detail including the solar field, the HRSG, and the control structures. The developed model was initialized using the operational design data and validated using actual measurements. Dynamic analysis of different four days was performed then the simulation results were presented and compared with actual measurements. The comparison showed that the course of the actual measurements could be predicted with high accuracy and the developed model can be considered in future planning decisions.

Finally, the dynamic instabilities of the two-phase flow in the HRSG were investigated by performing experiments using demineralized water in a two-phase flow test rig with a horizontal evaporator tube. The experimental results for the main three types of dynamic instabilities (density wave oscillation, pressure drop oscillation, and thermal oscillation) were presented and compared in time and frequency domains. The comparison study showed that the density wave oscillations (DWOs) have a higher frequencies range, of about 0.04 to 0.1 Hz, compared with the pressure drop oscillations (PDOs), which have a frequencies range of about 0.012 to 0.024 Hz. The PDOs, with their lower frequencies compared to DWOs, have a more significant effect on thermal oscillations and increase the likelihood of tube burnout occurring. Since the amplitude of the surface temperature oscillations along the evaporator tube, associated with the PDOs, reached 60 °C.

Table of Contents

Preface.....	iii
Erklärung.....	v
Kurzfassung	vii
Abstract.....	ix
Table of Contents.....	xi
List of Tables	xv
List of Figures	xvii
Nomenclatures	xxi
Symbols.....	xxi
Greek Symbols.....	xxii
Subscripts.....	xxii
Abbreviations and Acronyms	xxiii
Chapter 1: Introduction.....	1
1.1 Background and Motivation.....	1
1.2 Research Objectives	4
1.3 State of the Art	6
1.3.1 Energy and Exergy Analyses	6
1.3.2 Dynamic Process Simulation	8
1.3.3 Two-phase Flow Dynamic Instabilities	10
1.4 Outline of the Thesis	11
1.5 Publications	12
1.5.1 Publications in International Peer-reviewed Journals:.....	12
1.5.2 Manuscripts for Publication in International Peer-reviewed Journals:.....	12
1.5.3 Publications in Peer-reviewed Conference Proceedings:	12
Chapter 2: Energy and Exergy Analyses of ISCC.....	15
2.1 Introduction	15
2.2 Plant Description	15
2.2.1 Solar Field.....	17
2.2.2 Combined Cycle.....	21
2.3 Thermodynamic Analysis	22
2.3.1 Energy Balance	23

2.3.2	Exergy Analysis	28
2.3.1	The Measurement Devices in the Kuraymat Power Plant	30
2.4	Results and Discussion.....	31
2.4.1	Solar Field Model	31
2.4.2	Solar Conversion Efficiency	36
2.4.3	Exergy Flow Diagram.....	37
2.4.4	Overall Thermal Efficiency of the ISCC Power Plant.....	41
2.4.5	Exergy Destruction in Each Component of the ISCC	41
2.4.6	Exergetic Efficiency of the Main Components of the ISCC.....	43
2.4.7	Exergetic Efficiency of the ISCC Power Plant	45
2.4.8	Investigating the Sources of Exergy Destruction.....	46
Chapter 3: Dynamic Process Simulation of ISCC		49
3.1	Introduction	49
3.2	Mathematical Modelling	50
3.2.1	Gas Turbine Simulation	54
3.2.2	HRSG Simulation	55
3.2.3	Solar Field Simulation	60
3.2.4	Dynamic Boundary Conditions.....	63
3.3	Results and Discussion.....	64
3.3.1	Model Tuning.....	64
3.3.2	Dynamic Model Validation.....	66
Chapter 4: Experimental Investigation of Dynamic Instabilities in HRSG.....		73
4.1	Introduction	73
4.2	Technical Fundamentals.....	74
4.3	Dynamic Instabilities Mechanisms	76
4.3.1	Density Wave Oscillations.....	77
4.3.2	Pressure Drop Oscillations.....	78
4.3.3	Thermal Oscillations	80
4.4	Characteristic Pressure Curves.....	80
4.5	Characterization of the Developed Test Rig	81
4.5.1	Design of Evaporator Tube	86
4.5.2	The Orientation of the Heated Test Tube	87
4.5.3	Modes of Operation	88
4.5.4	The Test Rig Instrumentation	89

4.6	Results and Discussion.....	89
4.6.1	Density Wave Oscillation	90
4.6.2	Pressure Drop Oscillation	94
4.6.3	Thermal Oscillation	98
Chapter 5: Conclusion and Outlook.....		101
5.1	Energy and Exergy Analysis	101
5.2	Dynamic Process Simulation	102
5.3	Experimental Investigation of the Two-phase Flow Dynamic Instabilities in the HRSG 103	
5.4	Outlook.....	103
Appendix A.....		105
A.1	The Experimental Results of the Second DWO.....	105
A.2	The Experimental Results of the Second PDO	109
A.3	The Experimental Results of the Second Thermal Oscillation	113
Bibliography		115

List of Tables

Table 2.1 The solar field design parameters [25], [26], [64]	17
Table 2.2 The main specifications of the one-axis parabolic trough collectors in Kuraymat ISCC power plant.....	19
Table 2.3 Therminol VP-1 main specifications [74].....	20
Table 2.4 Typical optical parameters and correction values for the solar field [78].....	26
Table 2.5 Coefficients for receiver heat loss with vacuum annulus.....	27
Table 2.6 Definitions of the exergy destruction and second law efficiency	29
Table 2.7 Plant measurement devices and their accuracy	31
Table 2.8 Exergy rates and other properties at various locations of ISCCS, state numbers refer to Figure 2.4	37
Table 2.9 Exergy, percent of exergy destruction and the second law efficiency of different components of the ISCC	40
Table 3.1 Nets structure and functions of the ISCC model.....	54
Table 3.2 Initialization of the HRSG high-pressure heating modules	57
Table 3.3 Initialization of the HRSG low-pressure heating modules	59
Table 3.4 The solar field design parameters [81],[65]	60
Table 3.5 The specifications of the HTF heat exchangers	62
Table 3.6 Reference steady-state cases description (operational design data).....	65
Table 3.7 Comparison between the simulation results and the operational design data.....	65
Table 4.1 Data of the reference HRSG (provided to TU Darmstadt by Doosan)	86
Table 4.2 The values of the dimensionless numbers.....	87
Table 4.3 Characteristics of the developed test rig	87
Table 4.4 The accuracy of the test rig measurement devices.....	89

List of Figures

Figure 1.1 Layout of an ISCC power plant	3
Figure 2.1 Schematic diagram of the Kuraymat ISCC power plant	16
Figure 2.2 Main components of the SKAL-ET collector [71]	18
Figure 2.3 Layout of the HRSG of Kuraymat ISCC power plant.....	22
Figure 2.4 A flow diagram of the Kuraymat ISCC power plant with state points illustration	24
Figure 2.5 The row shading that occurs during tracking of solar collectors from early to mid-morning [77]	25
Figure 2.6 HCE end loss [17].....	25
Figure 2.7 DNI measured at Kuraymat ISCC power plant on June 21, 2011; September 21, 2011, and December 21, 2011.	32
Figure 2.8 Measured and predicted thermal output from the solar field for (a) June 21, 2011, (b) September 21, 2011 and (c) December 21, 2011.	32
Figure 2.9 Rates of heat absorption and heat loss from the solar field for (a) June 21, 2011, (b) September 21, 2011, (c) December 21, 2011.....	33
Figure 2.10 The value of $\cos \theta$ on June 21, September 21, and December 21.	34
Figure 2.11 Solar field thermal power output vs. DNI.	34
Figure 2.12 Solar field thermal efficiency vs. DNI.....	35
Figure 2.13 Solar field thermal power output vs. incidence angle.	35
Figure 2.14 Solar field thermal efficiency vs. incidence angle.....	36
Figure 2.15 Solar radiation-to-electricity efficiency of the Kuraymat ISCC at different ambient temperatures for solar thermal heat input	36
Figure 2.16 Solar thermal-to-electricity efficiency of the Kuraymat ISCC at different ambient temperatures for solar thermal heat input	37
Figure 2.17 The T-S diagram for the Rankine cycle of the Kuraymat ISCC power plant	39
Figure 2.18 Exergy flow diagram, given as the percentage of total exergy input for the ISCCS.....	40
Figure 2.19 The overall thermal efficiency of the power plant at different ambient temperatures for different solar heat inputs.....	41
Figure 2.20 Exergy destruction in each component of the ISCC to the total exergy destruction of the plant at different ambient temperatures for solar heat input equal to 0 MW	42
Figure 2.21 Exergy destruction in each component of the ISCC to the total exergy destruction of the plant at different ambient temperatures for solar heat input equal to 50 MW	42

Figure 2.22 Exergy destruction in each component of the ISCC to the total exergy destruction of the plant at different ambient temperatures for solar heat input equal to 75 MW	43
Figure 2.23 Exergetic efficiency of different components of the ISCC at different ambient temperatures for solar heat input equal to 0 MW	44
Figure 2.24 Exergetic efficiency of different components of the ISCC at different ambient temperatures for solar heat input equal to 50 MW	44
Figure 2.25 Exergetic efficiency of different components of the ISCC at different ambient temperatures for solar heat input equal to 75 MW	45
Figure 2.26 ISCC power plant exergetic efficiency at different ambient temperatures for different solar heat inputs	46
Figure 3.1 Schematic of the gas turbine net in APROS.....	55
Figure 3.2 Schematic of the HRSG net in APROS.....	56
Figure 3.3 The HP drum level controller	58
Figure 3.4 Schematic of the solar field net in APROS	61
Figure 3.5 The HTF flow rate control circuit	63
Figure 3.6 The rates of heat absorption from the solar field for four days: (a) 20.07.2013, (b) 21.07.2013, (c) 30.08.2013, (d) 04.09.2013.....	67
Figure 3.7 The feedwater mass flow rate for four days: (a) 20.07.2013, (b) 21.07.2013, (c) 30.08.2013, (d) 04.09.2013	67
Figure 3.8 The steam mass flow rate for four days: (a) 20.07.2013, (b) 21.07.2013, (c) 30.08.2013, (d) 04.09.2013.....	68
Figure 3.9 The steam pressure before the steam turbines for four days: (a) 20.07.2013, (b) 21.07.2013, (c) 30.08.2013, (d) 04.09.2013.....	69
Figure 3.10 The steam temperature before the steam turbines for four days: (a) 20.07.2013, (b) 21.07.2013, (c) 30.08.2013, (d) 04.09.2013.....	70
Figure 3.11 The electrical power output of the ISCC power plant for four days: (a) 20.07.2013, (b) 21.07.2013, (c) 30.08.2013, (d) 04.09.2013	70
Figure 4.1 Flow patterns in the horizontal heated pipe [105]	75
Figure 4.2 Flow pattern for water leaving the evaporator tube with various mass flow rates [106]	75
Figure 4.3 Flow map for the horizontal heated pipe by [107]	76
Figure 4.4 Static vs. dynamic instabilities	76
Figure 4.5 Density wave oscillations [106]	78
Figure 4.6 Pressure drop oscillations [106]	79
Figure 4.7 Measured pressure drop for water through the evaporator tube [106]	81
Figure 4.8 Process and instrumentation diagram of the developed test rig	83

Figure 4.9 CAD model of the developed test rig	84
Figure 4.10 The GUI of the two-phase flow test rig developed by the LabVIEW program	85
Figure 4.11 The internal characteristic curve of the evaporator tube	90
Figure 4.12 The variation of the inlet mass flow rate of the evaporator tube during the DWO ...	91
Figure 4.13 The variation of the pressure drop in the evaporator tube during the DWO	91
Figure 4.14 The variation of the inlet mass flow rate of the evaporator tube during the DWO in the frequency domain.....	92
Figure 4.15 The variation of the pressure drop in the evaporator tube during the DWO in the frequency domain.....	93
Figure 4.16 The variation of the pressure drop in the evaporator tube during the PDO.....	94
Figure 4.17 The variation of the inlet mass flow rate of the evaporator tube during the PDO.....	95
Figure 4.18 The variation of the pressure drop in the evaporator tube during the PDO in the frequency domain.....	96
Figure 4.19 The variation of the inlet mass flow rate of the evaporator tube during the PDO in the frequency domain.....	97
Figure 4.20 The variation of the surface temperature along the evaporator tube during the DWO	98
Figure 4.21 The variation of the surface temperature along the evaporator tube during the PDO	99
Figure A.1 The variation of the inlet mass flow rate of the evaporator tube during the second DWO	105
Figure A.2 The variation of the pressure drop in the evaporator tube during the second DWO	106
Figure A.3 The variation of the inlet mass flow rate of the evaporator tube during the second DWO in the frequency domain.....	107
Figure A.4 The variation of the pressure drop in the evaporator tube during the second DWO in the frequency domain.....	108
Figure A.5 The variation of the inlet mass flow rate of the evaporator tube during the second PDO	109
Figure A.6 The variation of the pressure drop in the evaporator tube during the second PDO..	110
Figure A.7 The variation of the inlet mass flow rate of the evaporator tube during the second PDO in the frequency domain.....	111
Figure A.8 The variation of the pressure drop in the evaporator tube during the second PDO in the frequency domain.....	112

Figure A.9 The variation of the surface temperature along the evaporator tube during the second DWO.....	113
Figure A.10 The variation of the surface temperature along the evaporator tube during the second PDO	114

Nomenclatures

Symbols

A	Area	[m ²]
a, b	Constants	[-]
BelShad	losses from shading of ends of HCEs due to bellows	[-]
D	Diameter	[mm]
EnvTrans	The transmissivity of the glass envelope	[-]
f	Focal length of the collectors	[m]
G	Mass flux	[kg/s·m ²]
GeoAcc	Geometric accuracy of the collector mirrors	[-]
h	Specific enthalpy	[kJ/kg]
HCEabs	the absorptivity of the HCE selective coating	[-]
HCEdust	losses due to shading of HCE by dust on the envelope	[-]
HCEmisc	a miscellaneous factor to adjust for other HCE losses	[-]
h _{fg}	Specific enthalpy of vaporization	[kJ/kg]
H _v	Fuel heating value	[kJ/kg]
İ	Rate of exergy destruction	[MW]
L	Length	[m]
MirCln	Mirror cleanliness	[-]
MirRef	Mirror reflectivity	[-]
ṁ	Mass flow rate	[kg/s]
N _{collectors}	Number of the solar field collectors	[-]
N _{sub}	Subcooling number	[-]
p	Pressure	[bar]
N _{pch}	Phase change number	[-]
Q̇	Heat flow rate	[MW]
Q̇ _{abs}	Rate of heat absorbed from the solar radiation per unit Area	[W/m ²]
Q̇ _{SF}	Rate of heat addition to the ISCC from the solar field	[MW]
ReHL	heat loss from the surface of the receiver per unit Area	[W/m ²]
Re _i	Reynolds number	[-]
s	Specific entropy	[kJ/kg·K]
T	Temperature	[°C]
TrkTwstErr	Twisting and tracking error associated with the collector	[-]

u	Velocity	[m/s]
W	Collector aperture width	[m]
\dot{W}	Power output	[MW]
$\dot{W}_{\text{net,out}}$	Net power output of the power plant	[MW]
$\dot{X}_{\text{cycle,in}}$	Total rate of exergy input to the power plant	[MW]
\dot{X}_a	Rate of exergy of the air after the compressor	[MW]
\dot{X}_b	Rate of exergy of the exhaust gases after the combustor	[MW]
\dot{X}_c	Rate of exergy of the exhaust gases after the gas turbine	[MW]
\dot{X}_{heat}	Rate of exergy transfer by heat	[MW]
\dot{X}_{work}	Rate of exergy transfer by work	[MW]

Greek Symbols

α	Directly proportional	[-]
δ	Declination angle	[degree]
Δ	Difference	[-]
ζ	The ratio of chemical exergy and the net calorific value [-]	[-]
η	Efficiency [-]	[-]
θ	Incidence angle	[degree]
θ_z	Zenith angle	[degree]
μ	Dynamic viscosity	[kg/m·s]
ρ	Density	[kg/m ³]
Σ	Summation operator	[-]
X	Exergy	[kJ]
Ψ	Specific exergy	[kJ/kg]
ω	Hour angle	[degree]

Subscripts

amb	Ambient
av	Average
CP	Condensate pump
e	Exit
elec	Electric
f	Liquid

FWP	Feed water pump
g	Vapor
GT	Gas turbine
i	Inner
in	Inlet
inc	Incidence
o	The dead state
s	Source
SF	Solar field
SFHEX	Solar field heat exchanger
ST	Steam turbine

Abbreviations and Acronyms

APROS	Advanced PROcess Simulation software
ASPEN HYSYS	Chemical process simulation software
CAD	Computer-Aided Design
CC	Combustion Chamber
CCGT	Combined Cycle Gas Turbine
CSP	Concentrated Solar Power
CSPP	Concentrated Solar Power Plant
DAQ	Data Acquisition
DNI	Direct Normal Irradiance
DWO	Density Wave Oscillation
ECO	Economizer
EVAP	Evaporator
FG	Flue Gases
FW	Feedwater
FWP	Feedwater Pump
G	Generator
GT	Gas Turbine
GEF	Global Environmental Facility

GUI	Graphical User Interface
HCE	Heat Collection Element
HRSG	Heat Recovery Steam Generator
HTF	Heat Transfer Fluid
HP	High-Pressure
HPST	High-Pressure Steam Turbine.
IAM	Incidence Angle Modifier
ISCC	Integrated Solar Combined Cycle
ISCCS	Integrated Solar Combined Cycle System
LP	Low-Pressure
LPST	Low-Pressure Steam Turbine
LEC	Levelized Energy Cost
MATLAB	Matrix Laboratory
MENA	Middle East North Africa nations
MST	Main Supply Tank
NI	National Instrument
NREA	New and Renewable Energy Authority
NREL	National Renewable Energy Laboratory
OFT	Overflow tank
PDO	Pressure Drop Oscillation
PI	Proportional-Integral
PNID	Process and Instrumentation Diagram
PTC	Parabolic Trough Collector
RTD	Resistance Temperature Detector
SAM	System Advisory Model
ST	Steam Turbine
SEGS	Solar Energy Generation Systems
SH	Superheater
SRC	Solar Rankine Cycle
SDCC	Solar Driven Combined Cycles
SCA	Solar Collector Assembly
SCE	Solar Collector Element.

ST	Steam Turbine
TRNSYS	TRaNsient SYstem Simulation program

Chapter 1: Introduction

In this chapter, the background and motivation for investigating the performance of integrated solar combined cycle (ISCC) power plants are presented. Furthermore, the objectives of the study and the methodology applied are explained. This is followed by an overview of historical research and its state of the art, categorized by the methodology applied in this thesis. Finally, the outlines of the thesis and the author's publications in international peer-reviewed journals and conferences are presented.

1.1 Background and Motivation

Continuous technical progress in recent decades has significantly shaped the way of life and the demands of the population, especially in industrial nations. However, this progress is also accompanied by accelerating demand for energy, as both small appliances and large industrial plants are frequently powered by electrical energy. Electricity demand is growing worldwide faster than any other form of energy consumption as a result of increasing population growth, digitalization, e-mobility and sector coupling.

The share of electricity produced from thermal power plants continues to dominate total electricity production worldwide, thermal power plants share more than 80% of electricity production worldwide and are set to remain a major player for the foreseeable future [1]. Thermal power generation includes electricity produced from coal (38.2%), natural gas (23.1%), nuclear (10.2%), petroleum (2.9%), and non-renewables and waste (9.8%) [1].

In this regard, reducing the amount of fossil fuel burned and consequently lowering emissions of carbon dioxide, a greenhouse gas associated with global warming, is on the social and political agenda. The increasing number of devastating floods, droughts and hurricanes in recent decades, which according to climate researchers are partly due to man-made global warming, are urging the international community to take measures to protect the climate and the environment. Thirteen of the 14 warmest years on record have all happened this century. Recent analyses show that current action by governments around the world is not sufficient to prevent warming of more than 3 °C by the end of this century, with rises of 4 °C or even 6 °C not excluded [2]. Hence, with a critical view of these serious circumstances, it seems necessary to resort to other means of power generation. Therefore, the increasing use of renewable energy sources as a supplement to conventional energy supplies is gaining importance.

Energy from renewables is expected to make a significant contribution to the carbon mitigation required for achieving the European and global climate change mitigation goal of keeping the maximum average global temperature rise below 1.5 °C [3]. The European Union and their member states intend to promote the expansion of renewable energy sources of at least 32% of the gross final energy consumption by 2030 because energy from renewables will play a key role for the years after 2020. These actions mainly include the promotion of renewable energy sources for power generation with possible electrification of the heating and transport sectors. However, the levelized cost of renewable energy should be less expensive in order to be competitive with other power generation technologies. Therefore, it is of increasing importance to advance the processing

of renewable energies like solar energy as well as the development of modern types of power plants. Solar energy has many technologies; one of the promising technologies is the concentrated solar power (CSP) technology which operates using concentrated solar collectors to get higher temperatures than other technologies. The options for thermal energy storage, hybrid system operation and the possible use as an efficient combined heat and power plant make CSP the most flexible renewable electricity generation technology.

CSP technology is one of the solar energy technologies that use mirrors or lenses, or a combination of both, to concentrate the sun's rays and convert their energy into very high-temperature heat to produce steam to drive steam turbines that generate electricity. The concentrated solar power plant (CSPP) produce energy using steam, similarly to conventional steam power plants with emission-free, by collect direct solar radiation to get heat instead of nuclear or fossil fuels. For sunny regions, solar thermal power plants, e.g. CSPPs, are an option for generating electricity with renewable energies.

Many types of concentrating solar collectors have been developed to be used in CSP technology like parabolic troughs, parabolic dishes, linear Fresnel reflectors and power towers. Parabolic trough collectors (PTCs) have been used in many CSPPs. Parabolic trough power plants are ready for use today because they were tested on a commercial basis [4]. This has been proven in California since 1985 by the parabolic trough power plant, which has succeeded in commercial operation and generated electricity using a steam turbine connected to a generator as conventional power plants. In the Mojave Desert (California, USA), nine parabolic trough power plants have been generating solar power since the 1980s. These solar electricity generation power plants produce a total of 354 MW of power [5]. They have demonstrated a long-term availability of around 99%. The reliability of the components and the low operating and maintenance costs have also been proven over many years. However, renewables normally provide fluctuating feed-in into the electricity grid so that energy reserves, e.g., energy storage systems or conventional thermal power plants are required to achieve a balance between current electricity supply and demand. CSP technologies can be coupled with heat storage technologies to produce electricity on demand regardless of irradiation conditions, but heat storage technologies are not yet affordable.

Solar thermal technologies can also be integrated into conventional thermal power plants to increase the profitability of the CSPPs. This integration in fossil thermal power plants is an economically interesting option for the prompt implementation of CSP technology while maintaining a high level of security of supply. Retrofitting thermal power plants for flexible operation can contribute to the integration of renewable energies into a modern power supply system. The world society actively supports measures aimed at facilitating a flexible and low-carbon energy economy.

The retrofitting of existing fossil-fuel power plants as part of their modernization to solar hybrid power plants is ideal. The combined cycle gas turbine (CCGT) power plants are the most recognized conventional thermal power plants for their high efficiency, fast start-up capability, and relatively low environmental impact. Besides, its flexible unit dispatch supports the increase in the share of renewable feed-in. The high thermodynamic efficiency of the CCGT power plants sways the world to widely construct these power plants. The modern concept of the CCGT power plant is mainly driven by the increasing performance of the gas turbine. Today, a 1 + 1 arrangement of gas turbine and steam turbine in combination with a triple-pressure heat recovery steam

generator (HRSG) is state of the art [20]. According to the International Energy Agency (IEA) in 2018, gas-fired power generation accounted for approximately 24% of the total share of worldwide electricity generation, dominated by CCGT power plants. On the one hand, the nominal process efficiency of a large-scale CCGT power plant with a net electrical power of about 605 MW per unit can reach levels greater than 60% [3]–[6]. On the other hand, state-of-the-art coal-fired power plants reach a net thermal process efficiency of about 46% with single reheat and several low-pressure and high-pressure feedwater preheaters [7]. The CCGT power plants have the advantage of absorption of the waste heat in the flue gas of a gas turbine using a HRSG installed downstream of the gas turbine. The integration of solar energy into these plants technology is an effective method for cleaner and cheaper power generation. It contributes to reducing the electricity generation costs from solar energy technologies by using the already existing components such as the steam turbine, generator, pumps and condenser.

The integration of the CSP technology within a CCGT power plants are known as an integrated solar combined cycle (ISCC). ISCC power plants consist of a solar field with a solar steam generator integrated into a conventional CCGT power plant as shown in **Figure 1.1**. This ISCC is a hybrid power technology that combines a CSPP with a modern CCGT power plant.

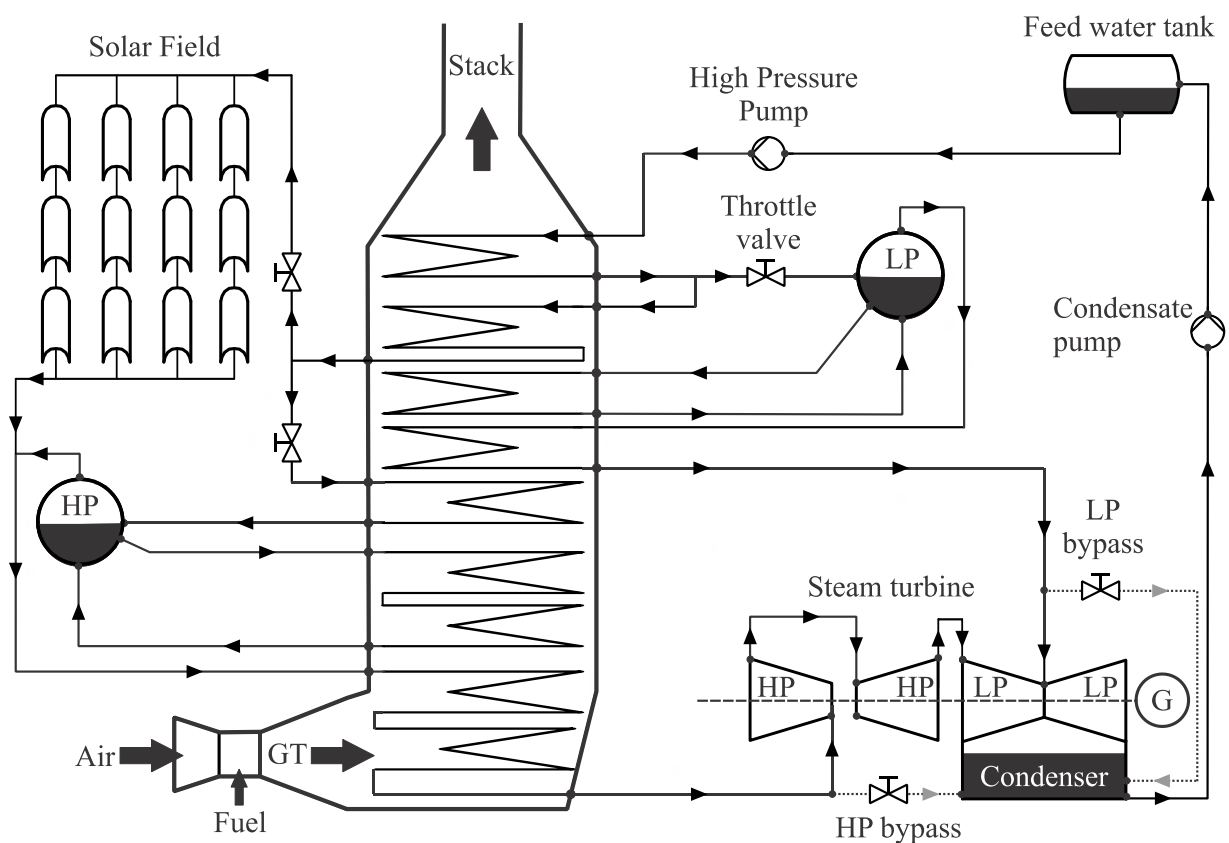


Figure 1.1 Layout of an ISCC power plant

There are two major benefits of this technology compared to a stand-alone CSPP. Since the CCGT power plant can operate continuously, the start-up and shut-down losses of the solar plant can be minimized, and the incremental costs for a larger steam turbine in the CCGT power plant are less than the overall unit costs in a CSPP. ISCC power plants feature the advantages of renewable clean energy with efficient CCGT power plants through increasing the efficiency of solar power plants

while decreasing the CO₂ emissions of the CCGT power plants. ISCC system improves the solar-to-electricity conversion efficiency [6] and the economic feasibility of the CSPPs. In addition, it increases the solar share, which leads to saving the fossil fuels used in these plants [7] while decreasing the CO₂ emissions [8]. Also, the ISCC power plants assure the delivery of the required electricity to the grid regardless of solar radiation conditions; unlike the stand-alone solar power plants.

The ISCC power plants were initially proposed by Luz Solar International after studying them since the 1990s [7]. From 1990 to 2000, the building of new parabolic trough power plants has stopped due to different economic reasons. In 2000, the Global Environment Facility decided to grant up to \$50 million for the construction of four ISCC power plants in some developing countries with high solar irradiation, most of them located in the Middle East region [9]. This decision increased interest in CSP technologies again, especially in parabolic trough collectors [10]. The ISCC power plants could play a role as a major contribution to meeting energy demand safely and reliably. The solar integration technology helps to adapt and retrofit the existing power plants instead of developing new ones. However, it has challenges in the design and optimization of retrofitting CCGT power plants.

The ISCC power plants have several configurations to reduce the cost and efficiency of solar integration into power generation. These configurations can be classified according to the utilization of absorbed solar heat, at any stage of heating, as it can be used for:

- Evaporating a part of the high-pressure steam.
- Preheating with the previous layout.
- Superheating section with the evaporation instead of preheating section.
- Evaporation section in addition to both preheating and superheating.

The ISCC can be configured by preheating the air with solar energy before entering the combustor which is called a ‘solarized’ gas turbine plant [11] or by reheating the gas turbine exhaust gases in a solar receiver before entering the HRSG [12]. Results of studying the configurations by mean of exergy analysis showed that the best choice is the utilization of solar heat in evaporation a part of the high-pressure steam configuration, as shown in **Figure 1.1**, due to its higher thermal efficiency than the others and its low irreversibility at the HRSG [7],[13].

The retrofitting of CCGT power plants to ISCC power plants with parabolic troughs represents a viable option to achieve relatively low-cost capacity expansion and strong knowledge building regarding concentrating solar power [14]. The costs of replacing the steam turbine with a greater one when using solar energy with an existing CCGT power plant are lower than the overall unit cost for a solar-only plant. And this will give the opportunity for improvement of the CSP technology.

1.2 Research Objectives

The purpose of the research presented in this thesis is to investigate the thermodynamic performance of the ISCC power plants. This task was undertaken through numerical and experimental research methodology.

First, the numerical investigation of the ISCC was implemented through:

1. Performing an energy and exergy analysis for the ISCC.
2. Developing and validating a sophisticated dynamic process model representing the Kuraymat ISCC power plant in Egypt using APROS software.

Second, the experimental investigation was implemented by carrying out experiments for the two-phase flow dynamic instabilities that may occur in the HRSG of the ISCC.

The conventional energy analysis (based on the first law analysis) gives the quantitative not the qualitative assessment of the various losses occurring in the components of such solar thermal system. Therefore the exergy analysis (based on the second law analysis) should be used to get a complete assessment of the various losses qualitatively as well as quantitatively. So, the exergy analysis complements the energy analysis not to replace. Exergy analysis pinpoints the location of the wasted exergy, in addition, to quantify the collection and useful consumption of exergy, which leads the way to improve the system. Energy and exergy analysis of the ISCC power plant is carried out to determine the plant performance and indicates sites of primary exergy destruction. Exergy-based performance analysis is the performance study of the system based on the second law of thermodynamics that overcomes the limit of studying the system based on the first law of thermodynamics. It assesses the magnitude and percentage of exergy destruction in each part of the system. Then, a sophisticated dynamic process model representing the Kuraymat ISCC power plant in Egypt was developed using APROS software. All processes and automation are modelled according to the specification of the reference plant. Moreover, actual measurements from the reference plant are used for model validation. The study includes measurement validation to analyze the influence of modelling assumptions on simulation results.

Since the gas turbine is an inherently flexible component, studies in the literature were largely focused on the dynamic response of the water / steam bottoming cycle. In HRSGs, demineralized water is vaporized using the hot exhaust gases from the upstream gas turbine, thus driving the steam turbine. There are two different concepts for HRSGs. On the one hand, there is the vertical HRSG with horizontal tubes, and on the other hand the horizontal HRSG with vertical tubes. Depending on the construction and the working principle of the HRSG, there are more or less prone to so-called flow instabilities. And concerning climate protection, it is a significant task to develop evaporation processes in the HRSGs, because this can increase the efficiency of the power plants and thus reduce CO₂ emissions. It is important to understand occurring instabilities to prevent unstable and unsafe operating conditions during the evaporation process to increase the service life of the HRSGs. In order to achieve a better understanding of this evaporation process, research is being conducted in the areas of heat transfer, pressure drops, and instability phenomena in two-phase (water-steam) flow. Therefore, an experimental investigation for the pressure drop and dynamic instabilities in evaporation processes using demineralized water as the working fluid in a horizontally oriented heated tube at low pressure are presented. The main focus lies on two-phase flow instabilities, in particular density wave oscillation (DWO), pressure drop oscillation (PDO), and thermal oscillations. These experiments aim to close the gap and contribute to experimental research in the field of water-steam two-phase flow with horizontal test sections exposed to the forced circulation.

1.3 State of the Art

At the beginning of the present century, research rose on this kind of power plants because of the grants that are given by the Global Environment Facility to some developing countries. Many types of researches have been implemented concerning the ISCCs. These researches study the ISCC from different points of view. The historical research and its state of the art are presented in the following subsections categorized by the methodology applied in this thesis. This methodology begins with performing energy and exergy analysis followed by a dynamic process simulation, then the experimental investigation of the two-phase flow dynamic instabilities.

1.3.1 Energy and Exergy Analyses

In the following review, different thermodynamic studies were performed to investigate the thermodynamic performance and the economic feasibility of the ISCC power plants.

B. Kelly et al. [15] demonstrated that the ISCC power plant concept presents an effective path for the continued development of PTC technology regarding the solar thermal-to-electric conversion efficiencies and the solar energy levelized energy cost (LEC). The conceptual plant designs in their work were developed using the GateCycle program. The results showed that the solar thermal-to-electric conversion efficiencies of ISCC will exceed those of a solar-only PTC plant and this technology provides further reductions in the solar energy levelized energy cost (LEC).

J. Dersch et al. [8], in collaboration with the International Energy Agency SolarPACES (Solar Power and Chemical Energy Systems) organization, studied the advantages and disadvantages of ISCC systems compared with solar electric generation systems (SEGS) and conventional CCGT power plants. The study showed the environmental and economic benefits of each ISCC configuration.

J. Rheinlander et al. [16] studied economically and technically ISCCs with PTCs and volumetric air receiver tower for implementation in Egypt. The results showed that the two systems are the same from the economic point of view.

A. M. Patnode [17] developed a comprehensive model of the SEGS VI using TRaNsient SYstem Simulation program (TRNSYS) for the solar part of the system and Engineering Equation Solver (EES) program for the power cycle part. SEGS VI plant's data were used for modeling. This model evaluated the effects of solar field collector degradation, HTF flow rate control strategies and alternative condenser design's performance. The results showed that the gross system efficiency is insensitive to variations in the mass flow rate and solar field outlet temperatures.

Y. Usta [18] created a model in the TRNSYS simulation environment for the solar field and power cycle of a large-scale solar thermal power plant in Turkey. The results showed that the power plant must include significant storage or backup heating. And G.C. Bakos et al. [19] uses TRNSYS software to develop a model simulates the power boosting mode of operation for a 50 MW ISCC power plant with PTC technology.

H. Derbal-Mokrane et al. [20] used TRNSYS simulation program to determine the annual performance of an ISCC in Algeria, under Hassi R'mel area conditions for reference days. A mathematical model of the main basic components in ISCC system was introduced. The results

show that the combined cycle electric power remains constant. The solar electric power of the plant increases until reaches a certain hour through the day and then decreases.

A. Baghernejad et al. [21] demonstrates the application of the exergoeconomic concept to optimize an Integrated Solar Combined Cycle System (ISCCS). The optimization code that developed shows that exergy and thermoeconomic analysis improved significantly for optimum operation.

M.J. Montes et al. [22] compared the annual operation of ISCC system and conventional gas turbine combined cycle (GTCC). The analysis showed that ISCC is more economic.

A. Rovira et al. [7] used exergy analysis to determine the best layout for optimum integration of solar resource with fossil fuel. Different ISCC configurations using PTCs working with HTF or direct steam generation were used. The evaporative direct steam generation configuration was found to have the lowest irreversibility at the HRSG and the highest thermal efficiency in the solar field.

E. Pihl et al. [14] assessed the optimal performance and cost of integrating parabolic troughs with an existing CCGT power plant by developing a thermo-economic optimization model of the ISCC resulting from this integration using the Epsilon Professional 9.0 software. The assessment showed that the equivalent solar levelized electricity cost (LEC) from a retrofitted CCGT is less than the LEC for the conventional CSP system and thermal storage is not economically attractive for the ISCC.

G. Bonforte et al. [23], P. Iora et al. [24], M. Mehrpooya et al. [25], and A. Baghernejad and M. Yaghoubi [26] implemented exergetic analyses of ISCC power plants. G. Bonforte et al. [23] developed an exergo-environmental and exergo-economic model to analyze an ISCC power plant in Southern Poland under the design conditions. The results showed that the CO₂ emissions were reduced by 9%. P. Iora et al. [24] presented a novel allocation method for the electricity produced in an ISCC based on the exergy loss approach by implementing internal exergy balances. They showed that this method is reliable and as good as the conventional Separate Production Reference method. M. Mehrpooya et al. [25] constructed a model using ASPEN HYSYS simulation software and MATLAB code to exergetically analyze an ISCC with a high-temperature energy storage system. It was found that the largest exergy losses were at the solar collector, the energy storage system, and the combustor.

A. Baghernejad and M. Yaghoubi [26] carried out energy and exergy analyses for an ISCC in Yazd, Iran using the design data of the power plant. The results showed that the energy and exergy efficiencies of this power plant are higher than those for a simple CCGT power plant without a solar contribution and those for steam power plants with PTC technology. O. Behar et al. [13] simulated the performance of the first ISCC in Algeria, under Hassi R'mel climate conditions. The results showed that the output power and the thermal efficiency increased in the daytime than at night by 17% and 16.5%, respectively. Where the output power increased from 134 MW to 157 MW and the thermal efficiency was increased from 57.5 to 67%. On the other hand, the steam turbine capacity was increased by 50% at the design point.

S. Wang et al. [27] analyzed the performance variation of the solar field and overall ISCC using advanced exergy analysis methods and hourly analysis within a typical day. The results showed

that increasing the solar energy input to the ISCC system decreases the exergy destruction of the Brayton cycle and increases the exergy destruction of the Rankine cycle.

L. Duan and Z. Wang [28] proposed a novel ISCC system which integrates a gas turbine inlet air cooling system driven by solar energy with the traditional ISCC system, using Aspen Plus and EBSILON softwares to build the models. The results showed that the proposed system has better thermodynamic and economic performance than the traditional ISCC system.

S. Wang and Z. Fu [29] proposed an ISCC coupled with an organic Rankine cycle (ISCC-ORC) using different organic fluids and investigated the thermodynamic and economic performance of it. The performance investigation showed that the proposed ISCC-ORC system improved the performance of the ISCC.

D. Liqiang et al. [30] proposed an ISCC contains a solar energy-driven chiller for cooling the inlet air of the gas turbine's compressor and analyzed its performance. The results show that the proposed system has a higher solar thermal efficiency and a larger annual solar power generation than the traditional ISCC system.

G. Wang et al. [31] conducted an exergetic analysis of the ISCC system for electricity generation and refrigeration using the Ebsilon software with the gray-box model. The analysis found that the ISCC system has overall exergy efficiency of 44.63% and the largest exergy destruction occurred in the combustion chamber followed by the solar direct steam generation system.

From this literature review, one can find several papers regarding the investigation of ISCC power plants applied to different atmospheric conditions. The originality of this work is the parametric study of the energy and exergy analyses regarding an existing ISCC power plant in Egypt, under Kuraymat climate conditions, as a whole and for the main components in the ISCC power plants. This work aims to identify the sites of major exergy destruction, clarify the reasons for exergy destruction in these sites, and attempt to clarify how to decrease the exergy destruction in this type of power plant. Besides this, given the challenges for the electricity market with the continuing expansion of intermittent renewables, in this work, we investigate the operational flexibility of ISCC power plants.

1.3.2 Dynamic Process Simulation

In the literature, the dynamic process simulation of ISCC power plants is less presented than the steady-state process simulation. The dynamic simulation validation is a key aspect to evaluate these ISCC power plants realistically and reliably to make a well-founded decision on their technological feasibility. In particular, a few studies that have addressed the dynamic simulation complemented their models with actual measurement validation.

J. Spelling et al. [32] performed a thermo-economic optimization of a CCGT power plant integrated with a solar tower with a developed dynamic model using the in-house simulation tool SOLARDYN. This dynamic model is used to obtain the minimal initial investment cost as well as the minimal level of electricity cost. They concluded that the ISCC power plants are both economical and thermodynamic promising after they properly designed and they have a competitive level of electricity cost compared with those of other solar thermal power plants.

G. Franchini [33] dynamically simulated a solar Rankine cycle and an ISCC by adopting the TRNSYS types of the solar thermal electric components library. The simulation results revealed

that the ISCC has a higher solar-to-electric efficiency than the solar Rankine cycle and using the solar tower technology assured a higher annual solar-to-electric efficiency, about 21.8%, compared to parabolic trough collectors. The highest solar power production and the highest annual solar-to-electric efficiency of 21.8% were found to be with ISCC coupled with solar tower field, higher conversion efficiency of solar energy introduced into the combined cycle, as compared to SRC, while the solar-to-electric efficiency decreased to be 18% and 13.2% in both cases of ISCC and SRC coupled with PTC respectively.

C. Ponce et al. [34] designed a dynamic simulator for an ISCC power plant using MATLAB Simulink[®], based on a solar power plant simulator and a CCGT power plant simulator developed by E. Camacho et al. [35] and D. Sáez et al. [36], respectively. They combined their dynamic simulator with a supervisory control strategy regulating the steam pressure of the superheater (SH) to account for the fuel savings that could be achieved when integrating solar collectors with a CCGT power plant.

F. Calise et al. [37] developed a dynamic simulation model of an ISCC power plant with thermal storage using TRNSYS and presented a thermo-economic and environmental comparison between an ISCC and a conventional combined cycle based on dynamic simulations. The dynamic model verified that the overall electrical efficiency of the ISCC increases, by about 1%, compared to a conventional combined cycle.

B. El Hefni [38] assessed the benefits of converting an existing CCGT power plant to an ISCC power plant regarding the dynamic behavior of the power plant through creating a dynamic model of an ISCC power plant using Modelica. The model was used to simulate the start-up and shutdown of the solar field and to assess its impact on the dynamic behavior of the ISCC power plant.

K. Rashid et al. [39] evaluated the techno-economic performance and the life cycle of a plant-level hybridization (ISCC power plant), compared with grid-level hybrid units and a natural gas plant, using dynamic models through the System Advisory Model (SAM). The evaluation indicated that hybridization at the plant level has better synergy benefits than hybridization at the grid level. However, the solar efficiency and solar share of the plant-level hybridization are higher than those of the grid-level hybridization.

L. Duan et al. [40] revealed the off-design performance characteristics of ISCC system under different gas turbine off-design operation modes and different environmental conditions. The model results showed that the influence of the ambient temperature on ISCC system is greater than the influence of DNI on ISCC system.

Z. Wang and L. Duan [41] proposed the ISCC system with a changeable integration mode under different DNI conditions. The performance investigation of the ISCC system under this new operation strategy showed that the annual solar to electricity efficiency increases by 1.1% compared with traditional ISCC system and The economic performance analysis showed that the LCOE this proposed ISCC system decreased with 0.01 \$/kW·h compared with the traditional ISCC system.

N. Abdelhafid [42] investigated the dynamic behavior of the ISCC under off-design conditions by developing and validating a dynamic model for the Hassi R'mel ISCC power plant in Algeria using

MATLAB. The simulation results proved that wind speed and direct normal irradiance (DNI) have a significant influence on ISCC performance.

N. Zhang et al. [43] built a dynamic model of the ISCC system using the lumped parameter method and compared the dynamic performance of the ISCC systems with and without a heat storage system under a typical day of operation. The comparison indicated that the ISCC system with thermal storage has better stability than that without thermal storage as a result of reducing the disturbances caused by DNI variations.

Considering the limited existing work, this work contributes to bridge the knowledge gap in the dynamic simulation of ISCC power plants. However, most reviewed studies so far suffer from the fact that the developed dynamic models are not validated using actual measurements. In this study, a sophisticated dynamic process model representing the Kuraymat ISCC power plant in Egypt was developed using APROS software. All processes and automation are modelled according to the specification of the reference plant. Moreover, a detailed dynamic validation of the developed model using actual measurements of different four days from the reference ISCC power plant was implemented. Such a detailed dynamic validation is not available in the literature.

1.3.3 Two-phase Flow Dynamic Instabilities

Mathematical models for describing the phenomena from the literature are summarized and critically reviewed under the boundary conditions of an HRSG, especially also the experimental plant, and the necessary quantities and definitions for describing the two-phase flow are discussed. In the following review, different set-ups were used to investigate the different types of two-phase flow dynamic instabilities. M. Kaichiro et al. [44] studied the relation between burnout and instabilities for water above the critical point. And Q. Wang et al. [45] formulated a correlation for the prediction of limiting heat flux and quality of the DWO type. Some other researchers studied the dynamic instabilities using water as a test fluid in a vertical test tube with natural circulation as an external characteristic. K. C. Jain et al. [46] discussed the effect of system geometry on the behaviour of the DWOs. D. Delmastro and A. Clause [47] studied phase trajectories and chaos analysis. J. M. Kim and S. Y. Lee [48] emphasized the role of the flow restriction between the expansion tank and the experimental loop and studied several instability interacting modes. S. Guanghui et al. [49] derived a criterion and period correlation of DWO. And A. Baars and A. Delgado [50] studied modes of geysering coupled with manometer oscillations and the interaction of the DWO_I and DWO_{III} . These researchers conducted experiments with water in a vertical test tube exposed to the forced circulation.

The horizontally oriented test tube with water as a test fluid is very rare. J. S. Maulbetsch and P. Griffith [51] studied the influence of the compressible volume on the PDO and DWO with water driven by forced circulation in horizontal orientation pipe. And S. Karsli et al. [52] investigated the amplitudes and periods of the DWOs in a horizontal pipe with inserts.

The following researchers conducted experiments with horizontally oriented test tubes but they used a refrigerant as a test fluid. H. Yüncü [53] developed a model based on the homogeneous flow assumption to predict stability boundaries of the boiling two-phase flow system for the PDO and DWO and compared its results with his experimental results. Ö. Çomaklı et al. [54] investigated the pipe length effect on the dynamic instabilities besides defining the boundaries for the appearance of PDO, DWO and thermal oscillations. S. Karsli et al. [52] investigated the effect of

internal surface modification on the boundaries for the appearance and the characteristics of the PDO, DWO and thermal oscillations. S. Kakaç and L. Cao [55] analysed the PDO and thermal oscillations with upstream compressible volume in both, vertical and horizontal test tubes numerically with the Drift-Flux model and verified the results by his experimental findings. N. Liang et al. [56] investigated the two types of instabilities, static and dynamic, in a refrigeration system. C. A. Dorao [57] studied the period of DWOs in a uniformly heated horizontal test tube experimentally. M. Sørnum and C. A. Dorao [58] studied the effect of the DWO on the boiling heat transfer coefficient. L. Zhang et al. [59] investigated the relationship between changing the heat flux and inlet subcooling degree on the features of DWO and PDO. I. W. Park et al. [60] studied the interaction between PDOs and superimposed DWOs. L. Zhang et al. [61] analyzed the effect of the heat load distribution and the wall thermal capacity on the stability of the flow boiling. Finally, I. W. Park et al. [62] observed the influence of the existence of a compressible volume in the system on the amplitude of the superimposed DWO.

The knowledge extension of the occurrence of two-phase flow instability phenomena in power plants through experimental investigation is needed. As shown in the literature, there are only a few experimental studies regarding the instabilities analyses for vertical HRSG. Furthermore, it can be seen that little research in the field of two-phase flows deals with demineralized water as a test fluid. Previous experimental studies in this research area mainly used refrigerants such as Freon-11, because of their low boiling point. In contrast, in this study, a downscaled test rig for two phase instabilities starting from a vertical HRSG is operated with the demineralized water as a test fluid to avoid potential side effects due to different fluid properties. Another point by which the used test rig differs from previous ones is the variability in parameters concerning startup processes, the orientation of the evaporator pipe and the multiplicity of operating options.

In this thesis, experimental results for the main three types of the two-phase flow dynamic instabilities (density wave oscillations, pressure drop oscillations and thermal oscillations) were provided and discussed after investigating the internal characteristic curve for the evaporator tube of the two-phase flow test rig.

1.4 Outline of the Thesis

The outlines of this research work at-a-glance:

Chapter 1 “Introduction” contains the background and motivation for investigating the performance of integrated solar combined cycle (ISCC) power plants. Furthermore, the objectives of the study and the methodology applied are explained. This is followed by an overview of historical research and its state of the art, categorized by the methodology applied in this thesis. Then, the outlines of the thesis and the author’s publications in international peer-reviewed journals and conferences are presented.

Chapter 2 “Energy and Exergy Analyses of ISCC” discusses the principle of the energy and exergy analysis, followed by a detailed description of the ISCC power plant under investigation. In addition, the method and equations used to calculate the energy and exergy parameters are presented. Then, the influence of ambient temperature and solar heat input on system performance

was discussed, followed by the assessment of the sources of exergy destruction in the solar field and combustion chamber.

Chapter 3 “Dynamic Process Simulation of ISCC” begins with a background for mathematical modelling especially the dynamic process simulation. Then, a sophisticated dynamic process model representing the Kuraymat ISCC power plant in Egypt was developed using APROS software. The study includes measurement validation to analyze the influence of modelling assumptions on simulation results.

Chapter 4 “Experimental Investigation of Dynamic Instabilities in HRSG” presents briefly the fundamentals of the two-phase flow and explains the mechanisms of three main types of the two-phase flow dynamic instabilities in water tube boiling in detail using simple models. Also, the design of the test rig using similarity-based scaling criteria and the flexibility of the two-phase test rig are mentioned. Then, it provides experimental results for the Two-phase Flow Dynamic Instabilities in Tube-Boiling System.

Chapter 5 “Conclusion and Outlook” conclusions and recommendations resulting from this thesis are summarized in this chapter and an outlook for future research was mentioned.

1.5 Publications

1.5.1 Publications in International Peer-reviewed Journals:

- **A. Temraz**, A. Rashad, A. Elweteedy, F. Alobaid, and B. Epple, “*Energy and Exergy Analyses of an Existing Solar-Assisted Combined Cycle Power Plant*,” *Appl. Sci.*, vol. 10, no. 14, p. 4980, Jul. **2020**, doi: 10.3390/app10144980.
- **A. Temraz**, F. Alobaid, T. Lanz, A. Elweteedy and B. Epple, “*Operational Flexibility of Two-Phase Flow Test Rig for Investigating the Dynamic Instabilities in Tube Boiling Systems*,” *Front. Energy Res.* 8:517740, Sep. **2020**. doi: 10.3389/fenrg.2020.517740.
- **A. Temraz**, F. Alobaid, J. Link, A. Elweteedy and B. Epple, “*Development and Validation of a Dynamic Simulation Model for an Integrated Solar Combined Cycle Power Plant*,” *Energies*, 14(11):3304, Jun. **2021**. <https://doi.org/10.3390/en14113304>.
- A. Rashad, A. Elweteedy, **A. Temraz**, and A. Gomaa, “*Investigating an Integrated Solar Combined Cycle Power Plant*,” *Glob. J. Eng. Sci. - GJES*, vol. 7, no. 1, pp. 1–14, **2021**, doi: 10.33552/GJES.2021.07.000652.

1.5.2 Manuscripts for Publication in International Peer-reviewed Journals:

- **A. Temraz**, F. Alobaid, T. Lanz and B. Epple, “*Experimental Investigation of Two-phase flow Dynamic Instabilities in Subcooled Flow Boiling of Water in Horizontal Macro-channel System*,” Under review.

1.5.3 Publications in Peer-reviewed Conference Proceedings:

- **A. Temraz**, A. Rashad, A. Alweteedy, and K. Elshazly, “*Seasonal Performance Evaluation of ISCCS Solar Field in Kureimat, Egypt*,” in 6th Annual International Conference on Sustainable Energy and Environmental Sciences (SEES 2017), Mar. 2017, no. March, pp. 91–98, doi: 10.5176/2251-189X_SEES17.38.

-
- **A. Temraz**, A. Rashad, A. Elweteedy, and K. Elshazly, “*Thermal Analysis of the ISCC Power Plant in Kuraymat, Egypt*,” in 18th International Conference on Applied Mechanics and Mechanical Engineering (AMME 18)., 2018, pp. 3–5, doi: 10.21608/AMME.2018.34995.

Chapter 2: Energy and Exergy Analyses of ISCC

In this chapter, energy and exergy analysis was performed for the Kuraymat ISCC power plant. The chapter begins with an introduction to energy and exergy analysis, followed by a detailed description of the ISCC power plant under investigation. Then, the method and equations used to calculate the energy and exergy parameters are presented. Finally, the influence of ambient temperature and solar heat input on system performance was discussed, followed by the assessment of the sources of exergy destruction in the solar field and combustion chamber.

2.1 Introduction

The conventional energy analysis based on the first law analysis gives the quantitative not the qualitative assessment of the various losses occurring in the components of such solar thermal system. Therefore the exergy analysis based on the second law analysis should be used to get a complete assessment of the various losses qualitatively as well as quantitatively. So, the exergy analysis complements the energy analysis not to replace. Exergy analysis indicates the location of the wasted exergy, in addition, to quantify the collection and useful consumption of exergy, which leads the way to improve the system.

Energy and exergy analysis of the ISCC power plant is carried out to determine the plant performance and pinpoint sites of primary exergy destruction. Exergy-based performance analysis overcomes the limit of studying the system based on the first law of thermodynamics. It assesses the magnitude and percentage of exergy destruction in each part of the system.

In the literature, one can find several papers regarding the investigation of ISCC power plants applied to different atmospheric conditions. In this work, a parametric study for the energy and exergy analyses of the Kuraymat ISCC power plant in Egypt as a whole and the main components in the ISCC power plants were performed. The overall thermal efficiency and the exergetic efficiency of each component in the power plant were calculated for different solar field capacities. Owing to the results, an investigation of the sources of the exergy destruction in the solar field was conducted. The suggested recommendations and the proposed model offer the possibility of further simulation studies and prospective works. Hence, the strategy of model build-up can be transferred to other applications by the same procedure. To give the challenges for the electricity market as intermittent renewables continue to expand, the operational flexibility of ISCC power plants was investigated.

2.2 Plant Description

The entity of Egypt in the Sun Belt countries provides it with a very high annual DNI ranging from 1970 to 3200 kWh/m² per year from North to South with lengthy daily sunshine periods of about 9 to 11 hrs. and few cloudy days over the year make it a more attractive country for CSP technology [63]. The global environment facility (GEF) supported studying An (ISCCS) technically and economically for implementation in Egypt [16]. The plant is located in Kuraymat at a northern latitude of 29°16' and eastern longitude of 31°15', about 87 km South of Cairo, Egypt. The Kuraymat site was chosen from four suggested sites (Kuraymat, Sinai Peninsula, West Desert

and Red Sea Coast) after studying it by the New & Renewable Energy Authority (NREA) due to the least additional infrastructure. The site was selected to comprise an unoccupied flat desert area, high DNI which reaches 2400 kWh/m^2 per year, vicinity to water sources, and vicinity to the extended natural gas pipelines. The construction of the ISCC Kuraymat power plant was begun in January 2008 and start commercial operation as a whole in June 2011 [10], [64]. The plant is owned by the NREA in the ministry of electricity and energy of Egypt. The Global Environmental Facility (GEF), accessed through the World bank, has contributed a grant of USD 49.8 Million towards the incremental cost of solar electricity generation [9]. The objective of the project was to increase the share of solar-based electricity in the Egyptian energy generation mix. The global development objective of the project was to reduce greenhouse gas emissions from anthropogenic sources by increasing the market share of low greenhouse gas-emitting technologies.

The ISCC power plant in Kuraymat of approximately 135 MW total power capacity consists mainly of two parts, the solar field and the combined cycle. It comprises a combined cycle with a power of 115 MW and a solar field with an electrical output of 20 MW [65]. The combined cycle includes a gas turbine (GT) with an electrical power output of 70 MW and a steam turbine (ST) with an electrical output of 65 MW [66], [67]. The combined cycle is coupled with a parabolic trough collector solar field, as shown in **Figure 2.1**. The solar field includes 160 parabolic trough collectors, that uses the heat from the sun to warm up a heat transfer fluid (HTF) used to generate high-pressure (HP) steam in HTF heat exchangers (solar field heat exchangers).

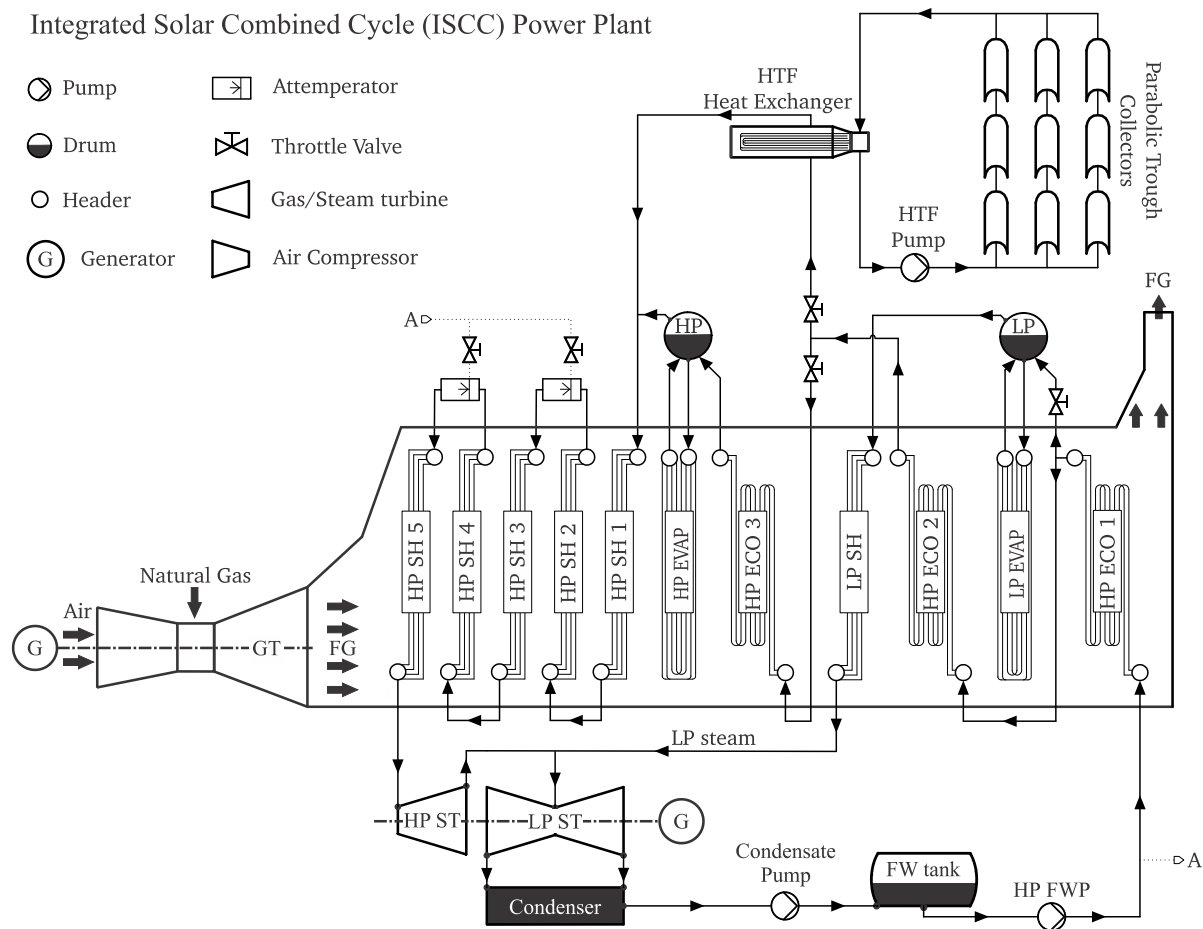


Figure 2.1 Schematic diagram of the Kuraymat ISCC power plant

During the day, a part of the feedwater (FW) extracted from the heat recovery steam generator (HRSG) and pass through the HTF heat exchangers, then this FW leaves the HTF heat exchangers as steam and is fed back to the HRSG, where it is superheated. The integration of a combined cycle with the solar field ensures the delivery of the required electricity contribution to the grid regardless of solar radiation conditions.

In the combined cycle, the HRSG is located behind a GT, using the heat of the exhaust gasses from the GT to produce steam, which drives the ST and the generator (G). The objective of the HRSG is to use the hot exhaust gasses from the GT to heat water and convert it into pressurized superheated steam. The pressurized superheated steam expands in the ST, which drives a generator to produce electrical power. At the rated output operating point, the GT supplies approx. 206 kg/s flue gases (FG) at a temperature of approx. 630 °C to the HRSG. The FG leave the HRSG system with a temperature of approx. 100 °C [68]. The enthalpy difference is transferred to the water-steam circuit to generate pressurized superheated steam.

The reference plant has two operating modes, day mode, and night mode. During night mode the solar field is shut down and the HRSG and the ST are operating at lower output mode. During day mode the solar field is in operation and the generated steam is fed to the HRSG then to the ST, which operates at a higher output mode. The load of the GT is approximately constant and independent of the operating mode (day / night mode).

2.2.1 Solar Field

The solar field comprises parallel rows of solar collector arrays and typical glass mirrors of 61 MW installed thermal capacity and two solar heat exchangers each with a heat transfer capacity of 50MJ/s. It comprises 40 loops, each loop having four parabolic trough collectors (type Skal-ET 150 designed by TSK Flagsol Engineering GmbH), as indicated in **Table 2.1**, and each collector has an aperture area of 817.15 m².

Table 2.1 The solar field design parameters [25], [26], [64]

Solar field operation parameter	Unit	Value
Total aperture area of the solar field	m ²	130,800
Number of collectors per loop	N ^o	4
Number of loops	N ^o	40
Design DNI	W/m ²	700
Maximum solar heat input	MW	61
Output temperature of the HTF	°C	393
Input temperature of the HTF	°C	293

The solar heat transfer from the solar field collectors (PTCs) to the steam cycle uses a heat transfer fluid (HTF) system. The HTF is Therminol VP-1 from Solutia (ultra-high-temperature, liquid / vapor phase fluid) and operates between 12 °C and 400 °C (54–750 °F) [69], [70]. The

HTF system is designed for an HTF mass flow rate of 250 kg/s at full load (61 MW of solar field thermal power output). Hot HTF returning from the solar field at 393 °C is pumped through the solar heat exchanger. The HTF leaves the solar heat exchanger at 293 °C and is pumped back into the solar field. The solar field supplies thermal energy to the solar heat exchanger train to produce steam, which supplements the turbine steam from the HRSG to increase the output of the steam turbine. The solar field tracks the sun on a single axis, absorbing direct normal radiation.

2.2.1.1 Solar Collector

The installation of the parabolic trough collector design is based on the SKAL-ET 150. This collector is designed to be gathered from pre-fabricated low-cost steel structure that can be manufactured locally all over the world. The PTC consists of reflectors and receiver (Heat Collection Element “HCE”). **Figure 2.2** shows the main components of the SKAL-ET collector. The reflectors are created by bending a sheet of reflective material (silver edlow-iron float glass) into a parabolic shape. The receiver is a black treated metal tube, the absorber tube, in the focal point of the reflector. The solar mirrors for the ISCC Kuraymat are FLABEG in 4 millimeters and 5 millimeters thickness. The absorber tube (HCE) is surrounded by a glass cover and the space between the pipe and the glass cover is evacuated to reduce heat losses by conduction to the surroundings. The glass tube is created from special materials and mostly coated with anti-reflective films to improve solar transmittance and reduce solar reflectivity. The glass tube vacuum stability depends on the mechanical strength and temperature resistance of the glass-to-metal seal due to the combination of materials with matching coefficients of thermal expansion. The glass-to-metal seal of the receiver must handle intense temperature changes and ensures vacuum durability. The concentration ratios (ratio of solar flux on the receiver to that on the mirrors) of the Parabolic troughs that can be achieved is between 10 and 100 [71]. The collectors are arranged along a north-south axis and can rotate from east to west over each day. The main specifications of the Kuraymat collectors are illustrated in **Table 2.2**.

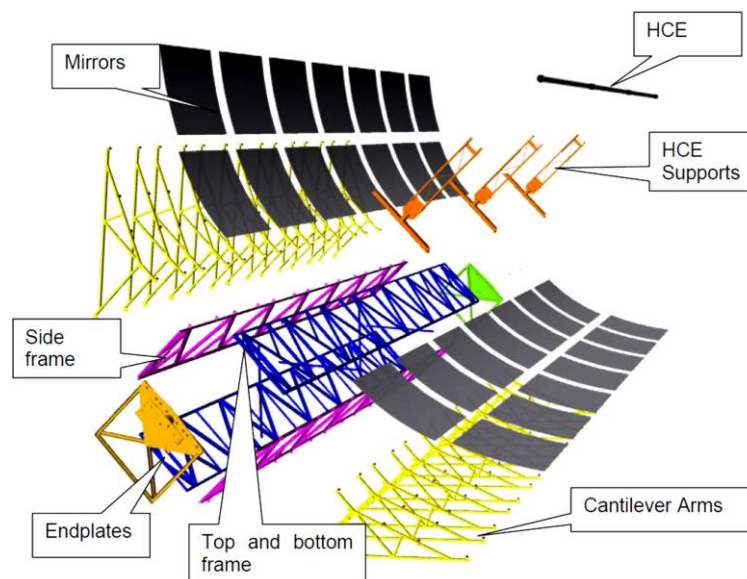


Figure 2.2 Main components of the SKAL-ET collector [71]

The solar collectors follow the sun during the daytime and can track the sun during periods of intermittent cloud cover since a tracking mechanism is used. The tracking system used in the Kuraymat plant for the parabolic trough concentrator is based on “virtual” tracking. In which, a

mathematical algorithm calculates the sun position replaced a conventional sun-tracking unit with sensors that detect the position of the sun [72].

The solar field consists of 40 loops. Four collector assemblies of type SKAL-ET 150 are contained per loop. The collector assembly comprises 12 solar collector elements (SCE).

Table 2.2 The main specifications of the one-axis parabolic trough collectors in Kuraymat ISCC power plant

Parameter	Unit	Value
SCA manufacturer (Model)	-	Flagsol (SKAL-ET 150)
Mirror manufacturer (Model)	-	Flabeg (RP3)
Mirror type	-	Silver edlow- iron float glass
HCE manufacturer (Model)	-	Schott (PTR 70)
Drive	-	Hydraulic
Aperture width	m	5.73
Focal length	m	1.71
Length per element	m	12
Length per collector	m	142.80
Mirror aperture area	m ²	817.15
Receiver diameter	m	0.07
Geometric concentration	-	82:1
Peak optical efficiency	%	80

2.2.1.2 HTF System

The solar heat transfer from the solar field collectors (PTCs) to the steam cycle is done by the HTF system. The HTF system includes the main HTF pumps, the HTF conditioning system, the piping connecting the solar field and the solar heat exchangers. The HTF conditioning system is used to eliminate high and low boiling compounds which are formed by degradation of the fluid.

The reflector mirrors focus the incident direct normal solar radiation into the absorber. The HTF is circulated through the absorber tube to acquire the solar heat. The HTF can be heated to temperatures of up to 400 °C [70]. The main specifications of the HTF are included in **Table 2.3**.

The HTF system is designed for an HTF mass flow rate of 250 kg/s (100%) of Solutia's Therminol VP1 at 100% load (61 MJ/s of solar field thermal power output). The mass flow rate of the HTF varies between 30 and 100% or higher due to the different solar irradiation. As a function of the mass flow rate, the pressure drop in the HTF cycle varies in a wide range between 1 bar and 15 bar [73]. The properties of Therminol VP1 can be calculated using the equations provided by the producing company [74].

The specific heat capacity (C_p) in [kJ/kg·K] is given by:

$$C_p = 0.002414 * T[^\circ\text{C}] + 5.9591 * 10^{-6} * T^2[^\circ\text{C}] - 2.9879 * 10^{-8} * T^3[^\circ\text{C}] + 4.4172 * 10^{-11} * T^4[^\circ\text{C}] + 1.498 \quad (2.1)$$

The specific enthalpy (h) in [kJ/kg] is given by:

$$h = 1.51129 * T[^\circ\text{C}] + 1.2941 * 10^{-3} * T^2[^\circ\text{C}] + 1.23697 * 10^{-7} * T^3[^\circ\text{C}] - 18.72677 \quad (2.2)$$

The HTF normal operating temperatures are 293 °C at the inlet of the solar field and 393 °C at the outlet which are usually reached within 20 to 60 minutes after starting the solar energy accumulation. Duration mainly depends on the actual solar irradiation and the initial HTF cycle temperatures.

Table 2.3 Therminol VP-1 main specifications [74]

Property	Value
Liquid phase heat transfer	12 to 260 °C (Liquid) 260 to 400 °C (Vapour / liquid)
Appearance	Clear, water-white liquid
Composition	73.5% diphenyl oxide, 26.5% biphenyl
Flashpoint, (ASTM D-92)	124 °C
Fire point, (ASTM D-92)	127 °C
Auto-ignition temperature (ASTM E659)	621 °C
Viscosity, mm ² /s (cSt)	3.70 @ 25 °C
	0.59 @ 150 °C
	0.29 @ 250 °C
	0.15 @ 400 °C
Crystallizing point	12 °C
Heat of vaporization	205 kJ/kg @ 400 °C
Density, kg/m ³	1,060 @ 25 °C
	957.0 @ 150 °C
	867.0 @ 250 °C
	694.0 @ 400 °C
Heat capacity, kJ/kg·K	1.56 @ 25 °C
	1.91 @ 150 °C
	2.18 @ 250 °C
	2.63 @ 400 °C
Thermal conductivity, W/m·K	0.136 @ 25 °C
	0.121 @ 150 °C
	0.106 @ 250 °C
	0.076 @ 400 °C

The HTF mass flow rate control system is implemented to optimize the outlet temperature of each solar field loop. Theoretically, the HTF outlet temperatures for all the single loop are the same [73].

Since the HTF solidifies at 12.3 °C, a freeze protection system is installed. This freeze protection is needed when the solar field is not operated for several days. At normal operation, no need for freeze protection, the thermal inertia of the HTF content itself is sufficient to prevent freezing during the night hours.

2.2.1.3 HTF Heat Exchangers

The HTF heat exchangers produce steam using the heat collected by the solar field. They are designed to receive energy from the solar field using the HTF and to convert it into a high pressure/high-temperature steam. The heat exchanger system comprises two trains - operating in parallel mode - each consisting of one economizer and one evaporator, both being a tube-and-shell design. The normal operating temperature of the HTF is 393 °C (hot) at the inlet of the evaporator and 293 °C (cold) at the outlet of the economizer. Enthalpy obtained with the HTF from the solar field is used for steam generation. Both heat exchangers combined have a total thermal capacity of 100 MW. The solar heat exchanger unit generates a slightly superheated Steam of approximately 90 bar, depending on solar heat gain, which is mixed with saturated steam from the high-pressure steam drum.

2.2.2 Combined Cycle

The combined cycle comprises one gas turbine, one heat recovery steam generator (HRSG), and one steam turbine. The gas turbine is MS6001FA heavy-duty with a generator of a rated electric power output of 70 MW at 20 °C ambient dry bulb temperature. It uses advanced aircraft engine technology in its design with a rating based on a firing temperature class of 2350 °F / 1288 °C [75]. The HRSG receives about 206 kg/s flue gas at about 600 °C from the gas turbine at full load operation. The flue gas leaves the HRSG at about 100 °C. The steam turbine has a high-pressure section that receives steam from the high-pressure superheaters and a low-pressure section that receives steam from the low-pressure superheater and the high-pressure turbine section. The steam turbine generator output is about 65 MW under the conditions of full load operation with a natural gas mass flow rate of about 4.7 kg/s and solar heat input of 50 MW and 20 °C ambient dry bulb temperature.

Exhaust steam from the low-pressure section of the steam turbine is condensed by a condenser of horizontal shell and tube type. The condenser cooling water temperature rise is 6 °C which is cooled by five cellular type evaporative coolers [65]. About 300 m³/h of raw water is pumped to the plant from an intake station at the Nile, and treated by clarification, filtration and ion exchange. The cooling towers are used clarified water in closed-cycle cooling water make-up. The plant includes a water treatment unit that treats blow down before discharge to the Nile.

2.2.2.1 Heat Recovery Steam Generator

The HRSG of the ISCC power plant in Kuraymat comprises three high-pressure economizers (HP ECO), a high-pressure evaporator (HP EVAP), a high-pressure steam drum (HP drum at a pressure of about 80 bar), and five high-pressure superheaters (HP SH) for a feed of

the high-pressure section of the steam turbine, as shown in **Figure 2.3**. Besides this, it includes a low-pressure evaporator (LP EVAP), low-pressure steam drum (LP Drum at a pressure about 11 bar), and low-pressure superheater (LP SH) for a feed of the steam turbine low-pressure section. The solar-generated steam is injected into the high-pressure drum.

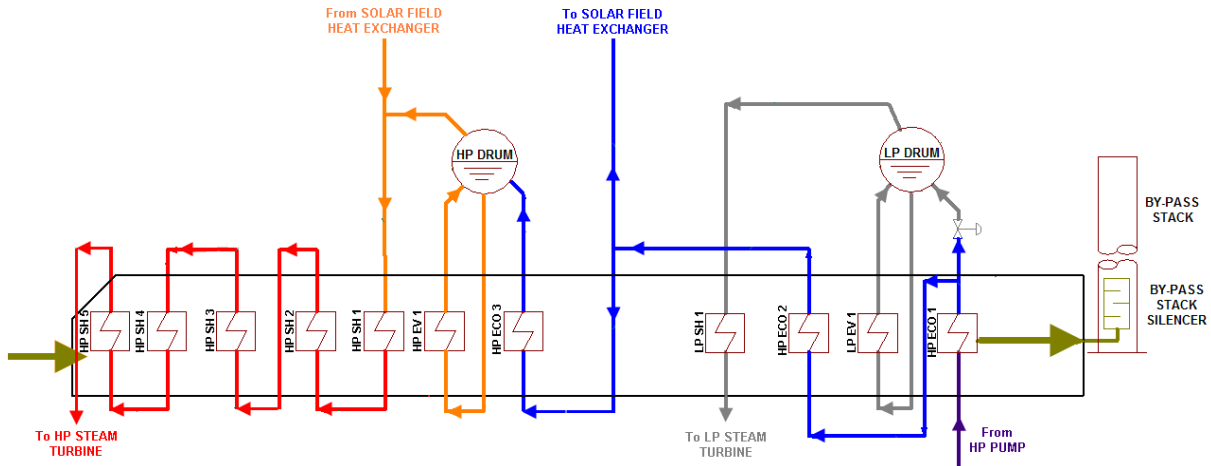


Figure 2.3 Layout of the HRSG of Kuraymat ISCC power plant

HRSG uses the exhaust gases from the gas turbine to produce superheated steam for the steam turbine without any supplementary firing. At rated conditions of the gas turbine full load operation, the HRSG receives about 206 kg/s flue gas from the gas turbine at temperatures of about 600 °C. The flue gas leaves the HRSG at about 100 °C to the stack.

The HRSG of the ISCC power plant in Kuraymat comprises three high-pressure economizers (HP ECO), a high-pressure evaporator (HP EVAP), a high-pressure steam drum of the pressure of about 80 bar, and five high-pressure superheaters (HP SH) for a feed of the high-pressure section of the steam turbine, as shown in **Figure 2.3**. Besides this, it includes a low-pressure evaporator (LP EVAP), low-pressure steam drum of pressure about 11 bar, and a low-pressure superheater (LP SH) for a feed of the steam turbine low-pressure section. The solar-generated steam is injected into the high-pressure steam drum. The solar-generated steam is injected into the high-pressure steam drum.

2.3 Thermodynamic Analysis

The ISCC was evaluated assuming steady-state operation, with no accounting for thermal capacitance. This assumption works fairly well through the majority of the operating day but creates some problems in the morning when the solar field is warming up. The energy and exergy calculations are performed concerning the state points shown in **Figure 2.4**.

A mathematical model was developed to predict the solar field thermal power output and investigate the performance of the solar field. Then, an energy and exergy analysis as well as parametric study for the ISCC power plant were performed to identify the causes and locations of the thermodynamic imperfection. Exergy destruction throughout the plant is determined and illustrated using an exergy flow diagram. Exergetic efficiencies of the main plant components are determined to evaluate their individual performances.

2.3.1 Energy Balance

The net rate of heat input to the ISCC ($\dot{Q}_{ISCC,in}$) is given by:

$$\dot{Q}_{ISCC,in} = \dot{Q}_{fuel} + \dot{Q}_{SF}, \quad (2.3)$$

where \dot{Q}_{fuel} is the rate of heat addition to the ISCC from the fuel combustion and \dot{Q}_{inc} is the absorbed incident solar radiation. The heat from the fuel combustion (\dot{Q}_{fuel}) as a function of the fuel flow rate (\dot{m}_{fuel}) and the fuel heating value (H_v) is given by:

$$\dot{Q}_{fuel} = \dot{m}_{fuel} * H_v. \quad (2.4)$$

The electric power output of the ISCC ($\dot{W}_{elec,ISCC}$) is equal to the sum of the electric power outputs of the gas turbine ($\dot{W}_{elec,GT}$) and the steam turbine ($\dot{W}_{elec,ST}$) as follows:

$$\dot{W}_{elec,ISCC} = \dot{W}_{elec,GT} + \dot{W}_{elec,ST}. \quad (2.5)$$

As a result, the overall first law efficiency of the ISCC power plant is:

$$\eta_{I,cycle} = \frac{\dot{W}_{elec,ISCC}}{\dot{Q}_{ISCC,in}} \quad (2.6)$$

2.3.1.1 Absorbed Incident Solar Radiation

and the heat from the absorbed incident solar radiation (\dot{Q}_{abs}) as a function of the direct normal insolation (DNI), incidence angle (θ), incidence angle modifier (IAM), solar collectors' aperture area ($A_{mirrors}$), the row shadow factor ($Rowshadow$), the end loss coefficient ($Endloss$), the field efficiency (η_{field}), the heat collection element efficiency (η_{HCE}), and the solar field availability ($SfAvail$) is given by [17]:

$$\dot{Q}_{abs} = DNI * \cos\theta * IAM * A_{mirrors} * RowShadow * EndLoss * \eta_{field} * \eta_{HCE} * SfAvail, \quad (2.7)$$

Here, the solar collectors' aperture area ($A_{mirrors}$) is calculated from the number of solar field collectors ($N_{collectors}$) and the width ($W_{collector}$) and length ($L_{collector}$) of the collectors as follows:

$$A_{mirrors} = N_{collectors} * W_{collector} * L_{collector}. \quad (2.8)$$

and, the incidence angle modifier (IAM) is the correlation of the losses from the collectors due to additional reflection and absorption by the glass envelope, and it can be calculated as follows [17]:

$$IAM = 1 + \frac{0.000884 * \theta}{\cos\theta} - \frac{0.00005369 * \theta^2}{\cos\theta}, \quad (2.9)$$

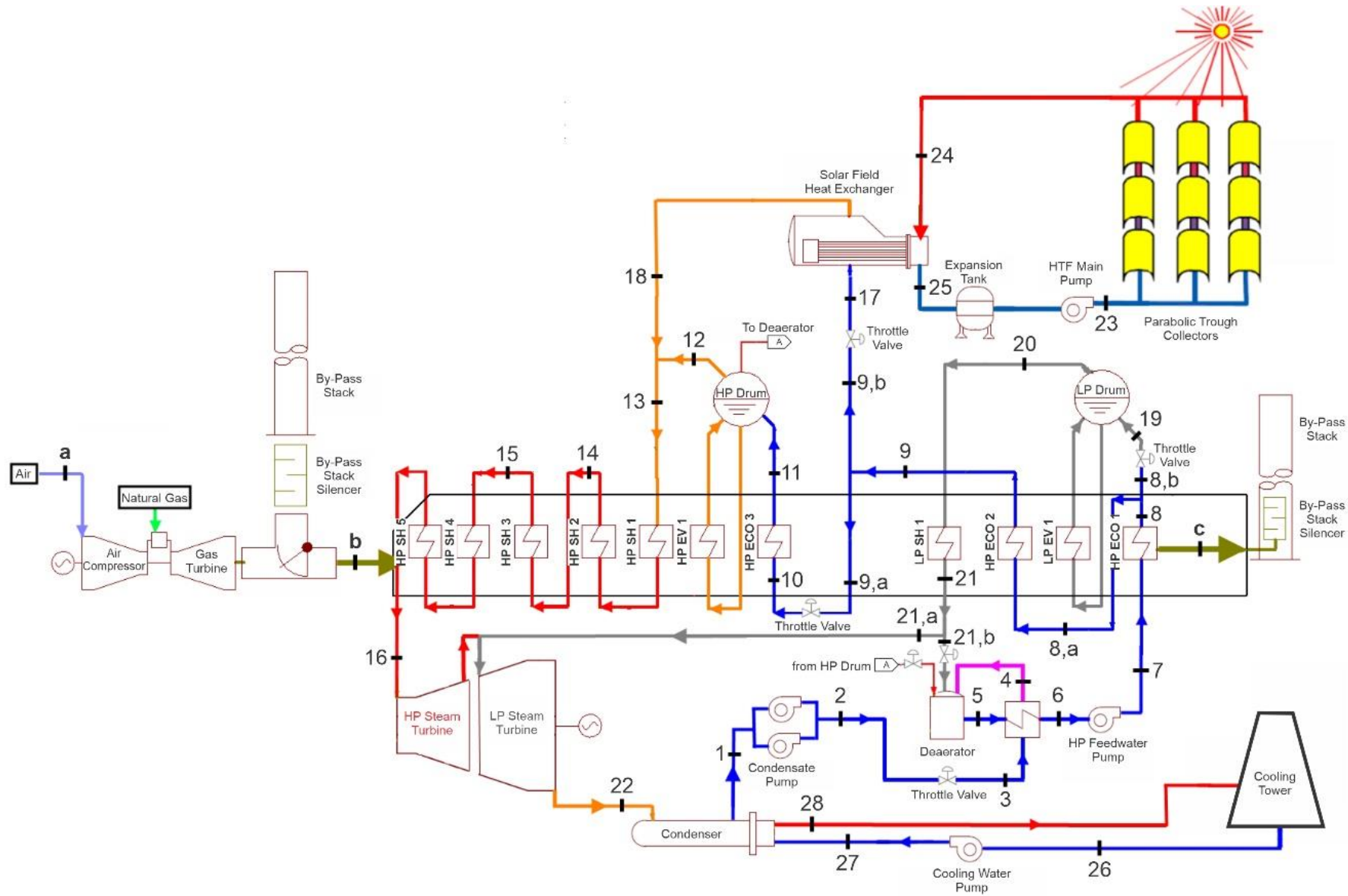


Figure 2.4 A flow diagram of the Kuraymat ISCC power plant with state points illustration

The incidence angle for a plane rotated about a horizontal north-south axis with continuous east-west tracking to minimize the angle of incidence is given by [76]:

$$\cos \theta = \sqrt{\cos^2 \theta_z + \cos^2 \delta \cos^2 \omega}, \quad (2.10)$$

where, θ_z = the zenith angle [degree].

δ = the declination angle [degree].

ω = the hour angle [degree].

The shading of parallel rows during sunrise and sunset periods occurs due to the positioning and geometry of the collector troughs and it causes additional losses as shown in **Figure 2.5**.

These shading losses are represented by the row shadow factor. This factor is the ratio of the effective mirror width to the Collector width. This ratio can be derived from the length of spacing between troughs ($L_{spacing}$), the solar zenith angle (θ_z) and the incidence angle (θ) [77]:

$$RowShadow = \frac{L_{spacing}}{W_{collector}} * \frac{\cos \theta_z}{\cos \theta} \quad (2.11)$$



Figure 2.5 The row shading that occurs during tracking of solar collectors from early to mid-morning [77]

End loss occurs for a non-zero incidence angle. At the ends of the HCEs, a small length of the absorber tube is not illuminated by solar radiation reflected from the mirrors as shown in **Figure 2.6**. As a function of the focal length of the collector, the incident angle and the length of the collector the end losses are:

$$EndLoss = 1 - \frac{f * \tan \theta}{L_{SCA}}, \quad (2.12)$$

f = focal length of the PTC collector [m].

L_{SCA} = length of a single SCA (12 solar collector elements) [m].

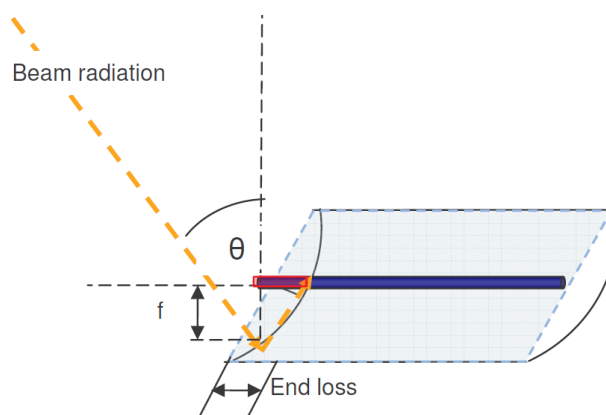


Figure 2.6 HCE end loss [17]

The solar radiation losses are due to the imprecisions of the solar collector trough mirrors, glass envelope, and receiver tube materials which may cause insolation to be absorbed or scattered by dirt on the mirrors, or tracking error. The final solar radiation absorption is affected by the absorptivity of the receiver tube selective coating, the transmissivity of the glass envelope, and other surface properties.

The field efficiency (η_{field}) that represents the correction parameters for the collector assembly and mirrors and the effect of the surface, is given by [17]:

$$\eta_{\text{field}} = \text{TrkTwstErr} * \text{GeoAcc} * \text{MirRef} * \text{MirCln}. \quad (2.13)$$

The HCE efficiency (η_{HCE}) that represents the effect of surface and correction parameters for the heat collection element is given by [17]:

$$\eta_{\text{HCE}} = \text{HCEdust} * \text{BelShad} * \text{EnvTrans} * \text{HCEabs} * \text{HCEmisc}, \quad (2.14)$$

Table 2.4 Typical optical parameters and correction values for the solar field [78]

Name	Value	Name	Value
TrkTwstErr	0.99	BelShad	0.97
GeoAcc	0.98	EnvTrans	0.96
MirRef	0.93	HCEabs	0.95
MirCln	0.95	HCEmisc	0.96
HCEdust	0.98		

TrkTwstErr = the twisting and tracking error associated with collector type [-].

GeoAcc = the geometric accuracy of the collector mirrors [-].

MirRef = the mirror reflectivity [-].

MirCln = the mirror cleanliness [-].

HCEdust = the losses due to shading of HCE by dust on the envelope [-].

BelShad = the losses from shading of ends of HCEs due to bellows [-].

EnvTrans = the transmissivity of the glass envelope [-].

HCEabs = the absorptivity of the HCE selective coating [-].

HCEmisc = the miscellaneous factor to adjust for other HCE losses [-].

2.3.1.2 Receiver Heat Loss

The heat losses from the receiver tube to the surrounding, from the receiver tube to the glass envelope and from the glass envelope to the ambient air, in $[\text{W}/\text{m}^2]$ are driven by temperature difference between the bulk temperature of the fluid and the temperature of the surrounding ambient air.

The effect of wind speed on heat loss is negligible except in the case of a missing glass envelope. While heat transfer fluid flow rate and ambient air temperature influence heat loss from the collector, the effects of these variables are small in comparison to the effect of bulk fluid

temperature and DNI [17]. Thus, the receiver heat loss is modeled as a function of bulk fluid temperature and DNI. It is driven by the temperature difference between the inlet and outlet temperature of the HTF as follows [78]:

$$H_{\text{loss}} = \frac{a_0(T_{\text{out}} - T_{\text{in}}) + \left(\frac{a_1}{2}\right)(T_{\text{out}}^2 - T_{\text{in}}^2) + \left(\frac{a_2}{3}\right)(T_{\text{out}}^3 - T_{\text{in}}^3) + \left(\frac{a_3}{4}\right)(T_{\text{out}}^4 - T_{\text{in}}^4)}{T_{\text{out}} - T_{\text{in}}} + \frac{DNI[b_0(T_{\text{out}} - T_{\text{in}}) + \left(\frac{b_1}{3}\right)(T_{\text{out}}^3 - T_{\text{in}}^3)]}{T_{\text{out}} - T_{\text{in}}}, \quad (2.15)$$

$$\text{RecHL} = \frac{H_{\text{loss}}}{W}, \quad (2.16)$$

where,

H_{loss} = heat loss from the outermost surface of the receiver, per unit length [W/m].

T_{out} = the HTF temperature at the solar field outlet [°C].

T_{in} = the HTF temperature at the solar field inlet [°C].

RecHL = heat loss from the outermost surface of the receiver per unit area [W/m²].

a, b = Coefficients for vacuum annulus receiver [78].

Coefficients for **Eqn. 2.13**, along with their standard deviations, are shown for the vacuum annulus in **Table 2.5** and root mean square (RMS) deviation for the curve fit is equal ± 2.4 W/m.

Table 2.5 Coefficients for receiver heat loss with vacuum annulus

Parameter	Value	Standard deviation
a_0	-9.4630	8.463850E-01
a_1	3.029616E-01	1.454877E-02
a_2	-1.386833E-03	7.305717E-05
a_3	6.929243E-06	1.070953E-07
b_0	7.649610E-02	5.293835E-04
b_1	1.128818E-07	6.394787E-09

2.3.1.3 Solar Field Piping Heat Losses

The heat losses from the piping leading to and from the loops in the solar field in [W/m²] are estimated by the following empirical equation [17]:

$$\text{SfPipeHL} = (0.01693 * \Delta T - 0.0001683 * \Delta T^2 + 6.78E^{-7} * \Delta T^3), \quad (2.17)$$

$$\Delta T = T_{\text{av}} - T_{\text{amb}}, \quad (2.18)$$

$$T_{av} = \frac{T_{in} - T_{out}}{2}, \quad (2.19)$$

where,

T_{amb} = the ambient temperature [°C].

2.3.1.4 Solar Heat Input

The net energy gained by the HTF over the solar field, per unit aperture area [W/m²]:

$$\dot{Q}_{gain} = \dot{Q}_{abs} - RecHL - SfPipeHL. \quad (2.20)$$

The predicted total useful energy gained by the HTF in the solar field is given by:

$$\dot{Q}_{SF} = \dot{Q}_{gain} * A_{SF}, \quad (2.21)$$

A_{SF} = total aperture area of the solar field [m²].

2.3.1.5 Solar conversion efficiency

One important parameter in evaluating the solar field performance is its ability to convert the solar energy into electricity, which is represented by solar conversion efficiency. It is reported that the solar conversion efficiency within the ISCCs can be calculated depending on the considered solar input whether incident solar radiation (solar radiation-to-electricity efficiency) or solar heat gain (solar thermal-to-electricity efficiency) [79].

The solar radiation-to-electricity efficiency which is calculated as:

$$\eta_{sol_rad} = \frac{\dot{W}_{elec,ISCC} - \dot{W}_{elec,CCGT}}{DNI * A_{SF}} = \frac{\Delta \dot{W}_{elec,ST}}{DNI * A_{SF}}, \quad (2.22)$$

The solar thermal-to-electricity efficiency which is calculated as:

$$\eta_{sol_heat} = \frac{\dot{W}_{elec,ISCC} - \dot{W}_{elec,CCGT}}{\dot{Q}_{SF}} = \frac{\Delta \dot{W}_{elec,ST}}{\dot{Q}_{SF}}, \quad (2.23)$$

where, $\dot{W}_{elec,CCGT}$ = the electrical power output of the ISCC without the solar field.

2.3.2 Exergy Analysis

Exergy-based performance analysis is the performance study of a system based on the second law of thermodynamics, which overcomes the limitations of studying the system based on the first law of thermodynamics. Exergy is a measure of the maximum useful work of a system as it proceeds to a specified final state in equilibrium with its surroundings, dead state. Exergy is destroyed in the system, not conserved as energy is.

Two different approaches are generally used to calculate the exergy efficiency of a system, one is called “brute force”, while the other is called “functional” [26].

The brute force form of exergy efficiency is used in this study. The brute force form requires accuracy and an explicit definition of each input and output exergy term before calculating the exergy efficiency as shown in **Table 2.6**.

The analysis was made with the following assumptions:

- The ISCC runs at steady state with a constant direct normal insolation.
- Pressure drop and heat loss in the plant pipelines except in the solar field are all neglected.
- Kinetic and potential energy changes are ignored.

So, the second law efficiency (η_{II}), exergetic efficiency, is given by:

$$\eta_{II} = \frac{\text{Exergy output}}{\text{Exergy input}}. \quad (2.24)$$

Table 2.6 Definitions of the exergy destruction and second law efficiency

Component	Exergy destruction	Second law efficiency (η_{II})
Pumps	$\dot{i}_{pump} = \dot{X}_{in} - \dot{X}_{out} + \dot{W}_{pump}$	$\eta_{II,pump} = 1 - \frac{\dot{i}_{pump}}{\dot{W}_{pump}}$
Heaters	$\dot{i}_{heater} = \dot{X}_{in} - \dot{X}_{out}$	$\eta_{II,heater} = 1 - \frac{\dot{i}_{heater}}{\dot{X}_{in}}$
Turbine	$\dot{i}_{turbine} = \dot{X}_{in} - \dot{X}_{out} - \dot{W}_{turbine}$	$\eta_{II,turbine} = 1 - \frac{\dot{i}_{turbine}}{\dot{X}_{in} - \dot{X}_{out}}$
Condenser	$\dot{i}_{condenser} = \dot{X}_{in} - \dot{X}_{out}$	$\eta_{II,condenser} = \frac{\dot{X}_{out}}{\dot{X}_{in}}$
Cycle	$\dot{i}_{cycle} = \sum_{\text{all components}} \dot{i}$	$\eta_{II,cycle} = \frac{\dot{W}_{net,out}}{\dot{X}_{cycle,in}}$

The net exergy transfer by heat (\dot{X}_{heat}) at the source temperature (T_s) and dead state temperature (T_0) is given by:

$$\dot{X}_{heat} = \sum (1 - \frac{T_0}{T_s}) \dot{Q}_s, \quad (2.25)$$

and, the specific exergy (Ψ) is given by:

$$\Psi = (h - h_0) - T_0(s - s_0), \quad (2.26)$$

where h , h_0 , s , and s_0 are the specific enthalpy, the specific enthalpy under the dead state condition, the specific entropy, and the specific entropy under the dead state condition, respectively.

Then, the total exergy rate associated with a fluid stream (\dot{X}) at the mass flow rate (\dot{m}) becomes:

$$\dot{X} = \dot{m} * \Psi = \dot{m}[(h - h_0) - T_0(s - s_0)]. \quad (2.27)$$

The exergy destruction rate in the ISCC as a whole (\dot{I}_{ISCC}) was obtained from:

$$\dot{I}_{ISCC} = \dot{I}_{compressor} + \dot{I}_{CC} + \dot{I}_{GT} + \dot{I}_{SF} + \dot{I}_{SFHex} + \dot{I}_{condenser} + \dot{I}_{CP} + \dot{I}_{FWP} + \dot{I}_{ST} + \dot{I}_{HRSG} . \quad (2.28)$$

2.3.2.1 The Exergetic Efficiency of the Solar Field

The solar heat input from the HTF (\dot{Q}_{HTF}) to the water in the solar field heat exchanger, according to the state points shown in **Figure 2.4**, is given by:

$$\dot{Q}_{HTF} = \dot{m}_{23}(h_{23} - h_{24}), \quad (2.29)$$

$$\dot{Q}_{water} = \dot{m}_{17}(h_{18} - h_{17}). \quad (2.30)$$

The exergy destruction rate in the solar field (\dot{I}_{SF}) is calculated from:

$$\dot{I}_{SF} = \dot{X}_{SF,in} - \dot{X}_{SF,gain} , \quad (2.31)$$

$$\dot{X}_{SF,gain} = \dot{X}_{23} - \dot{X}_{24} , \quad (2.32)$$

$$\dot{X}_{SF,in} = \dot{Q}_{SF} \left[1 - \left(\frac{T_0}{T_{sun}} \right) \right] , \quad (2.33)$$

where T_{sun} is the sun temperature, which equals 5777 K. The exergetic efficiency of the solar field ($\eta_{II,SF}$) is given by:

$$\eta_{II,SF} = \frac{\dot{X}_{SF,gain}}{\dot{X}_{SF,in}} . \quad (2.34)$$

2.3.2.2 The Exergetic Efficiency of the ISCC

The fuel chemical exergy per unit time (\dot{X}_{fuel}) equals:

$$\dot{X}_{fuel} = \zeta * \dot{Q}_{fuel} , \quad (2.35)$$

where ζ is the ratio of the chemical exergy to the net calorific value, which equals 1.04 for natural gas [80].

The exergetic efficiency of the ISCC ($\eta_{II,cycle}$) is given as:

$$\eta_{II,cycle} = \frac{\dot{W}_{elec,ISCC}}{\dot{X}_{ISCC,in}} , \quad (2.36)$$

$$\dot{X}_{ISCC,in} = \dot{X}_{SF,in} + \dot{X}_{fuel} . \quad (2.37)$$

2.3.1 The Measurement Devices in the Kuraymat Power Plant

Two meteorological stations with wind sensor, temperature sensor, and sun tracker sensor are installed in the solar field on-site with a free view of the horizon without obstructions and no reflections to the solar sensors. Their measured values are logged into tables which can be downloaded from the field supervisory control. The type and accuracy of the measurement instrumentation used in the ISCC power plant are mentioned in **Table 2.7**.

Table 2.7 Plant measurement devices and their accuracy

Parameter	Instrument	Uncertainty
Direct normal insolation	Tracked pyrheliometer	$\pm 2\%$
Global and diffuse irradiation	Pyranometer	$\pm 2\%$
Wind speed	Anemometer	± 0.3 m/s
Wind direction		$\pm 3^\circ$
Ambient temperature	Temperature and humidity sensor	± 0.5 °C
Relative humidity		@ -40 °C to $+60$ °C
Barometric pressure	Barometric pressure sensor	± 0.5 mbar @ -20 °C
Pressure	Digital transmitters	$\pm 1\%$
Temperature	RTD	± 0.95 K @ 400 °C
Volume flow	Ultrasonic flow meter	$\pm 0.3\%$
Mirror cleanliness	Portable specular reflectometer	$< 2\%$

2.4 Results and Discussion

The performance of the ISCC power plant was analyzed under different design conditions. The analyses were performed for different solar field thermal outputs, of 0 MW, 50 MW, and 75 MW, and different ambient temperatures, 5, 20, and 35 °C. All calculations were made based on design condition data.

The energy efficiency and the exergetic efficiency were calculated based on the heat input to the plant by the fuel and the sun.

2.4.1 Solar Field Model

The solar field model was validated using direct normal insolation in **Figure 2.7**, ambient temperature, solar field inlet temperature, and solar field volumetric flow rate data from the plant records. The mass flow rate of the heat transfer fluid is calculated from the sum of the volumetric flow rates as measured by the flow meter to the east and west solar fields, multiplied by the density of the heat transfer fluid at the measured average solar field temperature of inlet and outlet solar field temperatures [81].

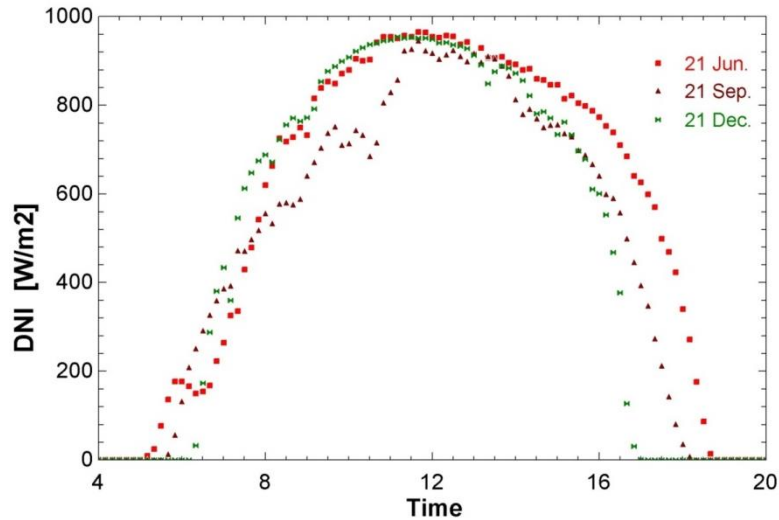


Figure 2.7 DNI measured at Kuraymat ISCC power plant on June 21, 2011; September 21, 2011, and December 21, 2011.

The total useful energy gained by the HTF in the solar field predicted by the model is compared to the observed total useful energy gained calculated from measured temperatures and flow rates (\dot{Q}_{HTF}) as recorded in the plant data, as shown in **Figure 2.8**.

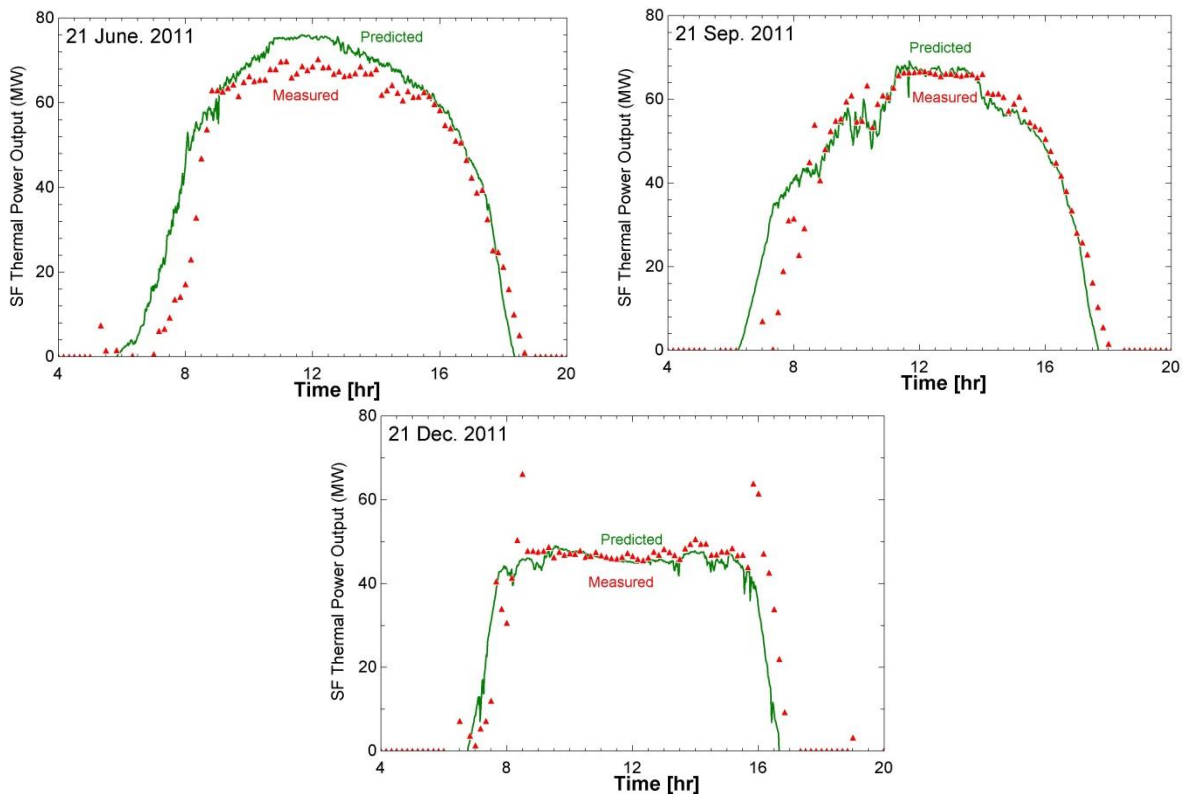


Figure 2.8 Measured and predicted thermal output from the solar field for (a) June 21, 2011, (b) September 21, 2011 and (c) December 21, 2011.

The results show a good agreement between the solar field thermal power output predicted from the model and the solar field thermal power output calculated using the plant records. This means that the model is trusted to be used in predicting the solar field performance at the different operating time.

Then, the solar model was used to study the influence of some parameters on the solar field performance. The absorbed energy by the receiver tubes (\dot{Q}_{abs}), the receiver and piping heat losses ($Rec \dot{Q}_L$ and $SF Piping \dot{Q}_L$, respectively) and the energy gained by the heat transfer fluid after thermal losses from the receiver and piping losses (\dot{Q}_{gain}), is compared in different seasons. The solar field performance was evaluated by thermal power output (\dot{Q}_{SF}) and thermal efficiency (η_{SF}). The parameters that thought to have an influence on the solar field performance were direct normal insulation (DNI), incidence angle (θ), and ambient temperature (T_{amb}).

Figure 2.9 shows the heat gain of the solar field in representative days of the seasons and the measured direct normal insolation is provided for reference. This figure shows that the highest heat gain is in summer while the lowest one is in winter. Also, the piping heat losses represent a very small value relative to the total heat losses. All energy rates shown in the figures are normalized on a per unit solar field aperture area basis, so their units are [W/m^2].

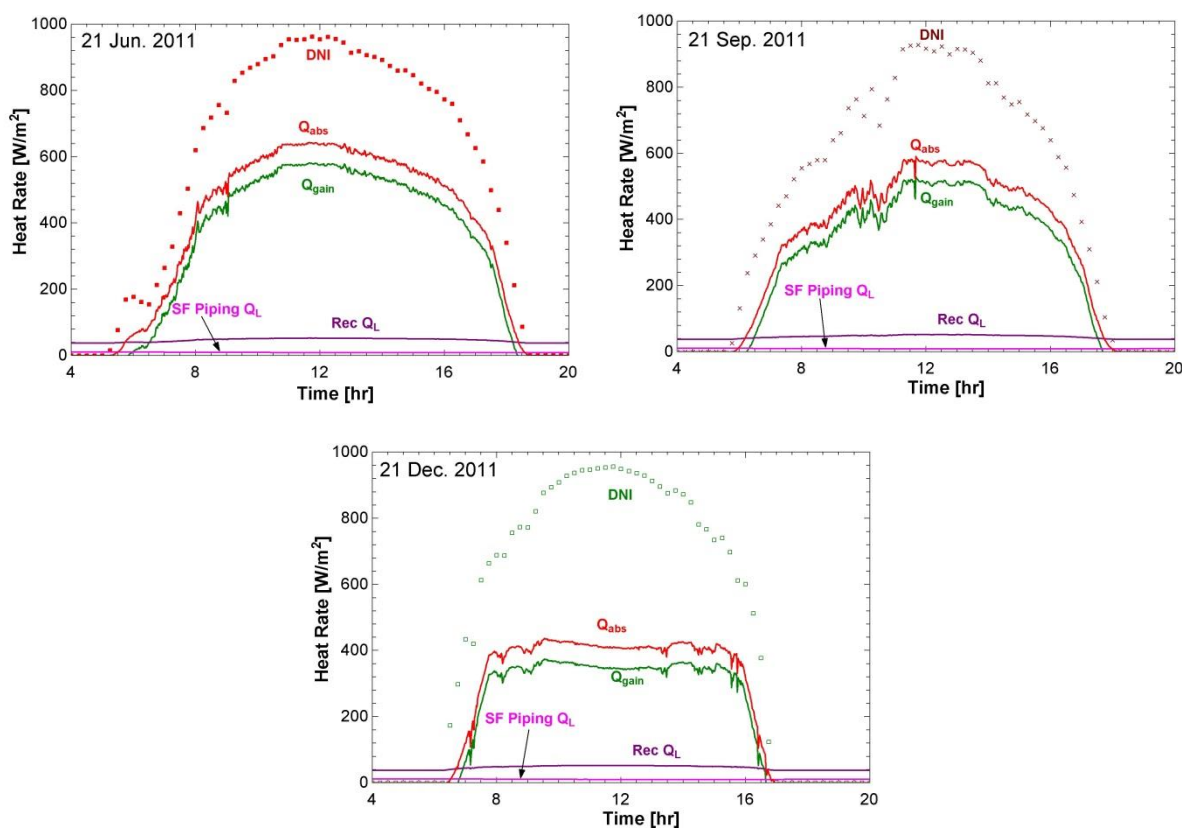


Figure 2.9 Rates of heat absorption and heat loss from the solar field for (a) June 21, 2011, (b) September 21, 2011, (c) December 21, 2011.

Figure 2.9 (a) and (b) show that the heat gain increases during the period of sunrise and reaches its peak value then decreases to sunset. However, **Figure 2.9** (c) shows that the heat gain is approximately constant during the period from sunrise to sunset. That may be due to the decrease of $\cos(\theta)$, as shown in **Figure 2.10**, in the heat absorbed equation, **Eqn. 2.5**.

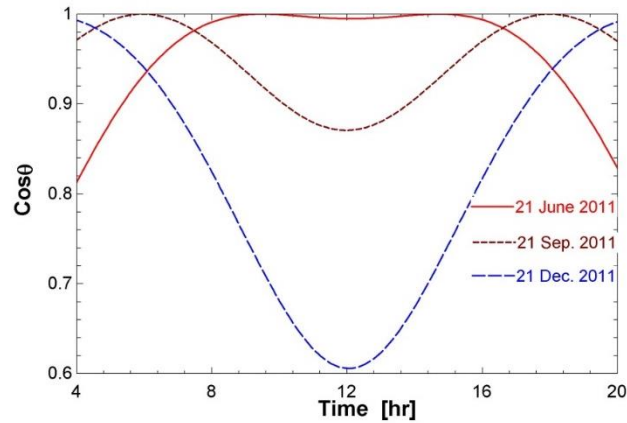


Figure 2.10 The value of $\cos \theta$ on June 21, September 21, and December 21.

From the seasonal comparison, integration of solar energy with the combined cycle power plant solved the problem of the electricity production drop in summer due to ambient temperature increasing where the solar field absorbs more energy in summer. Thus, ISCC has a stable energy production through the year.

The following figures (**Figure 2.11** through **Figure 2.14**) show the influence of the DNI and the incidence angle (θ) on both the solar field thermal power output and the solar field thermal efficiency. The study is carried out for June 21 in kuraymat, Egypt at 13:00 noon (LAT).

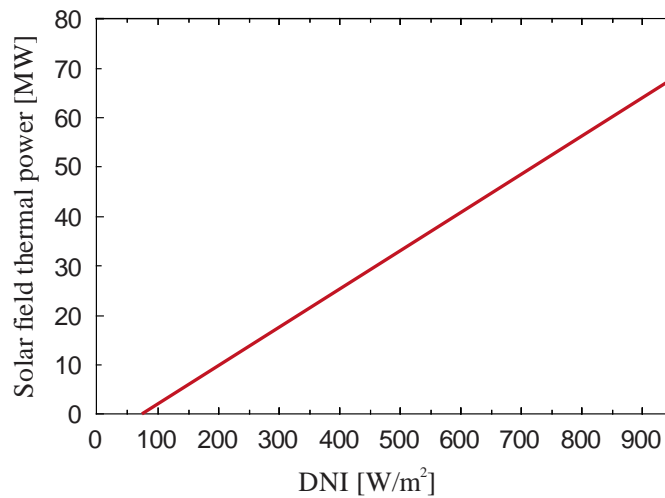


Figure 2.11 Solar field thermal power output vs. DNI.

The influence of DNI on both the solar field thermal power output and the solar field thermal efficiency for 21 June with ambient temperature of 35 °C is shown in **Figure 2.11** and **Figure 2.12**.

It is shown in **Figure 2.11** that the output power is directly proportional to the DNI. Where DNI increases, the heat absorbed by the HTF increases. To maintain the constant terminal temperature of the HTF, its mass flow rate should be increased which leads to increase of the solar field thermal output.

The solar field thermal efficiency increases with the increase of the DNI as shown in **Figure 2.11**. This may be explained as follows: the HTF operating with constant terminal temperatures (T_{in} and T_{out}). In case of the DNI increases, the HTF mass flow rate increases to maintain the same outlet temperature of the HTF. This means that the average density of the HTF and the cross-section area of the pipes remain constant. Which leads to increasing the heat transfer coefficient of the HTF by

increasing the velocity of the HTF due to increase the HTF mass flow rate, so the heat gain (\dot{Q}_{gain}) increases, hence the thermal efficiency increases.

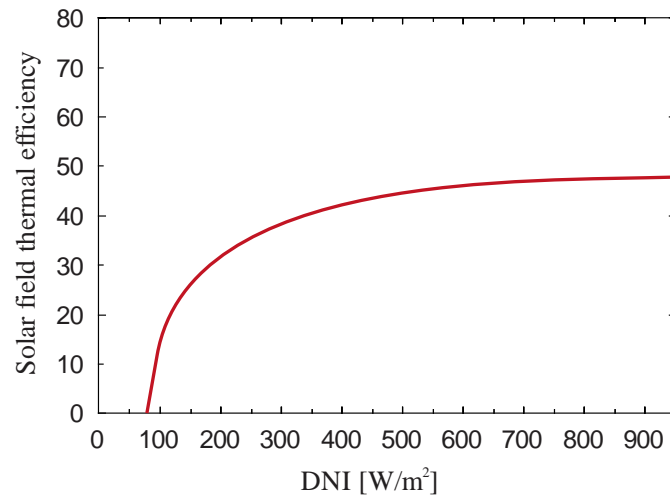


Figure 2.12 Solar field thermal efficiency vs. DNI.

The influence of the incidence angle (θ) on both the solar field thermal power output and the solar field thermal efficiency with DNI equal 950 W/m^2 and ambient temperature of $35 \text{ }^\circ\text{C}$ is shown in **Figure 2.13** and **Figure 2.14**. With increasing the incidence angle (θ), the solar field thermal power output decreases. That may be due to decrease amount of heat gain as a result of decreasing the reflected solar rays on the absorber tube which consequently leads to decrease of the solar field thermal power output.

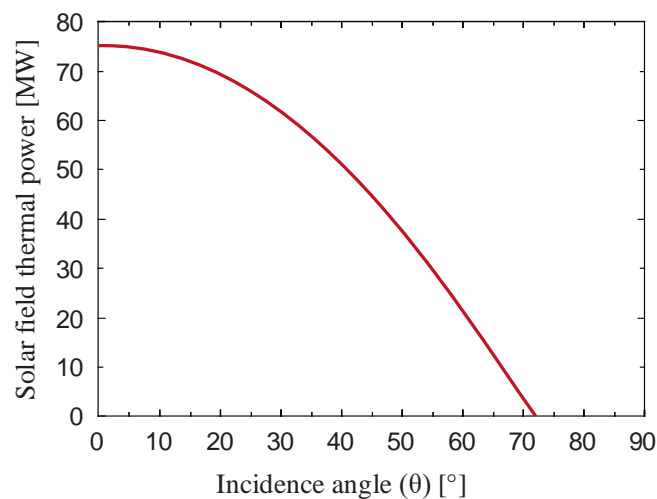


Figure 2.13 Solar field thermal power output vs. incidence angle.

The solar field efficiency decreases with the increase of the incidence angle (θ) as the thermal power output of the solar field which is clear from **Figure 2.14**. This figure shows that at $\theta = 70^\circ$ the thermal efficiency reaches zero. This may be explained as the heat gain (\dot{Q}_{gain}) is calculated using $\text{DNI} \cdot \cos(\theta)$ which means that the heat gain (\dot{Q}_{gain}) decreases with increasing the incidence angle (θ). So, the thermal efficiency decreases.

The results showed that the ambient temperature has no influence on the solar field thermal output. This can be explained as follows: the HTF has a constant terminal temperature which means that

the average temperature of the HTF is constant as well and the DNI is not affected by the ambient temperature. This may be because the ambient temperature affects the solar field heat loss which consists of two parts (receiver heat loss and solar field piping heat loss). Receiver heat loss (RecHL) is not affected by the ambient temperature [17]. Solar field piping heat loss (HL_{Piping}) represents a small fraction of the total heat loss so the efficiency is almost constant in this case. The same as the solar field thermal power output, the ambient temperature (T_{amb}) has no influence on the solar field thermal efficiency.

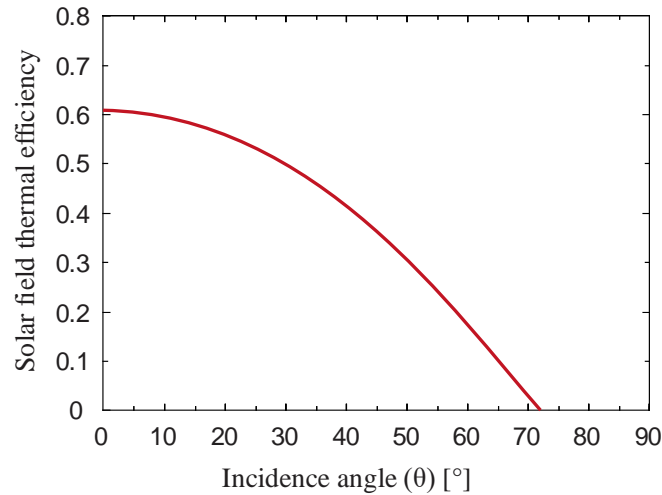


Figure 2.14 Solar field thermal efficiency vs. incidence angle.

2.4.2 Solar Conversion Efficiency

The variation of the solar radiation-to-electricity efficiency with the ambient temperature is shown in **Figure 2.15**. The figure illustrates that the ambient temperature has insignificant effect on the solar radiation-to-electricity efficiency. On the other hand, the figure depicts that the solar radiation-to-electricity efficiency increases with increasing the solar field heat input.

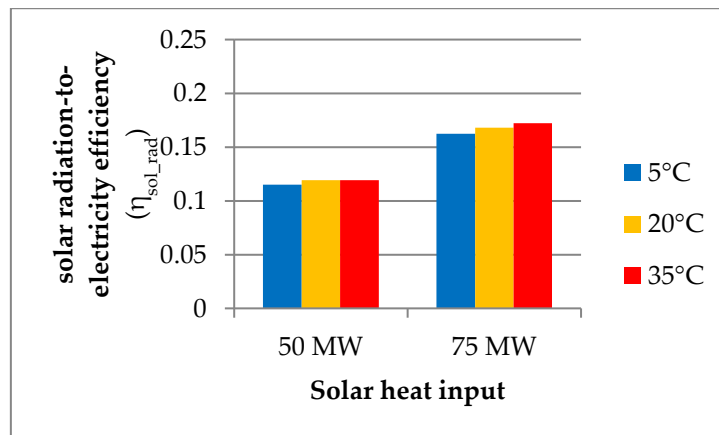


Figure 2.15 Solar radiation-to-electricity efficiency of the Kuraymat ISCC at different ambient temperatures for solar thermal heat input

The variation of the solar thermal-to-electricity efficiency with the ambient temperature is shown in **Figure 2.16**. It is obvious that the solar thermal-to-electricity efficiency increases slightly with increasing the ambient temperature.

It is clear that the value of the conversion efficiency from solar energy-to-electricity differs according to its definition as in **Figure 2.15** and **Figure 2.16**. For example, in the first definition (**Eqn. 2.22**) the value of the efficiency was 16.8% for solar heat input 75 MW at ambient temperature 20 °C, where it was 41% in the second definition (**Eqn. 2.23**) at the same conditions. It is believed that the first definition is more realistic than the second one as it represents the portion of the solar energy converted to electricity from the whole incident solar energy not from the solar heat gain.

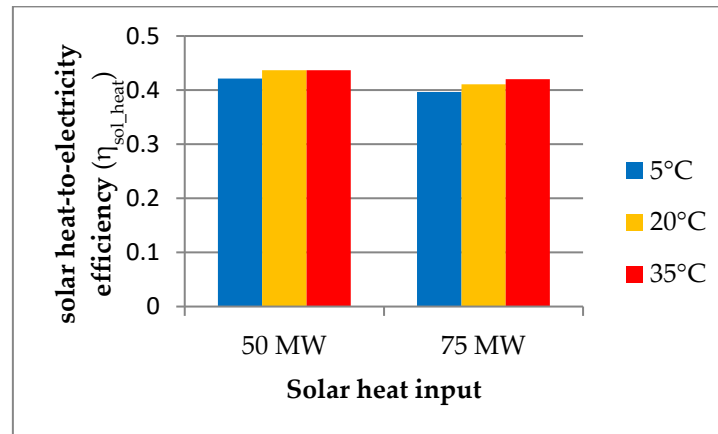


Figure 2.16 Solar thermal-to-electricity efficiency of the Kuraymat ISCC at different ambient temperatures for solar thermal heat input

2.4.3 Exergy Flow Diagram

The exergy rates and other properties at each state point are presented in **Table 2.8**. These values were calculated for actual plant measured data (pressure, temperature, mass flow rate and DNI) on 28 Aug. in Kuraymat at 2:00 PM, with DNI = 800 W/m². The T-s diagram of the Kuraymat Rankine cycle for the measurements at these conditions is shown in **Figure 2.17**.

The gas turbine and steam turbine electric power output of 62.19 MW and 51.94 MW, respectively, is obtained at the instance of recorded data with fuel consumption rate (\dot{m}_{fuel}) of 3.93 kg/s. The phase of each state point and the mass flow rates were illustrated in **Table 2.8**.

Table 2.8 Exergy rates and other properties at various locations of ISCCS, state numbers refer to **Figure 2.4**

State	Fluid	Phase	\dot{m} (kg/s)	P (bar)	T (°C)	h (kJ/kg)	s (kJ/kg·K)	\dot{X} (MW)
a	Air	Dead state	–	1.007	34.60	308.2	5.7300	–
0'	Water	Dead state	–	1.007	34.60	145.0	0.5000	–
0''	Oil	Dead state	–	1.007	34.60	35.2	0.1180	–
b	Fluegases	Gas	185.32	1.02	630.80	937.7	6.8500	52.508
c	Fluegases	Gas	185.32	1.01	87.60	361.6	5.8880	0.8100

State	Fluid	Phase	\dot{m} (kg/s)	P (bar)	T (°C)	h (kJ/kg)	s (kJ/kg·K)	\dot{X} (MW)
1	Water	Sat. water	49.01	1.007	38.40	160.6	0.5503	0.0004
2	Water	Liquid	49.01	9.36	38.90	163.9	0.5577	0.0474
3	Water	Liquid	49.01	1.20	38.90	163.6	0.5604	–
4	Water	Liquid	49.01	1.20	90.00	377.0	1.1920	–
5	Water	Liquid	49.30	1.20	104.80	439.3	1.3610	–
6	Water	Liquid	49.30	1.10	45.52	190.7	0.6453	3.9980
7	Water	Liquid	49.30	140.08	58.78	257.8	0.8090	0.8723
8	Water	Liquid	49.30	137.10	165.67	707.8	1.9840	5.2290
8,a	Water	Liquid	45.73	137.10	165.67	707.8	1.9840	4.8500
8,b	Water	Liquid	3.57	133.06	165.67	707.8	1.9840	0.3790
9	Water	Liquid	45.73	136.44	220.42	948.8	2.5010	8.5890
9,a	Water	Liquid	18.36	136.44	220.42	948.8	2.5010	3.4480
9,b	Water	Liquid	27.37	136.02	220.42	948.8	2.5010	5.1410
10	Water	Liquid	18.36	63.59	220.42	948.8	2.5190	3.3500
11	Water	Liquid	45.73	63.59	240.64	1041	2.7010	4.0060
12	Water	Sat. vapor	16.09	63.00	274.35	2785	5.8980	17.971
13	Water	Superheated	43.46	65.00	277.00	1220	3.0380	13.446
14	Water	Superheated	43.46	65.00	427.12	3237	6.5940	55.638
15	Water	Superheated	43.46	65.00	474.64	3355	6.7570	58.732
16	Water	Superheated	43.46	57.72	549.71	3542	7.0480	63.192
17	Water	Liquid	27.37	64.85	220.40	948.8	2.5180	4.9960
18	Water	Superheated	27.37	64.85	279.34	2780	5.8610	26.954
19	Water	Liquid	3.57	10.74	165.67	707.8	2.0150	0.3438
20	Water	Sat. vapor	4.37	10.74	183.00	2780	6.5620	2.7480
21	Water	Superheated	4.37	10.08	227.86	2892	6.8220	2.8600
21,a	Water	Superheated	2.10	9.97	227.86	2892	6.8220	2.8600
21,b	Water	Superheated	2.27	10.08	227.86	2892	6.8220	2.8600
22	Water	Sat.liq.vap.	45.56	0.08	32.60	2350	7.7120	0.0000
23	Oil	Liquid	205	17.00	393.00	784.6	1.6800	5.5110
24	Oil	Liquid	205	16.50	293.00	540.4	1.2840	30.023
25	Water	Liquid	3925	1.01	28.81	120.8	0.4200	0.9080
26	Water	Liquid	3925	1.05	28.81	120.8	0.4200	0.9226
27	Water	Liquid	3925	1.013	38.26	160.3	0.5489	0.3568

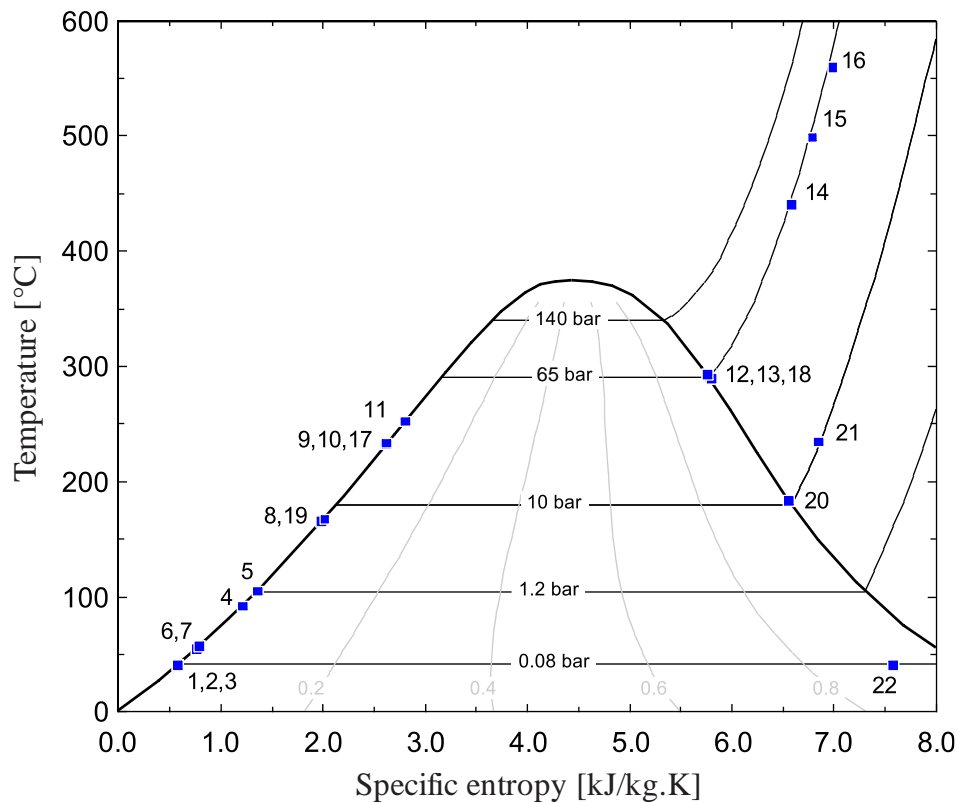


Figure 2.17 The T-S diagram for the Rankine cycle of the Kuraymat ISCC power plant

The enthalpy at state point (22) which represents the exhaust steam from the low pressure steam turbine section to the condenser is taken according to the design data of the plant. The rates of exergy destruction, percent of exergy destruction and the second law efficiency of the main components in the ISCC power plant were calculated using data on **Table 2.8**. The exergetic efficiency of the Kuraymat ISCC power plant at combined cycle regime is calculated at the same conditions used with the plant at the ISCC regime.

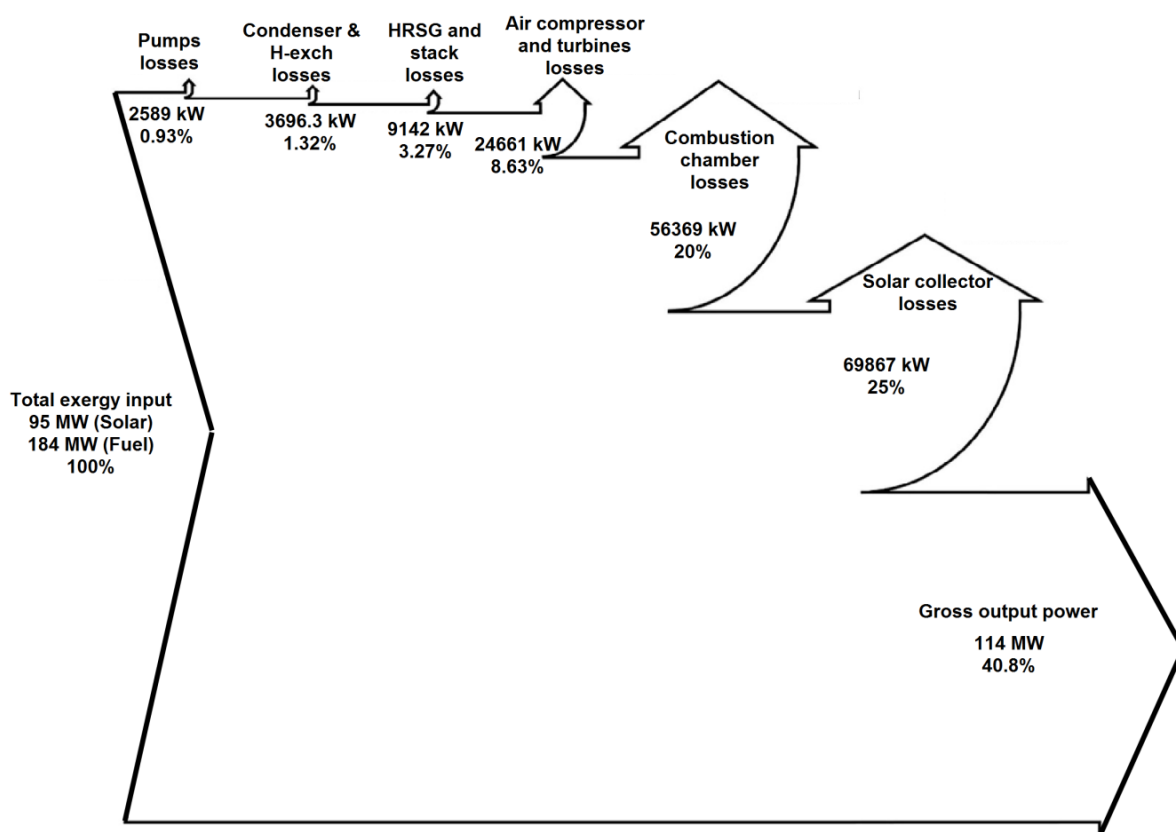
The efficiency of the Kuraymat ISCC power plant has higher efficiency at combined cycle regime than at ISCC regime as shown in **Table 2.9**. That may be due to the existence of solar field which need precise design optimization of solar energy integration in a combined cycle power plant.

The exergy flow diagram, given as the percentage of total exergy input for the ISCC power plant is shown in **Figure 2.18**. This figure reveals that the maximum exergy destruction occurs in the solar collector and the combustor.

Then, the performance of the ISCC power plant was analyzed for different design conditions. The analysis was performed at different solar field thermal output (75, 50 and 0 MW) and a different ambient temperature (5, 20 and 35 °C). In addition to energy and exergy efficiencies, the following parameters were evaluated for the plant components: exergy destruction in different components of the ISCC of the plant, percentage of exergy destruction in different components of the ISCC to the total of exergy destruction of the plant and the percentage of exergy destruction in different components of the ISCC to the total exergy input to the plant. The energy efficiency (overall thermal efficiency) and the exergetic efficiency (second law efficiency) were calculated based on the heat input to the plant by the fuel and the sun.

Table 2.9 Exergy, percent of exergy destruction and the second law efficiency of different components of the ISCC

Sub-system		\dot{i}_{des} [MW]	$\dot{i}_{des} / \dot{i}_{total}$ [%]	η_{II} [%]
Solar field	PTCs	69.87	0.42	26.42
	Heat exchanger	3.13	1.89	94.79
Combined cycle	Gas turbine	7.58	4.57	95.00
	Combustion chamber	56.37	34.00	78.29
	Air compressor	7.32	4.42	91.15
	Steam turbine	9.76	0.59	85.22
	Condenser	0.57	0.34	38.68
	Condensate pump	0.11	0.01	30.00
	Feed water pump	2.48	1.50	25.15
Combined cycle power plant	HRSG	8.33	5.03	89.63
	Stack	0.81	0.49	–
	Combined cycle power plant	–	–	64.00
ISCC power plant	–	–	40.58	

**Figure 2.18** Exergy flow diagram, given as the percentage of total exergy input for the ISCCS

2.4.4 Overall Thermal Efficiency of the ISCC Power Plant

The overall thermal efficiency of the ISCC power plant in Kuraymat at different ambient temperatures for solar heat inputs of 0 MW, 50 MW, and 75 MW is shown in **Figure 2.19**. The overall thermal efficiency of the power plant at different ambient temperatures for solar heat input equal to 0 MW, which represents the combined cycle regime, is shown in **Figure 2.19**. In the combined cycle regime, the thermal efficiency of the plant was reduced from 51.14% at ambient temperature 5 °C to 48.67% at 35 °C. **Figure 2.19** shows that the overall thermal efficiency of the ISCC decreases with increasing ambient temperature at different solar heat inputs, of 0, 50, and 75 MW, and that appears most distinctly at ambient temperature 35 °C. This may be due to the direct effect of the ambient temperature increase on the efficiency of the condenser and the gas turbine: the condenser and gas turbine efficiency decreases with increasing ambient temperature.

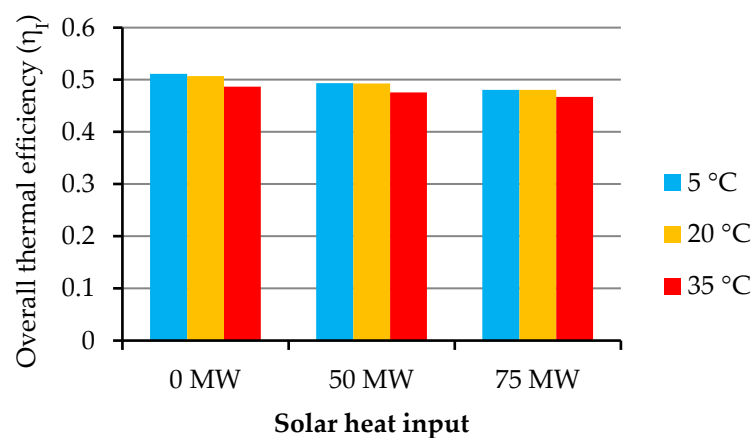


Figure 2.19 The overall thermal efficiency of the power plant at different ambient temperatures for different solar heat inputs

The overall thermal efficiency of the ISCC is lower than the overall thermal efficiency of the plant in the combined cycle regime in all cases, different solar heat inputs and ambient temperatures. **Figure 2.19** shows that the integration of the solar field with the combined cycle reduced the thermal efficiency of the power plant at all ambient temperatures. This may be because the target of the ISCC is not to increase the overall thermal efficiency of the combined cycle but to increase the economic feasibility of the solar power plants. Elimination of the thermal storage system reduces the cost of the power plant [82]–[84].

2.4.5 Exergy Destruction in Each Component of the ISCC

The exergy destruction in each component of the ISCC and the exergy destruction in the whole ISCC were calculated for different solar heat inputs and ambient temperatures of 5 °C, 20 °C, and 35 °C. The percentages of exergy destruction in each component of the ISCC out of the total exergy destruction of the power plant at different ambient temperatures for solar heat inputs 0 MW, 50 MW, and 75 MW are shown in **Figure 2.20**, **Figure 2.21** and **Figure 2.22**, respectively.

It is revealed in **Figure 2.20** that the combustion chamber (CC) has the highest percentage of exergy destruction, and this value is higher in the combined cycle regime than in the ISCC regime. This may ensure that the solar field has a high irreversibility weight, which affects the percentage

of exergy destruction in the combustion chamber compared to its value in the combined cycle regime. However, **Figure 2.20** shows that the exergy destruction in the combustion chamber decreases slightly with the increase of the ambient temperature under the combined cycle regime, 0 MW solar heat input.

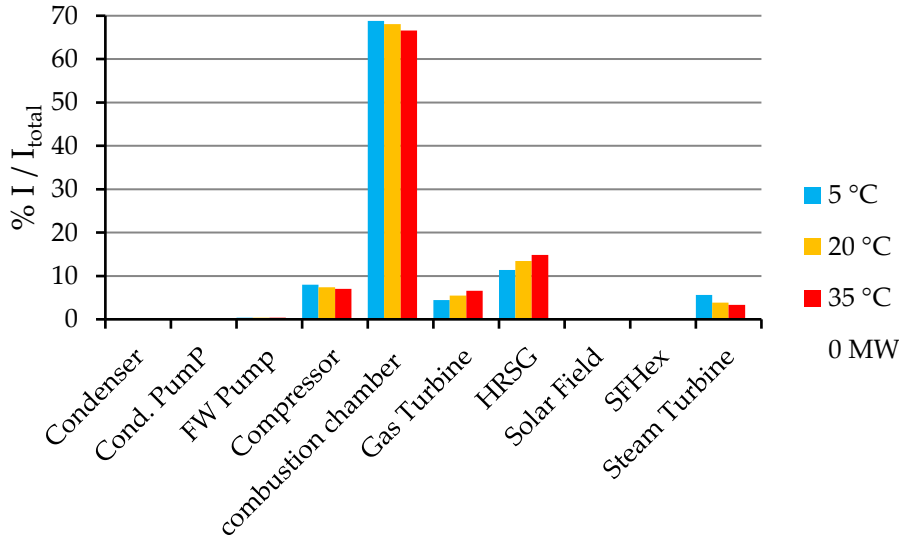


Figure 2.20 Exergy destruction in each component of the ISCC to the total exergy destruction of the plant at different ambient temperatures for solar heat input equal to 0 MW

It can be observed from **Figure 2.21** and **Figure 2.22** that the exergy destruction in the combustion chamber decreases significantly with the increase of the ambient temperature in the case of ISCC. This may account for the weight of exergy destruction in the solar field. Also, the exergy destruction in the solar field increases with increasing ambient temperature, in contrast to the exergy destruction in the combustion chamber.

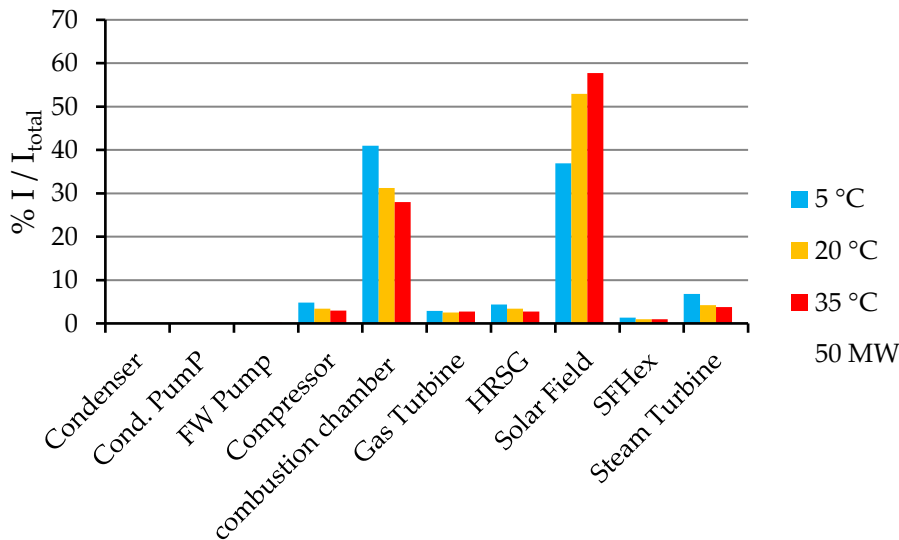


Figure 2.21 Exergy destruction in each component of the ISCC to the total exergy destruction of the plant at different ambient temperatures for solar heat input equal to 50 MW

Figure 2.20, **Figure 2.21**, and **Figure 2.22** show that the combustion chamber and the solar field have the highest exergy destruction among all the subsystems. This is valid for all cases of solar

heat input. It was also revealed from the values at different ambient temperatures that the exergy destruction of the solar field decreases with increasing solar thermal input.

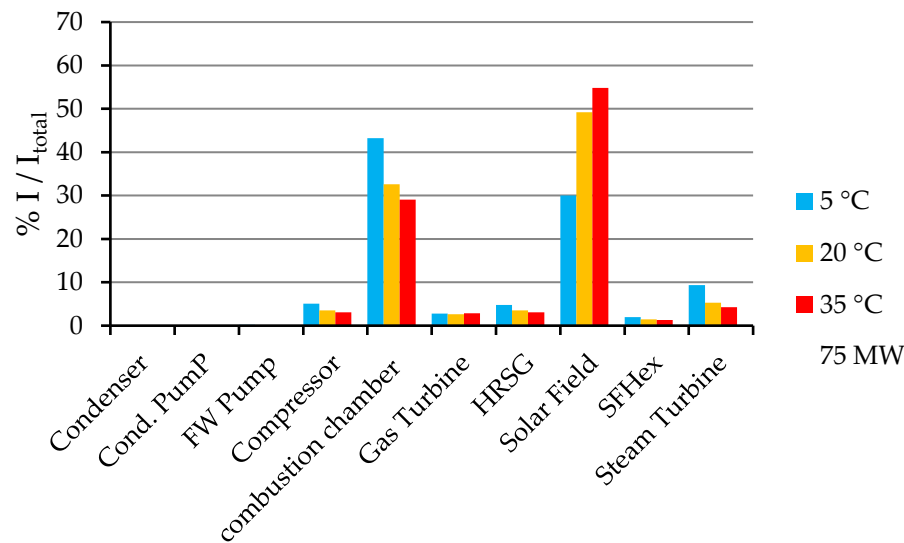


Figure 2.22 Exergy destruction in each component of the ISCC to the total exergy destruction of the plant at different ambient temperatures for solar heat input equal to 75 MW

2.4.6 Exergetic Efficiency of the Main Components of the ISCC

The exergetic efficiency of different components of the ISCC at different ambient temperatures for solar heat inputs 0 MW, 75 MW, and 50 MW is shown in **Figure 2.23**, **Figure 2.24** and **Figure 2.25**, respectively.

Figure 2.23 depicts the exergetic efficiency of different components of the ISCC at different ambient temperatures in the absence of the solar field, under the combined cycle regime. Under the combined cycle regime, the condenser has the lowest exergetic efficiency except at ambient temperature 5 °C. That may be due to the decrease in the low-temperature reservoir which increases the heat dissipated to the condenser cooling water.

The exergetic efficiency of the solar field decreased from 31.3% to 14.5% when the ambient temperature increased from 5 °C to 35 °C, as shown in **Figure 2.24**. The condenser exergetic efficiency also decreased from 75.5% to 19.3% when the ambient temperature increased from 5 °C to 35 °C for solar heat input equal to 50 MW. This may be due to the decrease in the temperature difference between the exhausted steam from the low-pressure turbine and the cooling water from the cooling tower.

Figure 2.25 shows that the exergetic efficiency of the solar field decreased from 47% to 21.7% when the ambient temperature increased from 5 °C to 35 °C. The condenser exergetic efficiency also decreased from 65.8% to 19.3% when the ambient temperature increased from 5 °C to 35 °C for solar heat input equal to 75 MW.

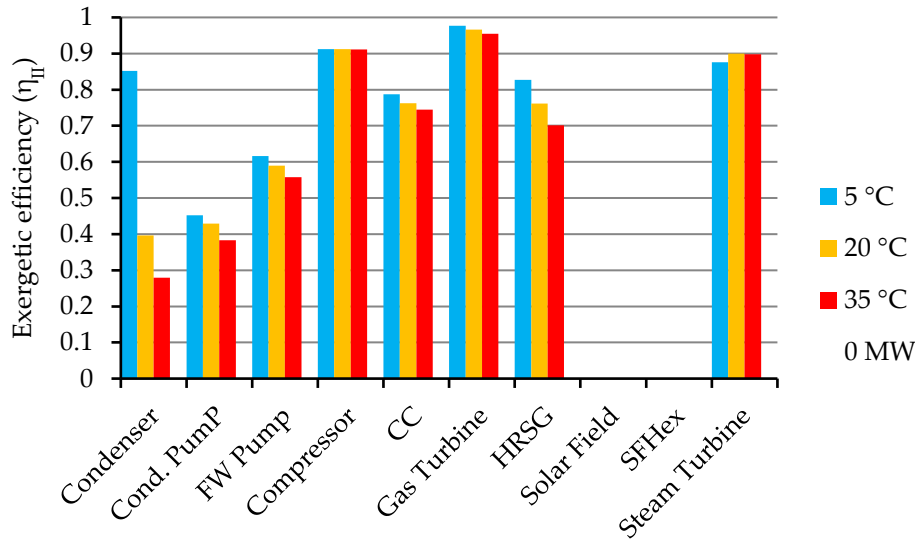


Figure 2.23 Exergetic efficiency of different components of the ISCC at different ambient temperatures for solar heat input equal to 0 MW

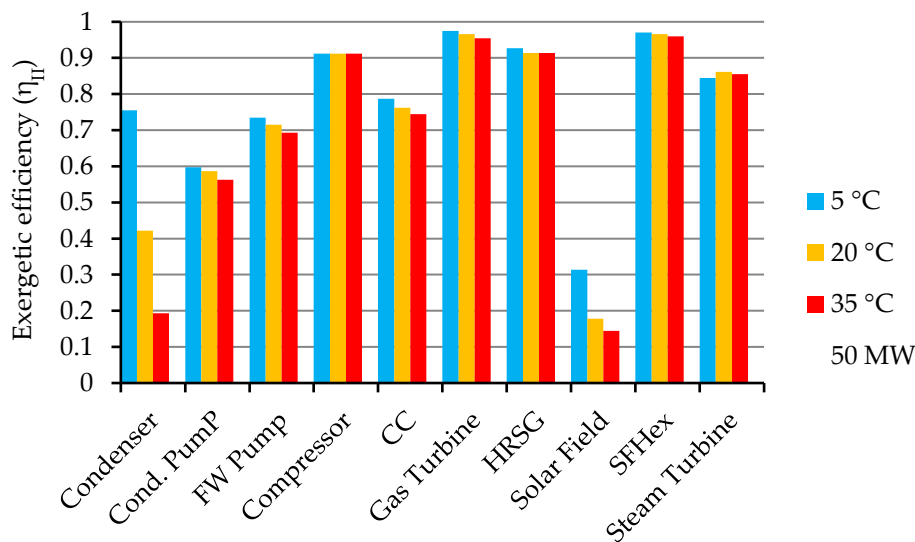


Figure 2.24 Exergetic efficiency of different components of the ISCC at different ambient temperatures for solar heat input equal to 50 MW

Unlike the thermal efficiency [81], the exergetic efficiency of the solar field explicitly decreased with increasing ambient temperature, as shown in **Figure 2.24** and **Figure 2.25**. This may be due to the increase of the exergy destruction in the solar field with increasing ambient temperature, as shown in **Figure 2.21** and **Figure 2.22**.

As shown in **Figure 2.23**, **Figure 2.24**, and **Figure 2.25**, the exergetic efficiency of the HRSG decreased with increasing ambient temperature, and this may be due to the existence of the attemperators in the HRSG which limit the steam temperature to the setpoint value. In the HRSG installed in the Kuraymat power plant, attemperators were installed at the surface of the superheaters to control the temperature at the inlet of the high-pressure steam turbine. These attemperators use water directly from the main feedwater pump of the power plant. An increase in the ambient temperature may lead to an increase in the flue gas temperature of exhaust from the

gas turbine into the HRSG, and the attemperators limit the effect of this temperature increase on the temperature of the superheated steam going into the steam turbine using water directly from the main feedwater pump. This may be a reason for the decreasing exergetic efficiency of the HRSG with increasing ambient temperature as shown in **Figure 2.23**, **Figure 2.24** and **Figure 2.25**.

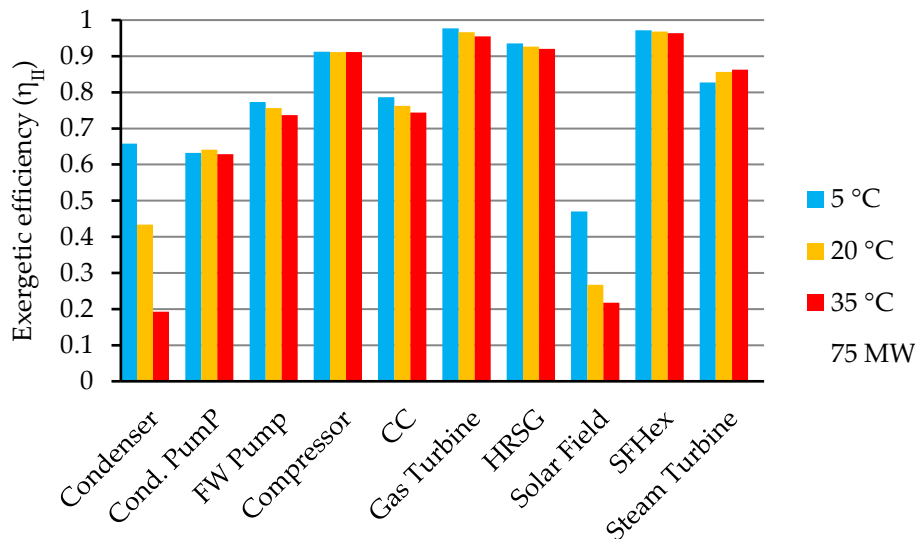


Figure 2.25 Exergetic efficiency of different components of the ISCC at different ambient temperatures for solar heat input equal to 75 MW

2.4.7 Exergetic Efficiency of the ISCC Power Plant

The exergetic efficiency of the ISCC power plant was calculated for different solar heat power inputs. The comparison was implemented at three different ambient temperatures: 5, 20, and 35 °C. The ISCC power plant exergetic efficiency for solar heat inputs 0 MW, 50 MW, and 75 MW at different ambient temperatures are depicted in **Figure 2.26**. The exergetic efficiency of the ISCC power plant was calculated based on the design condition data for the different solar heat power inputs. **Figure 2.26** reveals that the exergetic efficiency of the ISCC power plant is inversely proportional to the ambient temperature, where it decreased from 47.2% to 46% with increasing ambient temperature from 5 °C to 35 °C for solar heat input equal to 75 MW. In addition, it decreased from 48.2% to 46.58% when the ambient temperature increased from 5 °C to 35 °C for solar heat input equal to 50 MW.

Figure 2.26 also illustrates the exergetic efficiency of the combined cycle regime (solar heat input equal to 0 MW) at different ambient temperatures. In the absence of the solar field, the exergetic efficiency of the plant reached 49.18% and 47.21% at ambient temperatures 5 °C and 35 °C, respectively. This demonstrates that the exergetic efficiency of the ISCC power plant in Kuraymat has higher efficiency under the combined cycle regime than under the ISCC regime, as shown in **Figure 2.26**. This may be due to the existence of the solar field, which needs precise design optimization of solar energy integration in a CCGT power plant.

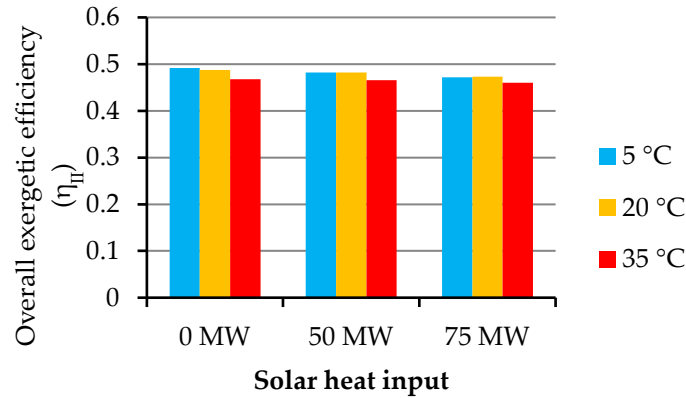


Figure 2.26 ISCC power plant exergetic efficiency at different ambient temperatures for different solar heat inputs

Like the overall thermal efficiency, the exergetic efficiency of the ISCC power plant decreased with increasing ambient temperature, mainly at an ambient temperature of 35 °C. This may be due to the sharp decrease in the exergetic efficiency of the condenser and the solar field with increasing ambient temperature, as shown in **Figure 2.23**, **Figure 2.24** and **Figure 2.25**. These figures also show that the exergetic efficiency of the gas turbine and the HRSG decreased with increasing ambient temperature, and that also affected the exergetic efficiency of the ISCC power plant, as shown in **Figure 2.26**.

2.4.8 Investigating the Sources of Exergy Destruction

From the attained results, it is clear that the amount of exergy destruction in the various components of the ISCC is altered. This variation is assumed to be due to different reasons such as the type of device, the process, etc.

Moreover, the results showed that the combustion chamber and the solar field represent the sites of highest exergy destruction in the ISCC. In this section, an attempt is made to explore and clarify the sources of exergy destruction in each component in order to identify the possibility to enhance the performance of the components of major exergy destruction.

2.4.8.1 Irreversibility in the Solar Field

The exergy destruction in the solar field is due to heat transfer between the sun and the absorber, heat transfer between the absorber and the HTF, and the friction of the viscous HTF. The exergy loss is due to the optical efficiency, the ratio of sunlight capture to incident sunlight, and the heat transfer to the surroundings.

The solar collector is considered to be the main source of exergy destruction in the solar field due to the high-temperature difference in the collector. The major contribution to the exergy destruction in the solar collector is due to the heat transfer between the sun and the absorber, while the major exergy loss occurs due to optical errors [85].

It was reported that exergy destruction due to heat transfer between the sun and the absorber accounts for 35% to 40% of the total exergy destroyed. Exergy losses to the surroundings account for 5% to 10% of the total exergy destroyed [85].

It is thought that to decrease the exergy losses from the solar collector, increase the collector energetic efficiency, attention should be pointed toward improving the optical parameters of the collector such as mirror reflectivity, the transmissivity of the glass envelope, absorptivity of the heat collection element (HCE) selective coating, and the focal length of the collectors etc.

Regarding the exergy destruction due to heat transfer, improving that part may involve great challenges because of the existence of the finite temperature differences which are essential for the heat transfer process and cannot be avoided.

2.4.8.2 Irreversibility in the Combustion Chamber

The combustion process is complex. Thus, the entropy generation during the combustion process is rather high due to the complexity of that process. It was reported that oxidation of fuel during the combustion process utilizes around 1/3 of the usable fuel energy [86]. This feature of the combustion process causes it to have the highest exergy destruction. The combustion process includes diffusion, chemical reaction, heat transfer, friction, and mixing. To implement all of these subprocesses, a considerable amount of the available energy is consumed. Most of this energy is unreachable, combustion activation energy, mixing, and diffusion. There are three major physicochemical subprocesses responsible for entropy production during the combustion process [86]:

- Diffusion of reactants, mixing of fuel and air molecules, and chemical reaction, fuel oxidation, where energy is consumed to overcome the activation energy.
- Heat transfer between combustion products and other neighbors of particles is called internal thermal energy exchange.
- Mixing of combustion products with other constituents.

These processes cause exergy destruction and thus result in a reduction in the system exergy. On one hand, all these processes destroy up to 40% of the useful exergy of the fuel. On the other hand, it was found that the dominant process of exergy destruction is the internal thermal energy exchange process. It was found that more than 2/3 of the exergy destruction in the combustion process occurs at the internal thermal exergy exchange process, while fuel oxidation is responsible for up to 30% of the exergy destruction, and the exergy destruction due to the mixing process is about 3% of the total exergy destruction of the combustion process [86].

The thermodynamically irreversible combustion process is path-dependent. To get a quantitative solution for the total entropy production during the combustion process, correct information of the sequence of the combustion process and reactions must be offered.

Many factors affect the exergy destruction in the combustion chamber. For example, the exergy destruction decreases with decreasing excess air and increasing preheating temperature. Mixing at a large temperature difference leads to high exergy destruction [87]. Also, the exergy destruction of the combustion chamber is affected by the molecular structure of the fuel, where the exergy destruction of the combustion chamber increases with the increase of the hydrocarbon chain length [88]. An attempt was made to avoid this heat transfer by introducing the concept of reversible combustion, where it was proposed theoretically to preheat the reactants to the equilibrium temperature and partial pressures without a reaction, but it could not be achieved in practice [86].

The major exergy destruction in the combustion chamber occurs during the phase of the internal thermal energy exchange between the system particles [86]. The unavoidability of the internal thermal energy exchange makes reducing the exergy destruction during the combustion process very difficult.

2.4.8.3 Irreversibility in the heat exchangers

The sources of exergy destruction in heat exchangers are fluid friction (leads to pressure losses), heat transfer between hot and cold flows (due to temperature difference), energy dissipation to the surroundings (heat transfer between the heat exchanger and its surroundings), production of the material (Exergy destruction varies directly with the roughness level) and construction of heat exchanger [89]. Dissipation to the environment is usually of minor effect and can be neglected when the heat exchanger operates at a temperature close to the surrounding's temperature [90]. Exergy destruction due to fluid friction increases with increasing fluid viscosity and velocity [91], [92]. The effect of a frictional pressure drop on the exergy destruction is small compared to the effect of heat transfer due to temperature difference[93].

2.4.8.4 Irreversibility in the gas turbine

The main sources of exergy destruction in the gas turbine are thought to be due to the friction and the heat transfer between the flue gases and the turbine blades. The time taken by the fluid during friction and heat transfer in the turbine is very short, so this may render the exergy destruction in the gas turbine to be not significant as in the combustion chamber. This may explain why the gas turbine has low exergy destruction compared with the combustion chamber. In the compressor, the mechanism of flow and interaction is the same as in the case of the gas turbine. Thus, it is thought that the exergy destruction in the compressor has the same weight as the gas turbine compared to the weight of exergy destruction in the combustion chamber. By the same way, the exergy destruction in the steam turbine can be interpreted.

2.4.8.5 Irreversibility in the steam turbine

Exergy destruction in the steam turbine is governed by construction and design features. The transition of flow between stages and leakage around turbine blades tips and through seals play a major role. So, this type of losses can be recovered to some extent and differs from the features of the exergy losses in the combustion chamber.

Chapter 3: Dynamic Process Simulation of ISCC

In this chapter, a sophisticated dynamic process model representing the Kuraymat ISCC power plant in Egypt was developed using APROS software. All processes and automation are modelled according to the specification of the reference plant. Moreover, actual measurements from the reference plant are used for model validation. The study includes measurement validation to analyze the influence of modelling assumptions on simulation results. The simulation results such as the electrical power output, the pressure, the temperature, and the mass flow rate were compared with the actual measurements, showing good agreement. And such a detailed dynamic validation is not available in the literature.

3.1 Introduction

Mathematical modelling complements the measurement work to better comprehend the principle, performance, and limitations of the energy systems and contributes to improving its efficiency. The mathematical modelling can be categorized as steady-state simulation and dynamic simulation. The steady-state simulation, like the energy and exergy analysis in the previous chapter, usually used in the design and optimization of energy systems based on the mass, momentum, and energy conservation equations in addition to empirical correlations for heat transfer and friction in so-called thermal-hydraulic models. However the steady-state simulation is only performed for a series of steady-state points and does not provide any information during the transients, the path between the steady-states may lead to a plant trip. Thus, a relevant next step is to analyze the process using dynamic simulation during transients, load changes, and malfunctions. Unlike the steady-state simulation, the dynamic simulation considers the time derivatives. It is a useful tool throughout the entire service life of a power plant, from proposal to decommissioning. It is a robust and cost-efficient tool for the prior assessment of radical operability and controllability of a power plant via the design and testing of control structures, operating procedures, and protective and relief devices. In contrast to steady-state process simulation, dynamic process simulation enables detailed acquisition of plant behavior during transients (e.g. load changes, disturbances, start-up and shutdown phases, etc.) with the associated control systems. Dynamic simulation is a feasible way to evaluate the limitations and capabilities of the power plants and their control structures [94]. This requires the accuracy of the model in representing the power plant and the efficiency of the simulation software. The accurate characterization of the system components and automation structures are essential for obtaining a meaningful dynamic response. The requirements for an accurate model are extremely complex. To be able to achieve the highest possible degree of accuracy, not only must the individual subsystems be optimally physically coordinated, but the behavior of components, material properties and control mechanisms must also be precisely coordinated.

Considering the limited existing work, this work contributes to bridging the knowledge gap in the dynamic simulation of ISCC power plants. However, most reviewed studies so far suffer from the fact that the developed dynamic models are not validated using actual measurements. In this study, a sophisticated dynamic process model representing the Kuraymat ISCC power plant in Egypt was developed using APROS software. All processes and automation are modelled according to the

specification of the reference plant. Moreover, actual measurements from the reference plant are used for model validation. The study includes measurement validation to analyze the influence of modelling assumptions on simulation results. The simulation results such as the electrical power output, the pressure, the temperature, and the mass flow rate were compared with the actual measurements, showing good agreement.

In the literature, the dynamic process simulation of ISCC power plants is less presented than the steady-state process simulation. Such a detailed dynamic validation is not available in the literature. The dynamic simulation validation is a key aspect to evaluate these ISCC power plants realistically and reliably to make a well-founded decision on their technological feasibility. In particular, a few studies that have addressed the dynamic simulation complemented their models with actual measurement validation.

This chapter is organized as follow: the developed dynamic process simulation model is presented and all assumptions used are summarized and discussed. Then, the model was tuned and steady-state validated using operational design data of the reference plant. The tuned model was then validated again using actual measurements of four different days by comparing the simulation results of the main parameters (electrical power, pressure, temperature, and mass flow rate) with their actual measurements. Finally, the main results of this investigation are highlighted in the conclusion section.

3.2 Mathematical Modelling

The model predicts the solar field heat output which is used as additional heat input to the heat recovery steam generator (HRSG), thus increasing the electrical power output and reducing the carbon emissions. A full-scale dynamic model of the Kuraymat ISCC power plant is developed using the **Advanced PROcess Simulation (APROS)**. It is a dynamic process simulator established for the representation of thermal power plant processes and the creation of realistic system-specific simulators. APROS developed by the Technical Research Centre of Finland (VTT) and Fortum Nuclear Services Ltd. It contains component libraries for dynamic modeling, of the process, automation and electrical systems, of thermal power plants, energy and industrial processes.

The modelling is based on the solution of dynamic conservation equations for mass, momentum, energy, where the calculations are solved simultaneously for the entire model network. Steam properties are calculated as a function of pressure and enthalpy, using the steam tables based on IAPWS-IF97 as a basis. Combustion and other relevant chemical reactions are modelled by APROS thermal-hydraulic models. The integrated model library contains components for the simulation of turbine plants, boilers, auxiliary systems, analogue, or binary automation and various electrical systems, which are used for modelling by drag and drop. Inserted components have to be initialized individually and connected by connecting lines to a P&I diagram. Calculated variables are stored in semantic databases and can be visualized in diagrams for monitoring purposes or exported for further use.

In APROS, a thermodynamic model is used to calculate pressure, mass flow, and enthalpy in six accuracy levels (model 0 to module 6).

Model 0: Mass flows in the inserted components are initialized by the user and not solved from the pressure dynamics. It is a sequential solver that solves mass and energy balances for each

component individually, neglecting pressure losses. Material properties are solved as a function of pressure, enthalpy, and mass fraction of the components.

Model 1: The mass flow is modelled. In contrast to model 2, pressure, flow and enthalpy are calculated using simplified equations, but without iteration. Influences of material properties are only slightly considered. In this model, heat transfer between the fluid and the components used is not simulated.

Model 2: It is assumed that the fluid is a homogeneous mixture of liquid and gas. In the calculation of the system, the thermal structure of the components is taken into account as well as the hydraulic node pressures, flows and enthalpy. The heat transfer between fluid and components is simulated.

Model 5 to 6: These modules are similar in scope to Model 2, simulating the thermal structure, node pressures, flow, and enthalpy. The mass fluxes and enthalpy are calculated for the liquid and gas in separate phases. The heat transfer between the two phases and the components is simulated.

The thermohydraulic network forms a dual network structure together with the design network, where the design network functions independently of the selected thermohydraulic accuracy. The design network determines the concentration of the fluid and the material properties of the process parts in the simulation environment. This network structure allows the thermodynamic flow model to be extended to include processes with fluids other than water and steam.

Before the flow system can be started, the initial state must be defined in the initialization phase. This step must be repeated as soon as the system is extended or modified. The focus of the initialization is on the calculation of the initial state values. Here, index tables and geometric values of the process components are defined, which describe the network structure. In this context, instructions are given for defining the simulated process using the thermohydraulic elementary components of the calculation level. After the system is initialized, the simulation can be started and the solutions for temperature, hydraulic node pressure, mass flow, and enthalpy can be calculated. If model 2-6 is used, final values are calculated iteratively by the main program, since the material properties of water and steam cannot be calculated implicitly.

The simulation created in this work is performed under model 2 conditions (homogeneous flow model). Conventional power plants have already been successfully simulated under this assumption. APROS models for thermal power plant technologies are commonly found in the literature. Most models have been validated by actual measurement, which confirms their accuracy and readability, such as the CCGT power plant [95]–[99], and CSPP [100]–[102].

The homogeneous flow model, also known as three-equation or one-dimensional mixture flow model, assumes that the liquid and gaseous phases move through the system with the same flow velocity and temperature (assumes thermodynamic equilibrium between phases). Under this assumption, it is possible to describe the thermodynamic system by only three conservation equations (mass, momentum, and energy), and these three equations are sufficient to model the homogeneous two-phase mixture. The dynamic behaviour of the three characteristic fluid variables is described by three conservation equations of the mixture. For single-phase flow components (e.g. economiser, superheater, and steam turbine), the three characteristic fluid variables are the local pressure, the mass flux and the fluid temperature of the mixture or the subcooled water / superheated steam enthalpy. In case of two-phase flow components (e.g. evaporator and

condenser), the three variables are complemented by the void fraction [94]. The local pressure, the mass flux and the enthalpy is described by three conservation equations of the mixture.

The mass conservation is given as:

$$\frac{\partial \rho}{\partial t} + \frac{\partial(\rho * u)}{\partial z} = S \quad (3.1)$$

where, the source term (S) can contain additional mass flows into, or out from, the system.

The momentum conservation is expressed as:

$$\frac{\partial(\rho * u)}{\partial t} + \frac{\partial(\rho * u^2)}{\partial z} = -\frac{\partial p}{\partial z} + F_{gra} + F_{wall} + f(valve + form + pump) \quad (3.2)$$

The energy conservation is as follow:

$$\frac{\partial(\rho * h_0)}{\partial t} + \frac{\partial(\rho * u * h_0)}{\partial z} = \frac{\partial p}{\partial t} + q_{wall}, \quad (3.3)$$

where, ρ , u , and h_0 represent the density, the mixture velocity, the total enthalpy including the kinetic energy, respectively. And F_{gra} , F_{wall} and q_{wall} are the gravitational acceleration force, the friction force and the heat flow through walls, respectively, all per unit volume. The function, $f(valve + form + pump)$, considers the pressure losses due to valve, form frictions and the hydrostatic pressure differences of a pump.

The pressure derivative term appeared in the energy conservation equation due to using the total enthalpy in place of internal energy (U).

$$\frac{\partial U}{\partial t} = \frac{\partial h_0}{\partial t} - \frac{\partial p}{\partial t} \quad (3.4)$$

In thick-walled vessels, e.g. drum and feedwater tank, the lower part is just water and the upper part is only steam. Here, the composition of the liquid flowing out of the tank is determined by the water level and the height of the connected branch. Actually, the number of connected branches to the tank is unlimited. However, the height of the branch inlet has to be within the height range of the tank. When the water level is below the branch height, the flow consists of steam, while when the water level is above the branch height, it consists of water. In between, there is a transition area where the composition of the exiting liquid gradually changes from water to steam. In this transition area, the governing equations of the mixture flow model are the conservation equations of mass, momentum, and energy with the motion between the two phases using drift-flux correlations. In this model, the four characteristic fluid variables are local pressure, total mass flux, enthalpy, and void fraction. The continuity equation of the mixture is given by [103]:

$$\frac{\partial \rho_m}{\partial t} + \frac{\partial(\rho_m * u_m)}{\partial z} = S_m \quad (3.5)$$

where, ρ_m , u_m , and S_m are the density, the fluid velocity and the source term of the mixture, respectively.

The momentum equation of mixture, neglecting the effect of surface tension, can be expressed as:

$$\begin{aligned} & \frac{\partial(\rho_m * u_m)}{\partial t} + \frac{\partial(\rho_m * u_m^2)}{\partial z} + \frac{\partial}{\partial z} \left(\frac{\chi * \rho_{gas} * \rho_{liq}}{(1 - \chi) * \rho_m} V_{gas,j}^2 \right) \\ & = -\frac{\partial p}{\partial z} + F_{gra} + F_{wall} + f(valve + form + pump), \end{aligned} \quad (3.6)$$

where, χ , ρ_{gas} , ρ_{liq} , and $V_{gas,j}$ are the void fraction, the density of gas phase, the density of liquid phase and the drift velocity of the gas phase with respect to the volumetric centre of mixture, respectively.

The energy equation of mixture is written as:

$$\begin{aligned} & \frac{\partial(\rho_m * h_{0,m})}{\partial t} + \frac{\partial(\rho_m * u_m * h_{0,m})}{\partial z} + \frac{\partial}{\partial z} \left(\frac{\chi * \rho_{gas} * \rho_{liq}}{\rho_m} V_{gas,j} * (h_{0,gas} - h_{0,liq}) \right) \\ & = \frac{\partial p}{\partial z} + q_{wall}, \end{aligned} \quad (3.7)$$

The drift velocity of the gas phase with respect to the volumetric centre of mixture ($V_{gas,j}$) can be:

$$V_{gas,j} = \frac{j_{gas}}{\chi} - (j_{gas} - j_{liq}), \quad (3.8)$$

where, j_{gas} and j_{liq} are the superficial velocity of the gas and the liquid, respectively, which are artificial velocities determined by assuming that only a given phase is flowing in a certain cross-sectional area. It can be determined as follow:

$$j_k = \frac{\dot{V}_k}{A}, \quad (3.9)$$

where, the subscript k is either gas or liquid, \dot{V}_k is the volume flow rate of the phase k and A is the cross-sectional area. The drift velocity and the void fraction can be defined by means of the drift-flux correlation, which in turn yields the velocity of the gas phase (u_{gas}) and the liquid phase (u_{liq}) as follows:

$$u_{gas} = u_m + \frac{\rho_{liq}}{\rho_m} V_{gas,j}, \quad (3.10)$$

$$u_{liq} = u_m - \frac{\chi}{1 - \chi} * \frac{\rho_{gas}}{\rho_m} V_{gas,j}, \quad (3.11)$$

and the mixture density (ρ_m) is given by:

$$\rho_m = \chi * \rho_m + (1 - \chi) * \rho_{liq}. \quad (3.12)$$

This mixture flow model with drift-flux correlations is often used when the behavior of the total mixture rather than the individual constituent phases is required.

The dynamic model is generated based on the piping and instrumentation diagrams of the existing 135 MW ISCC power plant in Kuraymat, Egypt. All data of the construction geometry and the boundary conditions are from the plant. The reference plant includes three different circuits that are interconnected: the flue gases circuit, the HTF circuit, and the water-steam circuit. This structure, three different circuits, was mapped in APROS simulation to have a better view of the

process and control structures. Therefore, the dynamic simulation model includes three different nets namely: the gas turbine net, the solar field net, and the HRSG net, as shown in **Table 3.1**. Each net has its control structures and dynamic boundary conditions. The interfaces between the nets are the heat exchangers: the HRSG, and the HTF heat exchangers. On the one hand, the HRSG consists of a setup of heating modules, which extract the heat from the FG and evaporate the water in the water-steam circuit. On the other hand, the HTF heat exchangers act as the interface between the solar field and the water-steam circuit in the HRSG, by extracting the heat of the solar-heated HTF and transfer it to the water-steam circuit. The accurate functioning of these two interfaces is crucial to be able to achieve high-quality simulation results.

Table 3.1 Nets structure and functions of the ISCC model

Net's name	Description
Gas turbine simulation	Flue gas path, turbine sections and their control circuits
HRSG simulation	Circuit of water / steam side and their control circuits
Solar field simulation	Solar field HTF side and their control circuits
Dynamic boundary conditions	Boundary condition for the gas turbine, DNI and HRSG

The standard process components of APROS libraries are used for the modelling, pipe, heat exchanger, and turbomachinery. The homogeneous flow model is used to describe the process components of the FG path and the water circuit, provided that the liquid and gaseous phases move through the system at the same flow rate and temperature. The point or node component is a basic process component that has at least one inlet and one outlet flow and it is used to connect different kinds of process components. Between two connection points, the pipe component can be used to transport the working fluid and calculate the fluid flow, pressure drop and velocity. The specification of the pipe component includes the shape and dimensions of the pipes. The heat pipe comprises models for heat transfer between wall and fluid, heat storage into the tube and pressure loss of the flow and it is used as a representation of different components in a power plant like pipes, valves, and heat exchangers.

The process control system shall be capable of handling the dynamics of the HRSG and HTF heat exchangers system without restricting the performance. Therefore, the developed model was controlled by implementing the real control structures and electrical systems from the reference plant.

3.2.1 Gas Turbine Simulation

The gas turbine net simulates the compression of the air, the combustion, the subsequent expansion of the FG through the GT, and the heat transfer from the FG to the different heating modules of the HRSG, as shown in **Figure 3.1**. The FG mass flow rate is initialized from actual measurements as a boundary condition. The natural gas mass is controlled dynamically as these boundary conditions. The air flows into the compressor at ambient temperature and pressure and its mass flow rate is specified as a dynamic boundary condition and controlled by the speed of the compressor. The compressor speed is controlled by a Proportional–Integral (PI) controller defined in APROS, which receives the mass flow rate behind the compressor as a variable and the mass

flow rate from boundary conditions as a set point. The GT is defined under the assumption that the FG temperature, pressure, and mass flow rate match the actual measurements.

The FG from the GT, with a temperature of about 630 °C, is led through the inlet duct of the HRSG to the first heat transfer module (HP SH 5) and between the heating modules, intermediate ducts are installed, which allow entry between them. The last duct is the outlet duct, which connects the last heat transfer module to the stack, as shown in **Figure 3.1**.

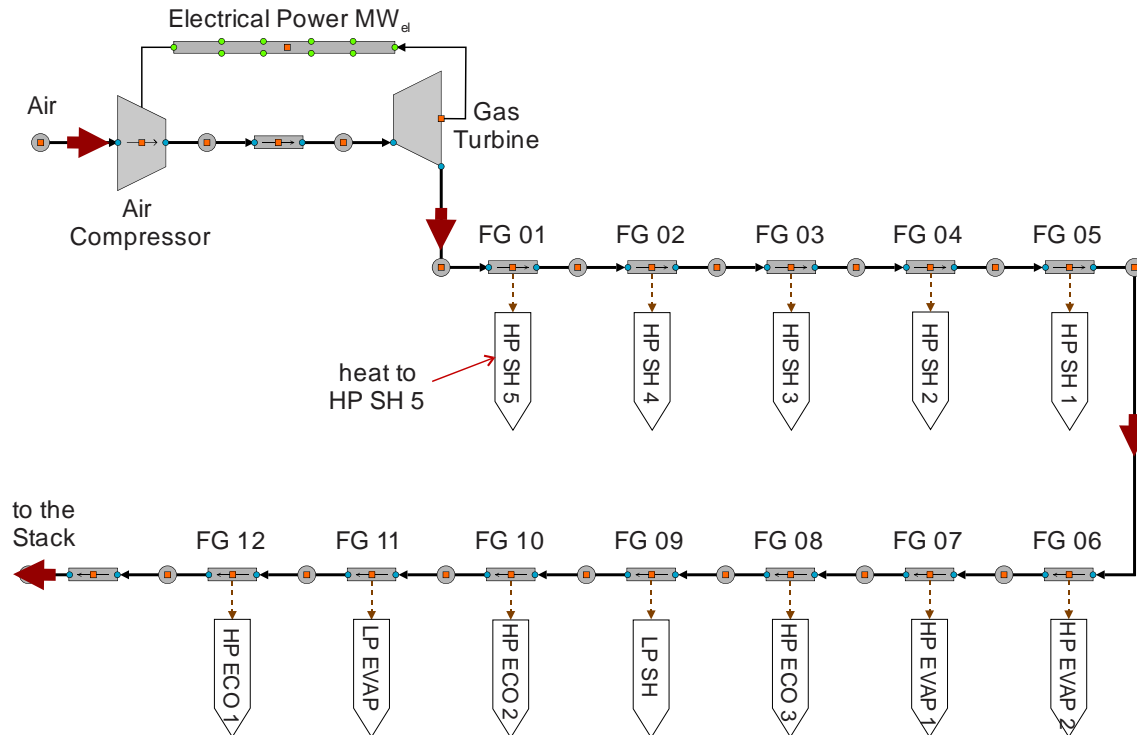


Figure 3.1 Schematic of the gas turbine net in APROS

3.2.2 HRSG Simulation

The HRSG net consists of a combination of heating modules, which extract the heat from the FG and evaporate the water in the water-steam circuit. The HRSG of the reference plant is a modular designed horizontal boiler with natural circulation. This means a horizontal FG direction with vertical tubes and natural circulation in the evaporators. As shown in **Figure 2.1**, the HRSG operates at two pressure levels. For each pressure level, water is supplied to the steam drum, via the economizers, by the HP feedwater pump (HP FWP). In the model, the condenser module is considered as dynamic boundary conditions.

The freshwater flows from the HP FWP into the first HP economizer (HP ECO 1) and is then divided into HP and low-pressure (LP) circuits. Before the HP ECO 2, a part of FW is extracted to pass through the LP evaporator (LP EVAP) and the LP SH, then to the LP ST. After the HP ECO 2 and before the HP ECO 3, a part of the FW is extracted to pass through the HTF heat exchangers during the day mode. The HP FW after the HP ECO 3 passes through the two HP evaporators (HP EVAP 1, and 2) and then mixed with the steam coming from the HTF heat exchangers to pass through the five HP superheaters (HP SH 1, 2, 3, 4, and 5). In order not to exceed the maximum steam temperature of 556 °C before the HP ST, HP FW is injected through two attemperators, one

attenuator between the HP SH 2 and the HP SH 3, and another attenuator between the HP SH 4 and the HP SH 5, as shown in **Figure 2.1** and **Figure 3.2**.

In the HP water-steam path, the HP FW is heated in the HP economizers (HP ECO 1, 2, and 3) to a temperature close to the saturation temperature) before it is fed to the HP drum. Then the water from the HP drum is fed to the evaporators (HP EVAP 1, and 2) through the downcomer and is partially evaporated, as shown in **Figure 2.1** and **Figure 3.2**. The driving force of the circulation is the difference of density between the water in the downcomer and the steam / water mixture in the EVAP tubes and risers, in so-called natural circulation. The saturated steam from the HP drum is fed to the HP superheaters (HP SH 1, 2, 3, 4, and 5) where it is superheated. Finally, the HP superheated steam, with pressure and temperature of about 70 bar and 566 °C respectively, is fed to the HP ST. The dimensions of the HRSG HP heating modules in the reference plant are given in **Table 3.2**.

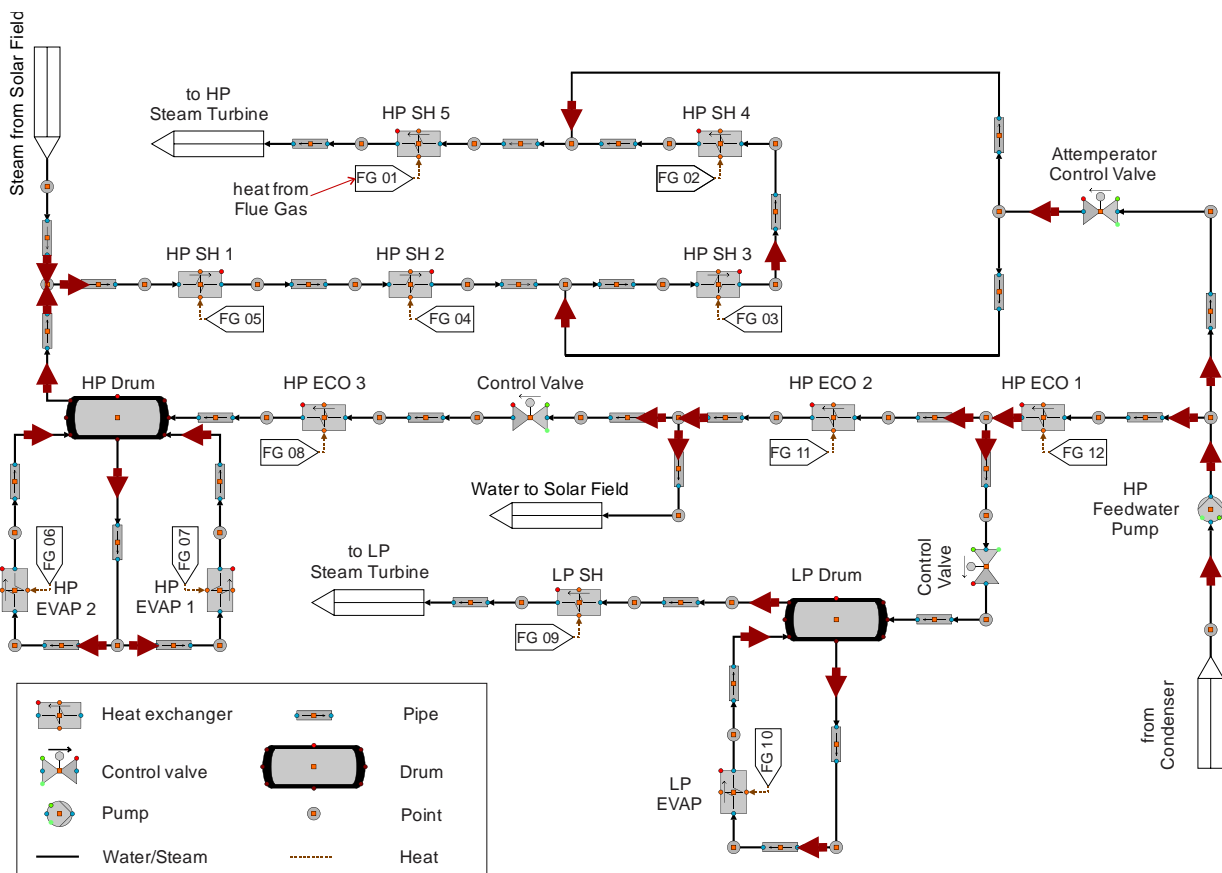


Figure 3.2 Schematic of the HRSG net in APROS

The HRSG net has three main controllers: one regulates the HP FW mass flow rate of the HP ECO 1, another regulates the water level and the pressure in the HP drum, and the third controls the injection cooling upstream of the HP SH 3 and 5 (attenuators). The inlet of the HP FWP is specified as boundary conditions with a pressure of 11 bar and a temperature of 110 °C. The total FW mass flow rate is regulated via the manipulation of the main FW control valve.

Table 3.2 Initialization of the HRSG high-pressure heating modules

	HP economizers			HP evaporators		HP superheaters				
	1	2	3	1	2	1	2	3	4	5
Module order	1	2	3	1	2	1	2	3	4	5
Number of parallel tubes in one row	41	41	41	41	41	41	41	41	41	41
Number of parallel rows	15	4	1	6	3	2	2	2	2	2
Outside diameter of the tube [mm]	38.1	38.1	31.8	38.1	44.5	44.5	44.5	44.5	44.5	44.5
Minimum tube thickness [mm]	3	3	2.6	2.6	2.6	3	2.9	3.2	3.6	3.6
Average tube length [m]	18.5	18.5	18.5	18.5	18.5	18.5	18.5	18.5	18.5	18.5
Outside diameter over fins [mm]	70.1	70.1	63.8	70.1	70.5	70.5	70.5	70.5	64.5	60.5
Thickness of the fins [mm]	1	1	1	1	1.3	1.3	1.3	1.3	1	1
Number of the fins [m ⁻¹]	280	255	120	280	280	280	280	280	250	120

3.2.2.1 The Level Control Mechanism of the HP Drum

The function of the drum level control is to adjust the level of the drum during the boiler start-up and to maintain its level at a constant steam load. A severe drop in this level can cause the boiler tubes to become exposed, causing them to overheat and become damaged. A rise in this level can disturb the process of separating moisture from the steam contained within the drum, reducing the efficiency of the boiler and allowing moisture to be introduced into the process or turbine.

The ECO water is fed to the drum through a FW distribution tube, which distributes the FW evenly over the length of the drum, below the water level (setpoint). From the drum, the water circulates through the EVAP employing natural circulation. In the EVAP, a part of the water evaporates and the water-steam mixture returns to the drum, where it is separated into water and steam. Saturated steam leaves the drum from the top to the superheating modules, where it is superheated and finally it flows to the ST. As mentioned above, the HRSG of the reference plant operates at two pressure levels [66], [67].

The control mechanism of the HP drum regulates the mass flow rate of water into the drum. The LP control structures are almost similar to those of the HP circuit. The control system includes PI controllers defined in APROS, which control the water level and the pressure in the HP drum. The parameter to be controlled is the mass flow rate through the control valve. The control system of the HP drum level is based on a three-element control, as shown in **Figure 3.3**, which makes the controller more robust. The operation algorithm of the controller is described as follows:

- The deviation between the actual drum level (L_{drum}) and the actual value (L_{setpoint}) is determined and taken as an input signal for the PI controller.

- The difference between the mass flow rate of the FW and the produced steam ($\Delta\dot{m}$) is calculated.
- The summation of the signals ($\Delta\dot{m}$, ΔL) is used as the second input signal for the PI-controller.

The PI controller regulates the FW mass flow rate into the drum through the continuous device control (DC) that regulates the FW mass flow rate from the FWP. As a basis for the control, the difference between the inlet and outlet mass flow rate of the drum and the change in the water level in the drum is measured and added. This sum defines the missing/excess water in the drum's circulation system and is initialized as input to the PI controller. The PI controller aims to make the sum of the differences approach zero.

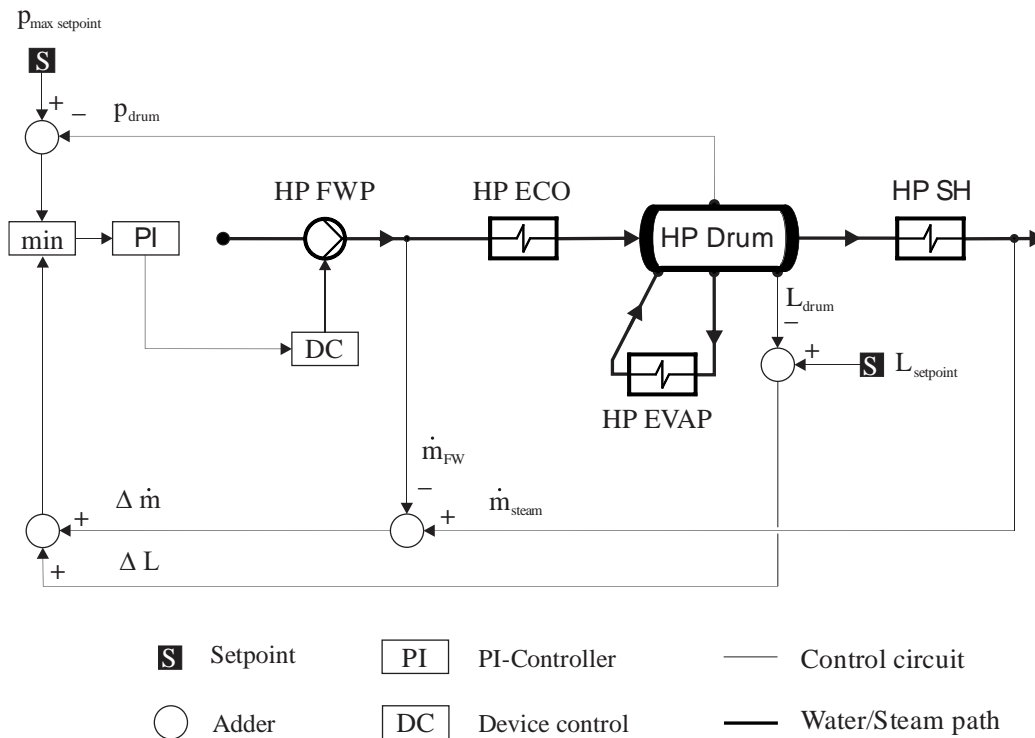


Figure 3.3 The HP drum level controller

The mass flow rate through the regulating valve is controlled by the output parameter of the PI controller (0 to 1). When the steam mass flow out of the drum increases and the water level in the drum decreases, the PI controller will increase the FW mass flow into the drum until the sum of the difference is zero. If the steam mass flow rate from the drum decreases and the water level in the drum increases, the PI controller reduces the FW mass flow rate into the drum until the sum of the difference is zero. In case the drum pressure exceeds a specific value ($P_{\max \text{ setpoint}}$), signal summation ($\Delta\dot{m}$, ΔL) is replaced by that resulting from the pressure difference between its pressure and its maximum pressure value, thereby preventing any further increase of its pressure. In order to avoid triggering the PI controllers with both signals at the same time, both output signals are filtered by a minimum filter defined in APROS. Both feedbacks (pressure and mass flow rate) controllers are connected to the minimum filter which selects both output signals and forwards the smaller value as input to the PI controller. This enables the PI controller to only be used for pressure regulation if the maximum permissible pressure is exceeded in the drum.

3.2.2.2 The Control Mechanism of the Attemperators

The attemperator is used to control the temperature of the superheated steam upstream of the ST by spraying water into the steam flow. The HRSG comprises two attemperators in the HP water-steam circuit to avoid the high-temperature difference in steam flow through the superheaters in the different operating modes (day / night mode). These two attemperators are located in front of two superheating modules, HP SH 3 and HP SH 5. The HP attemperators inject the FW mass flow rate at the inlet of the HP SH 3 and the HP SH 5, as shown in **Figure 3.2** to continuously provide a constant steam temperature at the inlet of the HP ST. High fluctuations or spikes in the superheated steam temperature should be prevented to preserve the HP ST material for longer life. The attemperator is designed to ensure that all water injected into the steam is evaporated to prevent the pitting of the turbine blades. The control mechanism of the attemperators regulates the superheated steam temperature at the outlet of the superheating section in order not to exceed the maximum permissible temperature of the HP ST (556 °C). The control system consists of a PI controller and control valve, defined in APROS. The input parameter of the PI controller is the measured temperature at the outlet of the last superheating module (HP SH 5). The temperature of steam at the outlet of the superheating section is measured and compared with the setpoint (in this case 566 °C). The value of the difference between these two signals is the input signal for the PI controller. The PI controller regulates the mass flow rate through the attemperator control valve.

In the LP water-steam path, water extracted from the HP ECO 1 is led through a throttle valve to the LP drum as shown in **Figure 3.2**. In the LP drum, the water circulates naturally through the LP EVAP via a downcomer and is heated until the saturation temperature is exceeded. Then, the produced steam leaves the LP drum into the LP SH. The LP drum has a level and pressure control mechanism that is similar to that of the HP drum (**Figure 3.3**). Finally, the LP superheated steam from the LP SH is combined with the steam from the HP ST and is fed into the LP ST. The actual dimensions of the HRSG LP heating modules were used for dimensioning the HRSG tubes in the model and are given in **Table 3.3**.

Table 3.3 Initialization of the HRSG low-pressure heating modules

	LP EVAP	LP SH
Number of parallel tubes in one row	41	41
Number of parallel rows	6	1
The outside diameter of the tube [mm]	38.1	31.8
Minimum tube thickness [mm]	2.6	2.6
Average tube length [m]	18.5	18.5
Outside diameter over fins [mm]	70.1	-
The thickness of the fins [mm]	1	-
Number of the fins [m ⁻¹]	280	-

3.2.3 Solar Field Simulation

The solar field comprises parallel rows of SKAL-ET 150 parabolic trough collectors forming 40 loops and each loop having four collector assemblies [81]. The mirrors cover 130,800 m² through 160 collectors and each collector has a total aperture area of 817.15 m², as in **Table 3.4**. The collectors are set up in a north-south direction and are rotated by a visual tracking system in an east-west direction to align the collector mirrors towards the sun depending on the angle of incidence. The solar field based on the HTF system delivers about 50 MW (thermal) at full load operating conditions. The HTF is heated in the receivers of the solar collectors and transfers its absorbed thermal energy through the HTF heat exchangers to the water-steam circuit. The HTF used in the solar field is a liquid phase HTF (Therminol VP1) [66], [67]. The HTF heat exchange system includes two similar parallel trains, each train consisting of an ECO and an EVAP in series. Both ECO and EVAP, are shell and tube type heat exchangers with water-steam on the shell side and HTF on the tube side, U tube type.

The heat absorption by the parabolic trough collectors is modelled in APROS through heat pipes in the solar field net, as shown in **Figure 3.4**. The effects of the solar field were mapped and a wide variety of influences (shading, activation, and deactivation) are modelled through the simulation. Each heat pipe simulates a parabolic trough solar collector, and every four heat pipes form a loop. Each loop inlet is connected to a cold header and the loop outlet is connected to a hot header. The solar field net includes 40 loops in total divided symmetrically in two solar fields, east and west fields. The DNI is dynamically initialized in each heat pipe via boundary conditions and heats the HTF flowing through. The heat gain by the absorber tubes from the DNI on the solar field (\dot{Q}_{HTF}), defined as solar heat input, was previously calculated in chapter 2. The HTF system is responsible for delivering the solar heat gained by the HTF (\dot{Q}_{HTF}) to the water through the HTF heat exchangers.

Table 3.4 The solar field design parameters [81],[65]

Solar field operation parameters	Unit	Value
Solar field total aperture area	m ²	130800
Number of collectors	N ^o	160
Number of collector loops	N ^o	40
Design direct normal irradiance (DNI)	W/m ²	700
Maximum solar field thermal power output	MJ/s	50
Hot leg HTF temperature	°C	393
Cold leg HTF temperature	°C	293

The solar field net includes the HTF heat exchangers that act as the interface between the solar field net and the HRSG net (water-steam circuit). The accurate functioning of these HTF heat exchangers is crucial to be able to achieve accurate simulation results. HTF heat exchangers are used to generate steam by cooling the HTF coming from the solar field, and this HP steam is fed back to the HRSG and is combined with the steam from the HP drum.

The main HTF pumps are variable speed pumps with a design mass flow rate of 250 kg/s that varies between 30 and 100% according to the actual solar irradiation. As a function of the mass flow rate, the pressure drop in the HTF cycle varies in a wide range between 1: 15 bar. The HTF pumped into the solar field is equally divided into two streams between the east and the west fields by control valves, as shown in **Figure 3.4**. The FW is supplied from a draw-off inside the ECO system of the HRSG. The FW is preheated in the HTF ECO up to just below saturation, before entering the HTF EVAP. In the HTF EVAP, steam is generated by cooling the HTF flow from the solar field as in the HTF ECO. The ECO and the EVAP are both shell-and-tube heat exchangers with two tube paths, type U-tube, as in **Table 3.5**. The steam coming from the HTF heat exchangers is combined with the steam coming from the HP drum and flows further into the HP SH 1, as depicted in **Figure 3.2**.

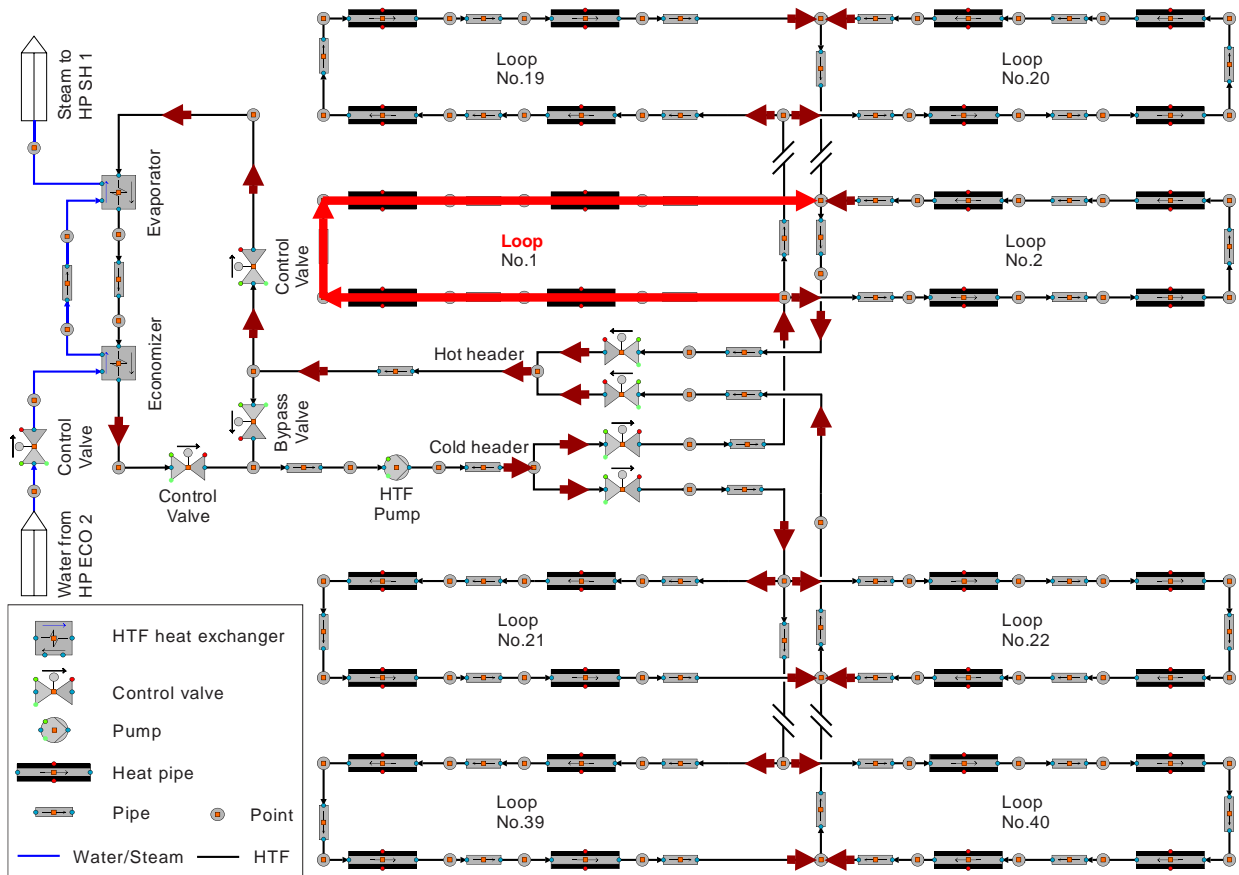


Figure 3.4 Schematic of the solar field net in APROS

The solar field net comprises three control systems that regulate the HTF mass flow rate into the solar field and the mass flow rate of the HTF and the water into the HTF heat exchangers. The first control system regulates the HTF mass flow rate through a PI controller defined in APROS to reach a constant outlet temperature (393 °C) from the solar collectors in order not to exceed the maximum allowable temperature of the HTF (400 °C). The second control system regulates the cooling mechanism of the HTF in the HTF heat exchangers through a bypass system to maintain the HTF inlet temperature to the solar collectors at 293 °C. In the night mode (no solar heat input), the HTF flows through a bypass control valve and circulates in the solar field to prevent the HTF from entering the HTF heat exchangers, this avoids undesired cooling of the HTF by the water in

the HTF heat exchangers waterside. The third control system regulates the FW mass flow rate in the HTF heat exchangers through a PI controller to reach the saturation temperature of the water at the outlet of the HTF heat exchangers.

Table 3.5 The specifications of the HTF heat exchangers

Parameters	Unit	Shell side	Tube side
Fluid	-	Water / Steam	Therminol VP-1
Nominal fluid flow rate	kg/s	28.50	173.25
Inlet temperature	°C	289	393
Outlet temperature	°C	292	293
Inlet pressure	bar	76.31	17.00
Nominal velocity	m/s	0.47	1.81
No. of passes per shell	-	1	2
No. of tubes	-	1110U	
Gross surface area	m ²	1034	
Effective shell/unit area	m ²	1006.37	
Mean temperature difference	°C	23.7	

3.2.3.1 The Control Mechanism of the HTF Mass Flow rate

The HTF mass flow rate into the solar field is divided equally between the east and west fields by two control valves. The HTF mass flow rate control system adapting the HTF pump speed to maintain the HTF outlet temperature from the solar field at 393 °C in order not to exceed the maximum allowable temperature of the Therminol VP1 (400 °C). The HTF mass flow rate control system includes a PI controller defined in APROS that controls the speed of the HTF pump depending on the heat rate absorbed by the HTF in the solar field (\dot{Q}_{HTF}).

The variable to be controlled is the HTF mass flow rate that is measured before the HTF pump. The required mass flow rate ($\dot{m}_{required}$) to be achieved is determined in a calculation cascade as follows:

- Calculating the specific enthalpy of the HTF at the solar field inlet (h_{in}) from the measured pressure (p_{in}) and temperature (T_{in}).
- Calculating the specific enthalpy of the HTF at the solar field outlet (h_{out}) from the measured pressure (p_{out}) and the set point temperature of 393 °C.
- Calculating the required HTF mass flow rate ($\dot{m}_{required}$) to reach the HTF temperature of 393 °C at the outlet of the solar field by dividing the heat rate gained from the solar field (\dot{Q}_{HTF}) by the specific enthalpy difference between the calculated specific enthalpies (h_{out} and h_{in}), as shown in **Figure 3.5**.

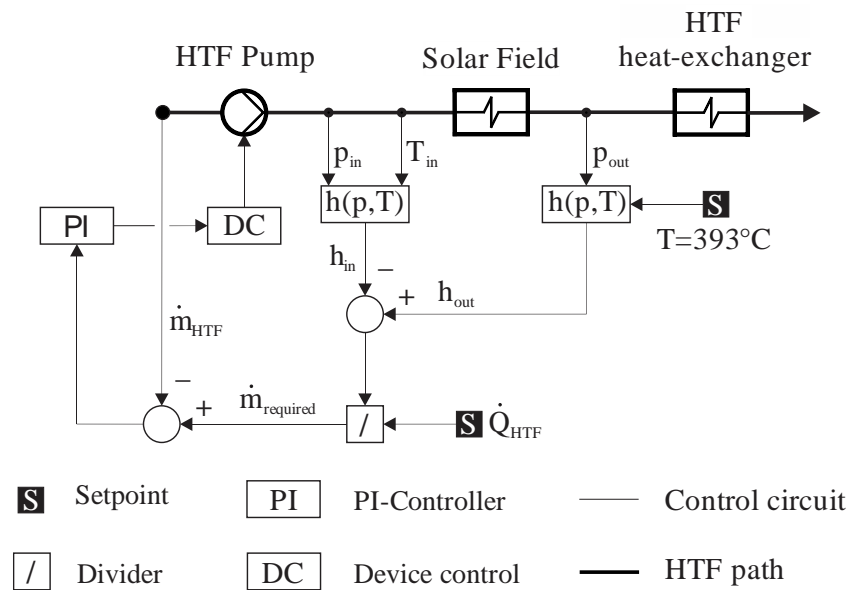


Figure 3.5 The HTF flow rate control circuit

The HTF mass flow rate ($\dot{m}_{required}$) is compared with the measured HTF mass flow rate before the HTF pump (\dot{m}_{HTF}). The difference between the two mass flow rates is initialized as a setpoint into the PI controller. Then the output parameter of the PI controller regulates the output of the HTF pump between 0 and 100% with a maximum mass flow rate of about 250 kg/s.

3.2.3.2 The Control Mechanism of the HTF Bypass

The HTF bypass mechanism regulates the temperature at the inlet of the solar field through a bypass system. The reference plant has a complex system to cool the HTF. In the model, the HTF cooling is achieved via two heat exchangers in series (ECO and EVAP) of counter flow type, as shown in **Figure 3.4**. The enthalpy difference of the HTF between the solar field inlet and outlet is transferred to the water-steam circuit via the HTF heat exchangers. The water coming from the HP ECO 2 is evaporated and slightly overheated in the HTF heat exchangers and then flows into the HP SH 1 with the steam from the HP drum, as shown in **Figure 3.2**. The HTF bypass system activates and deactivates the HTF mass flow rate into the heat exchangers and ensures a constant HTF outlet temperature from the heat exchangers at 293 °C. A PI controller, defined in APROS, measures the outlet temperature downstream of the HTF heat exchangers and controls the mass flow rate through the bypass valve thus the HTF inlet temperature to the solar field is constant (293 °C). If the outlet temperature drops below 293 °C, the PI controller bypasses the HTF heat exchanger by partially opening the bypass valve. Thus the HTF outlet temperature from the HTF heat exchangers is controlled to a constant 293 °C. When the temperature at the solar field inlet is above 293 °C, part of the mass flow rate is cooled in the heat exchangers via a control valve.

3.2.4 Dynamic Boundary Conditions

To initialize the created simulation environment with input data, interfaces for boundary conditions are created. In the dynamic model, boundary conditions were initialized for the GT, FW, and DNI parameters as a function of time. All boundary conditions were initialized as hourly values and timed by a common timer defined in APROS. A polyline module defined in APROS is used to

interpolate the initialized time values into a polynomial curve. To calculate different time series (different days), a switch defined in APROS can switch between different initialized polylines. In the gas turbine net, the boundary conditions for the natural gas and the combustion air were initialized. The natural gas temperature and pressure of 22.5 °C and 1 bar, respectively, were initialized as constant values as applied in the reference plant. The pressure and temperature of the combustion air correspond to the ambient conditions and are initialized in the node module upstream of the compressor. The FG mass flow rate was initialized in a PI controller to regulate the pressure and the mass flow rate of the compressor through its speed. In the HRSG net, the pressure and the temperature boundary conditions for the FW coming from the HP FWP were initialized in the node module before the HP ECO 1. Finally, the DNI was initialized in the solar field net according to the actual measurements. The DNI is initialized in the calculation network of the solar field. In a calculation cascade, receiver, piping, row shadow, incidence angle, end losses, and field efficiency are subtracted from the DNI. The resulting lossless DNI is multiplied by the collector area (130800 m²) and divided by the number of solar collectors (160). The resulting value is initialized into the heat pipes as the energy to be absorbed. The calculation system of the loss parameters can be found in the chapter 2.

3.3 Results and Discussion

The developed model was tuned using the operational design data of the reference plant. The boundary conditions of the gas turbine, feedwater and DNI are initialized with constant values. A comparison between this data and the simulation results was presented and evaluated. To increase the validity of the validation, the validation is carried out for two Cases. The simulated values for temperature, pressure and mass flow are measured and compared with the real data.

Then, to find out if the model can reproduce the dynamic behavior for temperature, pressure, mass flow rate, and power of the reference plant. Here, the dynamic model is validated using actual measurements for different four days in three different months, 20 Jul. 2013, 21 Jul. 2013, 30 Aug. 2013, and 04 Sep. 2013.

The main difference between the simulation days is the incoming DNI into the solar field and the resulting total electrical power outputs from the GT and the steam turbines in addition to the different ambient conditions. For the dynamic simulation, dynamic time series over 24h were available for each day. The dynamic simulation results for the heat absorbed from the given DNI values of different days were simulated then the mass flow rate, temperature, and pressure values along the power plant were presented and compared with the actual measurements.

3.3.1 Model Tuning

The steady-state simulation is just one initial condition for a dynamic simulation to tune the model. To increase the validity of the steady-state verification, it is performed for two different cases. As indicated in **Table 3.6**, the model was tuned using the operational design data for 50 MW solar heat input and two different ambient temperatures of 20 °C and 35 °C [16], [17].

The model was iteratively improved so that the numerical results match the operational design data of the two reference cases. The boundary conditions of the GT, the FW, and the DNI were initialized with constant values. The steady-state simulation results were calculated and compared

with design data and the accuracy of the main parameters results was evaluated and presented in **Table 3.7**.

As indicated in **Table 3.7**, the simulation results match the operational design data with high accuracy. Less accuracy appeared in the simulation pressure values (steam pressure after LP superheater and steam pressure in HP drum). The reason for these differences may be due to the geometry of the heat exchangers. Since the geometrical data is given in the model, further optimization of the pressure values is difficult.

Table 3.6 Reference steady-state cases description (operational design data)

Parameter	Case 1	Case 2
Ambient temperature [°C]	20	35
Natural gas flow rate [kg/s]	4.71	4.33
FG mass flow rate [kg/s]	206.36	190.47
FG temperature [°C]	605.29	622.94
Solar heat input [MW]	50	50
Net electrical power output [MW]	129.25	116.62
Net power plant efficiency [-]	60.93	59.77

After the model was tuned and verified, the simulation environment is initialized with the dynamic boundary conditions as will be explained in detail in the following sections.

Table 3.7 Comparison between the simulation results and the operational design data

Parameter/Variable	Case 1			Case 2		
	Reference	Simulation	Error	Reference	Simulation	Error
FW inlet temperature to the solar field [°C]	236.59	235.20	0.59%	232.86	231.49	0.59%
FW mass flow rate to the solar field [kg/s]	28.79	28.34	1.57%	28.48	27.89	2.09%
FW outlet temperature from the solar field [°C]	293.90	300.68	2.31%	292.56	299.17	2.26%
FG temperature [°C]	605.29	604.46	0.14%	622.94	604.46	2.97%
FW mass flow rate after FWP [kg/s]	56.80	56.81	0.01%	49.25	48.98	0.55%
FW pressure after FWP [bar]	150.40	149.99	0.27%	150.80	150.40	0.27%

Parameter/Variable	Case 1			Case 2		
	Reference	Simulation	Error	Reference	Simulation	Error
Steam pressure in LP drum [bar]	10.91	11.21	2.71%	10.82	10.77	0.48%
FW mass flow rate before LP drum [kg/s]	3.85	3.85	0.00%	3.30	3.39	2.72%
Steam pressure after LP SH [bar]	10.22	10.77	5.40%	10.22	10.41	1.89%
Steam temperature after LP SH [°C]	232.70	232.71	0.01%	235.40	232.98	1.03%
Steam pressure in HP drum [bar]	76.24	80.07	5.03%	74.57	78.28	4.97%
Steam mass flow rate before HP ST [kg/s]	46.78	46.52	0.55%	45.95	45.59	0.78%
Steam temperature before HP ST [°C]	559.70	560.01	0.06%	559.39	560.26	0.16%
Steam pressure before HP ST [bar]	69.38	67.81	2.26%	68.33	66.48	2.71%

3.3.2 Dynamic Model Validation

After the tuning of the model using operational design data for two different ambient temperatures, as indicated in **Table 3.7**, it is necessary to find out if the model can reproduce the dynamic behavior for temperature, pressure, mass flow rate, and power of the reference plant. Here, the dynamic model is validated using actual measurements for different four days in three different months, 20 Jul. 2013, 21 Jul. 2013, 30 Aug. 2013, and 04 Sep. 2013. The main difference between the simulation days is the incoming DNI into the solar field and the resulting total electrical power outputs from the GT and the steam turbines in addition to the different ambient conditions. For the dynamic simulation, dynamic time series over 24h were available for each day. The dynamic simulation results for the heat absorbed from the given DNI values of different days were simulated then the mass flow rate, temperature, and pressure values along the power plant were presented and compared with the actual measurements. Here, it should be mentioned that the model is not tuned during the dynamic simulation for the different given days.

Figure 3.6 shows the measured and simulated heat gain from the solar field for four selected days. The DNI is provided here for reference. The heat rate (\dot{Q}_{HTF}) shown in the figure is normalized on a per unit solar field aperture area basis, so the unit is [W/m²]. The DNI is the main factor determining the solar heat harvested by the HTF in the solar collectors (\dot{Q}_{HTF}). The calculation point of the HTF heat absorption rate (\dot{Q}_{HTF}) simulation results in **Figure 3.6** located at the outlet of the solar field, directly before HTF heat exchangers. The simulation results show agreement with measured data, this behavior is mainly achieved by the control system defined in the model.

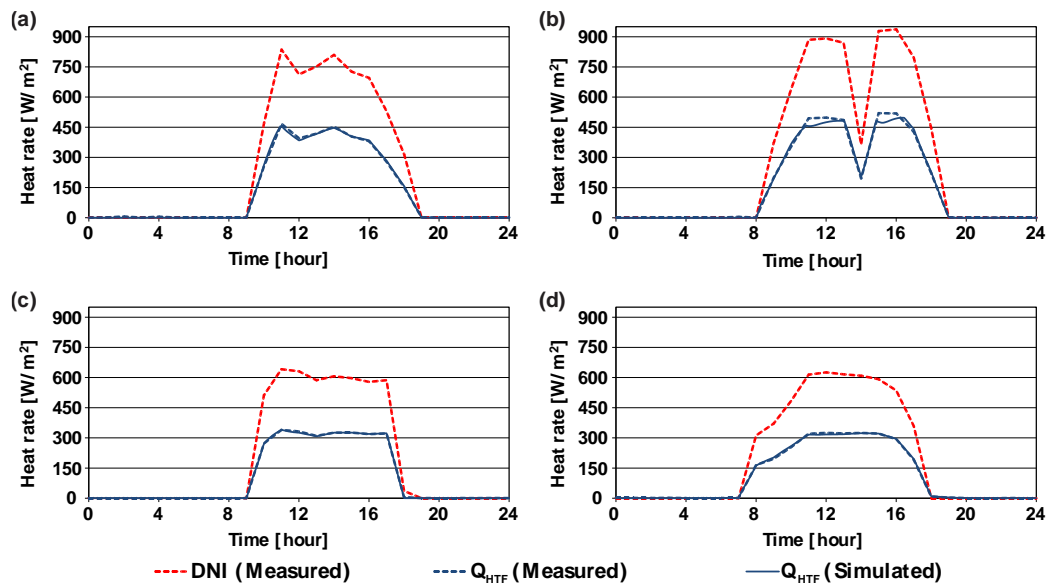


Figure 3.6 The rates of heat absorption from the solar field for four days: (a) 20.07.2013, (b) 21.07.2013, (c) 30.08.2013, (d) 04.09.2013

In the HRSG net, the simulation of the HP and LP water-steam circuits and the simulation of the steam coming from the HTF heat exchangers are of particular importance. Besides, it is necessary to check whether the simulation can good approximate the mass flow rate of the FW in both circuits, HP and LP circuits. **Figure 3.7** reveals the simulated and the measured FW mass flow rate in the HP and LP circuits for the different four days.

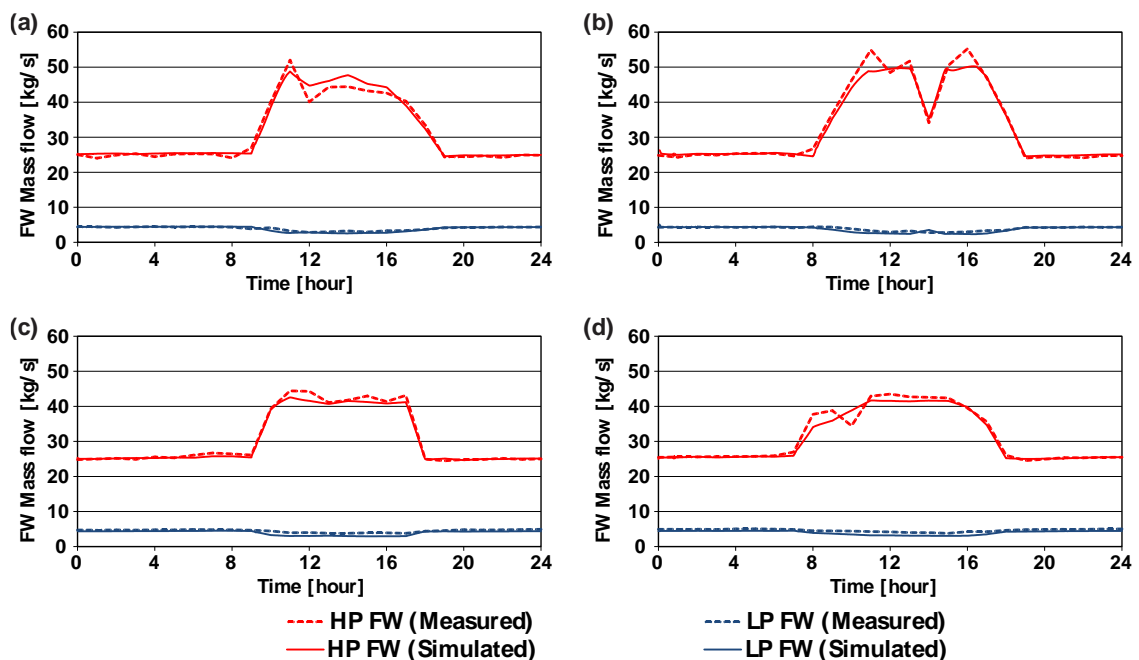


Figure 3.7 The feedwater mass flow rate for four days: (a) 20.07.2013, (b) 21.07.2013, (c) 30.08.2013, (d) 04.09.2013

In **Figure 3.7**, the FW mass flow rate in the HP circuit increases during the day as a result of the availability of the solar field in the power plant, contrary to the FW mass flow rate in the LP circuit, which decreases slightly during the day. **Figure 3.7** indicated that the simulation results of the FW

mass flow rate for both, the HP and the LP circuit, match well the actual measurements for the different four days. During the day mode, the additional FW mass flow rate in the HP circuit is well represented. The results showed that the FW flow in the LP circuit decreased during the daytime mode, which could be due to the decrease of available heat in the FG due to the higher mass flow rate in the HP circuit, and this slight decrease was also well represented with the simulation results. The fluctuations of the mass flow rate are modelled, but its extreme rates of change cannot be modelled accurately, however, a good trend is observed. The measuring point of the HP and LP FW mass flow rate is located upstream of the HP ECO 2 and upstream of the LP drum, respectively.

Figure 3.8 shows the simulated and the measured steam mass flow rate after the HP SH 5 and the LP SH. Similar to the FW mass flow rate, the steam mass flow rate in the HP circuit also increases during the day, contrary to the steam mass flow rate in the LP circuit, which slightly decreases during the day.

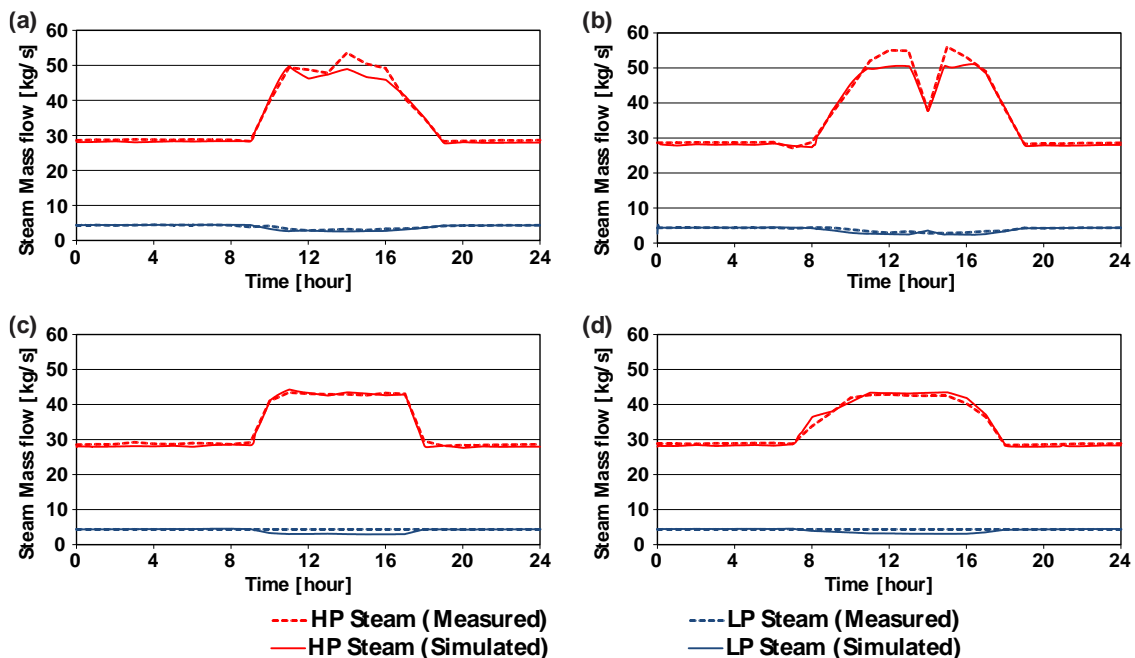


Figure 3.8 The steam mass flow rate for four days: (a) 20.07.2013, (b) 21.07.2013, (c) 30.08.2013, (d) 04.09.2013

Figure 3.8 revealed that the simulation model can accurately represent the trend of steam mass flow rate change after the HP SH 5 and the LP SH. Again, the increased mass flow rate in the HP circuit and its decrease in the LP circuit during the day can be modelled well, but the representation of the extreme values cannot be modelled identically, however, a good tendency can be seen.

Figure 3.9 shows the simulated and the measured steam pressure before the HP and LP steam turbines. The actual measurements show that the pressure of the steam after the HP superheating modules significantly increases during the day. The simulation results are slightly higher than the actual measurements, especially at the extreme values, however, the model can simulate the steam pressure variation during the load change well.

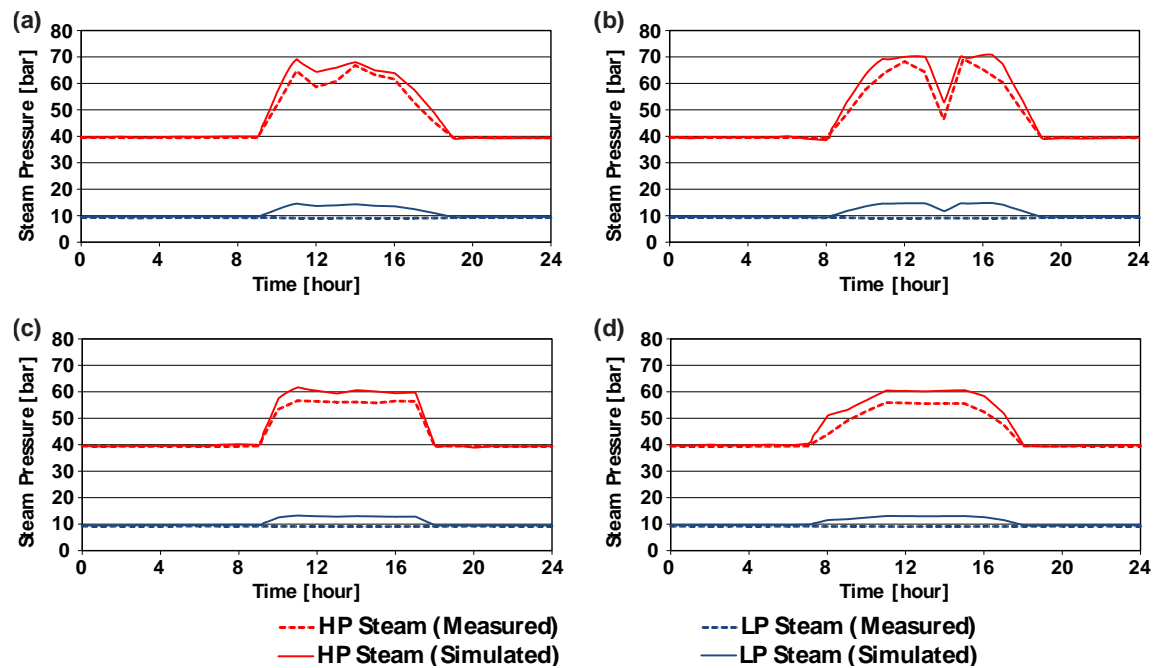


Figure 3.9 The steam pressure before the steam turbines for four days: (a) 20.07.2013, (b) 21.07.2013, (c) 30.08.2013, (d) 04.09.2013

In contrast to the actual measured data of the LP steam, constant pressure is observed in the simulation results which can be attributed to the measurement point and the role of the pressure control mechanism of the LP drum (**Figure 3.3**). The measuring point prevented the effect of the solar field-induced pressure change through a control valve upstream of the ST. It is possible to reproduce the effect of the solar field-induced pressure change by moving the measuring point between the control valve and the ST.

Figure 3.10 shows the simulated and the measured temperature behavior of the superheated steam after the HP SH 5 and LP SH. The effect of the solar field can be seen here in the temperature values of the LP steam. The steam temperature in the LP circuit increases during the day that may be due to the decrease of the LP mass flow rate during the day.

The results show that the temperature behavior of the actual measurements can be reproduced by the model. In **Figure 3.10** (a) and (b), the actual measurements of the days 20.07.2013 and 21.07.2013 show that the temperature of the HP steam before the ST decreased during the day however the model reproduced the temperature value with a constant value that is due to the control mechanism of the constant steam temperature before the ST through the attemperators. It is not recommended to change the steam temperature before the steam turbines, as this may cause material problems in the blades of the ST. The simulation results reveal the role of the attemperators in controlling the steam output temperature from the superheating modules, HP SH 5 and LP SH, in the dynamic model.

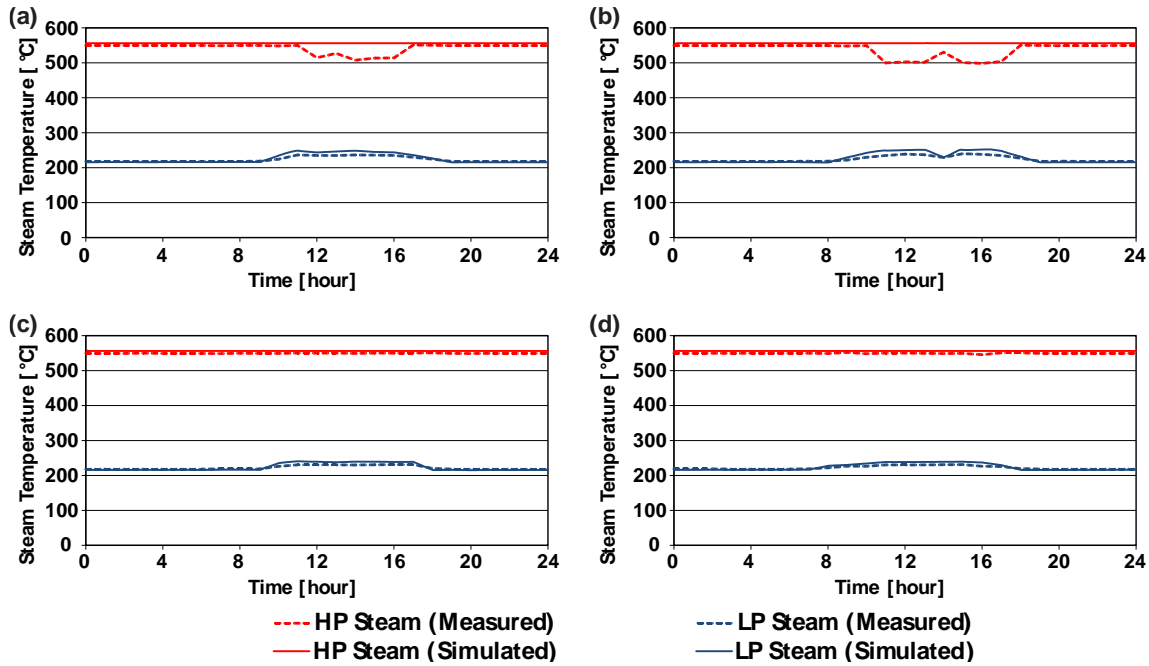


Figure 3.10 The steam temperature before the steam turbines for four days: (a) 20.07.2013, (b) 21.07.2013, (c) 30.08.2013, (d) 04.09.2013

The last important parameter to be validated is whether the overall performance of the ISCC systems can be simulated was the electrical power output of the ISCC power plant. **Figure 3.11** shows the simulated and the measured electrical power output from the steam turbines and the whole ISCC power plant.

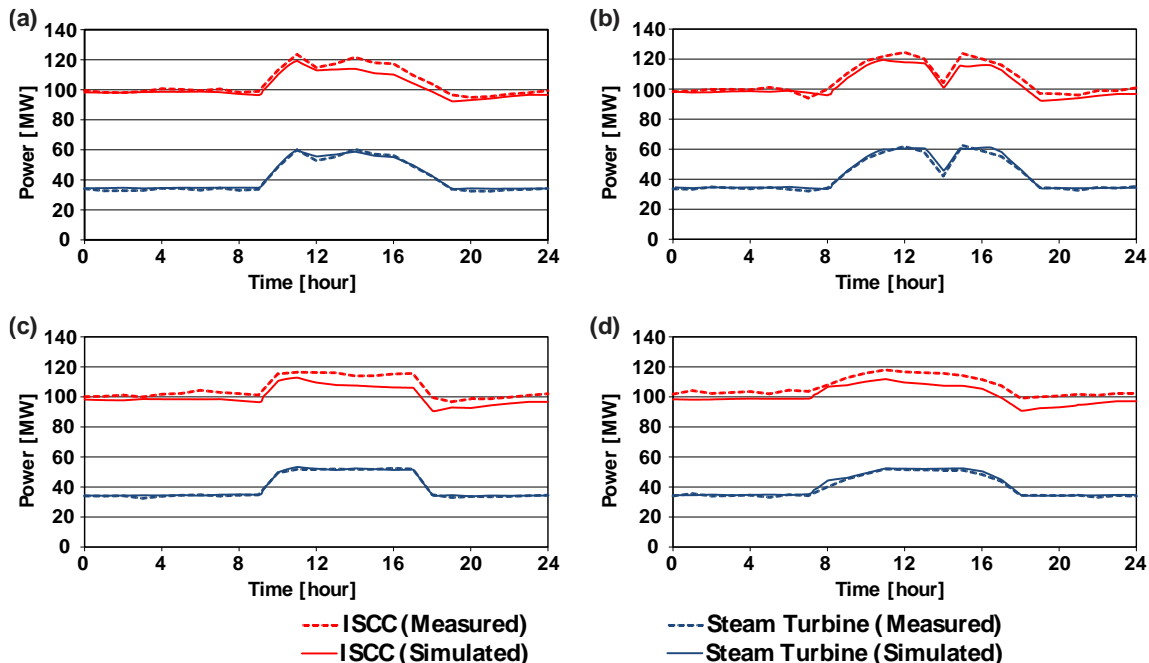


Figure 3.11 The electrical power output of the ISCC power plant for four days: (a) 20.07.2013, (b) 21.07.2013, (c) 30.08.2013, (d) 04.09.2013

Unlike the stand-alone solar power plant, the ISCC power plant produces electrical power for the grid regardless of solar radiation conditions, as revealed in **Figure 3.11**. During the day, the electrical output of the ISCC power plant is increased as a result of the heat harvested in the solar

field. It can be concluded that the curve of the measured electric power output can be simulated well through the dynamic model.

During the day, the simulation results represent the actual measurements of the steam turbines electric power output with high accuracy. There are small deviations in the simulation results for the electric power output of the whole ISCC power plant that is due to the deviation in the simulation results for the electric power output of the GT.

Chapter 4: Experimental Investigation of Dynamic Instabilities in HRSG

In this chapter, the fundamentals of the two-phase flow are briefly explained and the mechanisms of three main types of the two-phase flow dynamic instabilities in water tube boiling are described in detail using simple models. Then, the design of the test rig using similarity-based scaling criteria was mentioned. Finally, the experimental results for the two-phase flow dynamic instabilities were provided and discussed.

4.1 Introduction

Since the gas turbine is an inherently flexible component, studies in the literature were largely focused on the dynamic response of the water / steam bottoming cycle. In HRSGs, demineralised water is vaporized using the hot exhaust gases from the upstream gas turbine, thus driving the steam turbine. There are two different concepts for HRSGs. On the one hand, there is the vertical HRSG with horizontal tubes, and on the other hand the horizontal HRSG with vertical tubes. Depending on the construction and the working principle of the HRSG, there are more or less prone to so-called flow instabilities. And concerning climate protection, it is a significant task to develop evaporation processes in the HRSGs, because this can increase the efficiency of the power plants and thus reduce CO₂ emissions. It is important to understand occurring instabilities to prevent unstable and unsafe operating conditions during the evaporation process to increase the service life of the HRSGs. In order to achieve a better understanding of this evaporation process, research is being conducted in the areas of heat transfer, pressure drops, and instability phenomena in two-phase (water-steam) flow.

Two-phase flow systems are widely used in many industrial systems, such as steam generators, thermal management, refrigeration and cryogenics, and chemical processing systems. It has been studied over several decades due to its application in a wide variety of areas such as the chemical industry, food industry, power plants, refrigeration, and in recent years, heat removal from high heat flux devices such as computer chips and fuel cells. Two-phase heat transfer also has an application in space-based systems that involve refrigeration or thermal control systems. Besides the above-mentioned fields, two-phase heat transfer finds an application in other traditional means of heat transfer such as heat exchangers, petro-chemical processing, condensers and evaporators.

Heat recovery steam generator behavior is of particular importance to the water vapor flow in the heat exchanger tubes. Therefore, the two-phase flow and the phenomena associated with it are described. To design the evaporation process, it is important to understand occurring instabilities to prevent unstable and unsafe operating conditions.

Flow instabilities due to mass flow rate or pressure disturbances lead to mechanical as well as thermal fatigue [104]. These instabilities can cause serious damage or impairment during operation. In the case of mechanical fatigue, vibrations are induced in the HRSG as well as in its components due to mass flow rate and / or pressure oscillations. Furthermore, swinging wall temperatures can develop thermal stresses within the tube. Flow instabilities can lead to a periodic

change of the flow forms with different heat transfer mechanisms, which can lead to different wall overheating in the tube. Inadequate cooling of the tube wall leads to thermal failure, which usually manifests itself in the form of burnout of the wall. Thus, due to oscillations of several parameters, no stable process takes place. On the one hand, these flow instabilities lead to a reduction in the overall efficiency and on the other hand, they lead to many undesirable side effects, e.g. tube vibration. In particular, a reliable prediction of possible flow instabilities is important to avoid insufficient cooling of the steam generator tubes due to insufficient water circulation. Thus, reliable dimensioning and design of equipment in which these flows occur is a very important challenge.

In the two-phase flow systems, several different instabilities may occur. While the static instabilities are part of the standard boiler design and analytically accessible, a great effort is to be introduced by researchers to understand the dynamic instabilities. Unlike static instabilities, which contain a one-time excursion from an unstable operating point to a new stable condition, the dynamic instabilities are labelled by continuous cycling between slightly unstable operating points. These dynamic instabilities are hereunder briefly explained. In general, the dynamic instabilities in heat exchanger tubes can be classified as Density-wave type oscillations (DWO), Pressure-drop type oscillations (PDO), and Thermal type oscillations.

The dynamic instabilities analyses for vertical HRSG are of significant importance. As shown in the literature, there is no experimental study regarding the instabilities analyses for vertical HRSG. Furthermore, it can be seen that little research in the field of two-phase flows deals with demineralized water as a test fluid. Previous experimental studies in this research area mainly used refrigerants such as Freon-11, because of their low boiling point. In contrast, a test rig is designed and operated with demineralized water as a test fluid to avoid potential side effects due to different fluid properties. Another point by which the test rig differs from previous ones is the variability in parameters concerning startup processes, the orientation of the evaporator tube and the multiplicity of operating options.

4.2 Technical Fundamentals

To understand the properties and conditions in a two-phase flow, it is first of all important to deal with the different flow or phase distribution states of a two-phase flow. The water and steam phases can differently be distributed in a tube with the independence of velocity, volume fraction and tube orientation (horizontal, vertical or inclined). The various distributions of water and steam phases in a tube are known as flow patterns. Depending on the volume fraction of the steam and the orientation of the tube, different flow forms occur [105]. In the horizontal heated pipe, the water enters the heated pipe as sub-cooled water and leaves as superheated steam. Between the inlet and outlet of the heated pipe, mixed and transitional forms occur as shown in **Figure 4.1**.

A. Temraz et al. [106] have observed and recorded the existing flow pattern for the water on the sight glass at the outlet of the evaporator tube under the forced circulation operating condition by a high-resolution camera as shown in **Figure 4.2**. These captures were taken at the outlet of the evaporator for the water to enter the evaporator tube with constant inlet pressure (p_{in}) and constant inlet temperature (T_{in}) equal to 4 bar and 92 °C, respectively, with a uniform heating power of 6000 W and various mass flow rates.

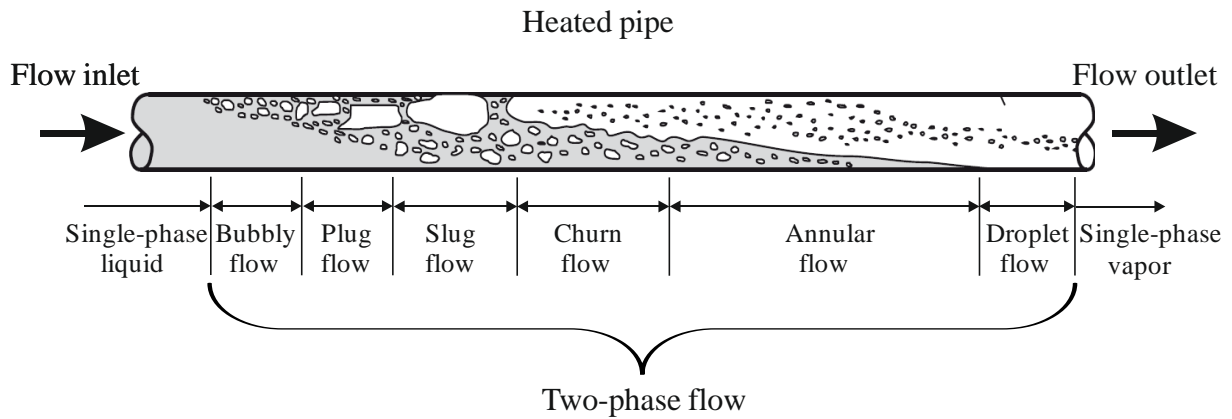


Figure 4.1 Flow patterns in the horizontal heated pipe [105]

The pressure and temperature values listed under each capture in **Figure 4.2** represent the conditions of water leaving the evaporator tube. The flow pattern appeared in **Figure 4.2 (a)** to be bubbly flow at the mass flow rate ($\dot{m} = 85$ kg/h) and transformed to plug flow in **Figure 4.2 (b)** at mass flow rate ($\dot{m} = 75$ kg/h). During decreasing the mass flow rate from ($\dot{m} = 65$ kg/h) to ($\dot{m} = 15$ kg/h) at the same inlet and heating conditions, the flow pattern converted from churn flow as shown in **Figure 4.2 (c and d)** to annular flow as shown in **Figure 4.2 (e, f, g and h)**.

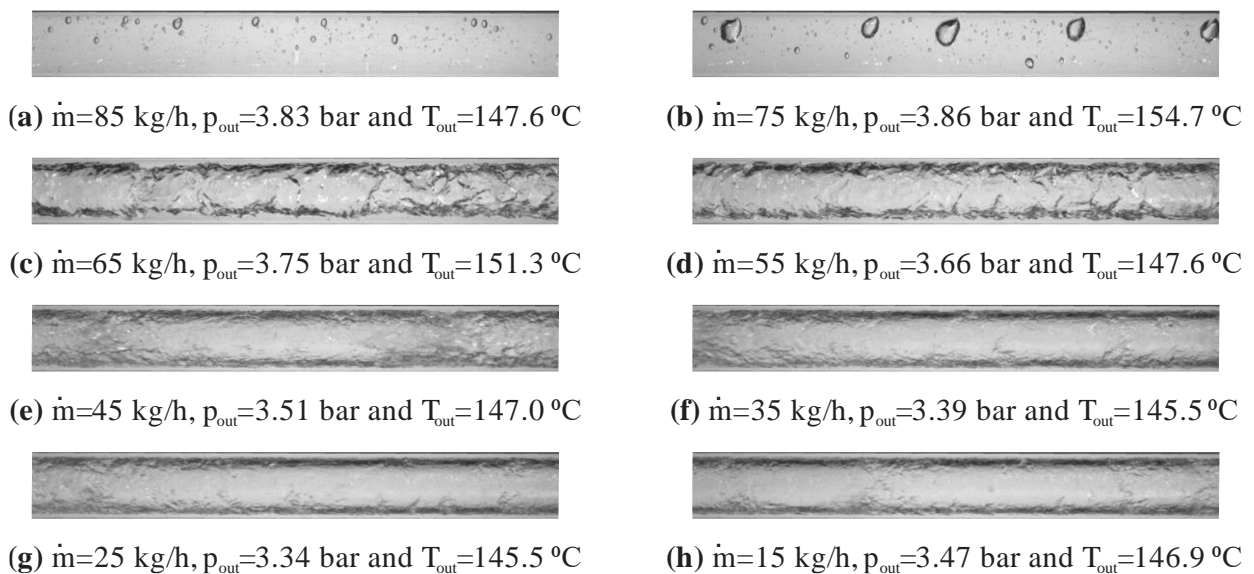


Figure 4.2 Flow pattern for water leaving the evaporator tube with various mass flow rates [106]

Flow maps are generally applied to predict the local flow pattern in a pipe. In these maps, the existence range of the flow regime is represented in two dimensions. It displays the transition boundary between the flow regimes, generally plotted on a log-log graph. These flow maps can only give a rough guide on the flow regimes in the heated pipe because there are no clear boundaries between the individual flow forms. In the literature, several flow maps are available, where the comparison between them is very difficult. Many of these maps are developed for an adiabatic water-steam flow and thus are only suitable for heated pipe under additional assumptions. Simple maps use one axis to differ between the flow regimes, while complex maps are built based on different axes. **Figure 4.3** shows a complex flow map for the horizontal and inclined heated

pipe is developed by [107]. It is one of the most widely used flow maps for predicting the transient between two-phase flow regimes in a horizontal heated pipe.

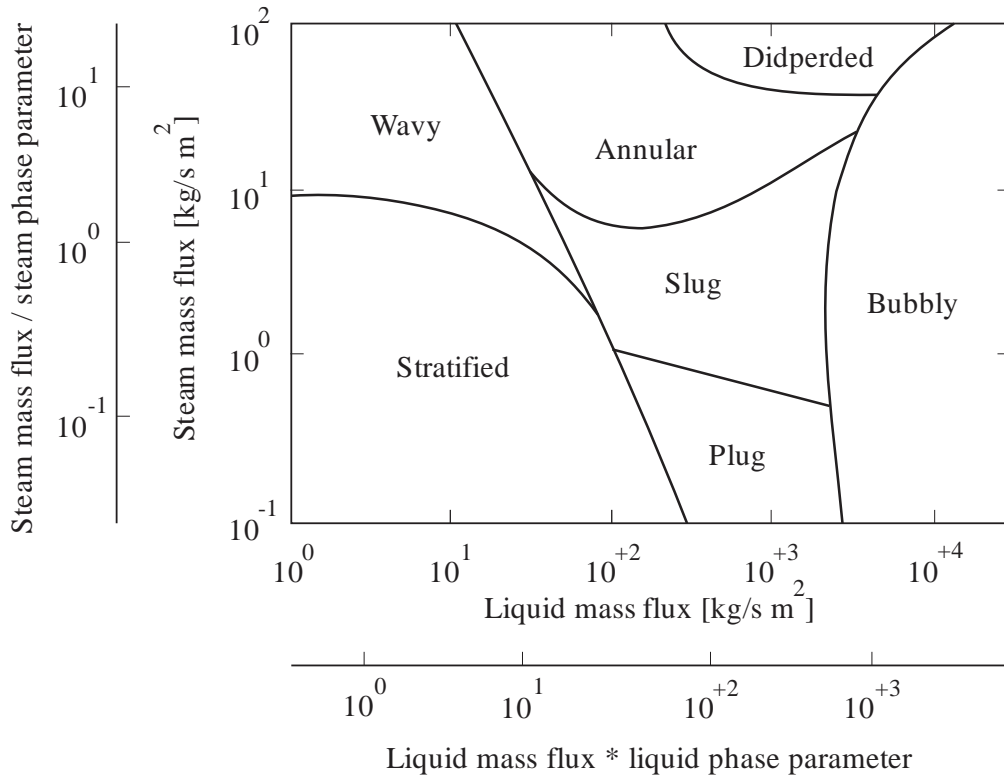


Figure 4.3 Flow map for the horizontal heated pipe by [107]

The intersection of mass velocities of the water and the steam on Taitel’s map identifies the flow pattern that exists at these conditions, as shown in **Figure 4.3**. Although the flow maps can only give a rough guide on the flow regimes, they are of significance for predicting the flow regime inside the heated pipe.

4.3 Dynamic Instabilities Mechanisms

The two-phase flow instabilities can be classified as static and dynamic [104]. The static instabilities were well defined and understood by a lot of studies and research and they are a part of the standard boiler design. Here, the mechanisms of dynamic instabilities are explained using simple models.

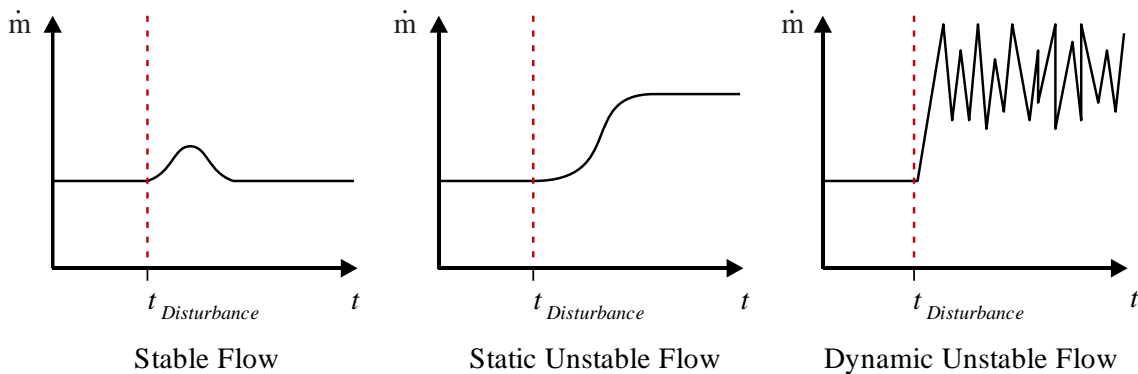


Figure 4.4 Static vs. dynamic instabilities

Static Instabilities are commonly characterized as a one-time departure from one unstable operating condition to a new, distinctly different operating condition, such as boiling crisis, Ledinegg instability, and flow pattern transition instability.

Unlike static instabilities which involve leaving one unstable operating condition to a new stable one, the dynamic instabilities lead to periodic fluctuations around a semi-fixed operating point due to a feedback mechanism between competing impacts on the flow [108]. In the case of dynamic instability, the flow parameters have sufficient interaction and delayed feedback between each other. The dynamic instabilities can result from the multiple feedbacks between mass flow rate, pressure-drop and density change variation in a boiling tube. The compressibility of the two-phase mixture provides the main motor of dynamic instabilities formation. The main types of two-phase flow dynamic instabilities in evaporator tubes are DWOs, PDOs and thermal oscillations. All of the dynamic instabilities present in the flow boiling only.

4.3.1 Density Wave Oscillations

Unlike Ledinegg instability (static instabilities), where the problem may be avoided by modifying the system to eliminate the negative slope portion of the internal characteristic curve, Knowledge of Operating Boundaries is the only option available for DWOs. Further, there are no simple correlations available for DWO stability boundaries as DWOs appear only for specific combinations of operating conditions dependent on a wider variety of factors [136].

The DWO is one of the most important dynamic instabilities, which take place in evaporator systems. Here, the fluid properties oscillate with relatively high frequencies. A simple model is adopted to understand the mechanism of DWOs. The model consists of a supply tank, an evaporator (investigated tube) and two flow restrictions [109]. The mechanism of DWOs is explained with the aid of **Figure 4.5**. In this model, it is assumed that the pressure in the supply tank (p_1) and the outlet pressure of the evaporator (p_e) are kept constant. Furthermore, the steam generation is assumed to be constant in the test tube independent of mass flow rate. This means that the heater should maintain a constant steam production in case of mass flow rate variation.

As previously mentioned, mass flow rate or pressure disturbances can lead to two-phase flow instabilities. There are two key pressure characteristic curves are used in the analysis of the stability for the flow boiling systems. The curve of the demand pressure-drop versus the mass flow rate, which called the internal pressure characteristic curve and the curve of supply pressure-drop versus the mass flow rate, which called the external pressure characteristic curve. The intersection between these two curves determines the stability of a given operating point.

Suppose that the operation is on the positive slope portion of the internal characteristic curve (point 1). At a time ($t = t_0$), if the pressure drop in the evaporator undergoes a sudden minor reduction from its nominal value with $\Delta p = p_0 - p_e$ then a drop in the inlet pressure (p_0) will occur instantaneously since the exit pressure (p_e) is constant. As a consequence, the mass flow rate in the evaporator and thus the inlet velocity (u_{in}) increases according to the following equation:

$$u_{in} \propto \sqrt{p_1 - p_0} \quad (4.1)$$

As a result, a higher density fluid will flow at ($t = t_0$) from the supply tank into the evaporator. However, an increase in the inlet velocity from point 1 to point 2 will cause an increase in the internal pressure drop, as shown in the internal characteristic curve in **Figure 4.5**.

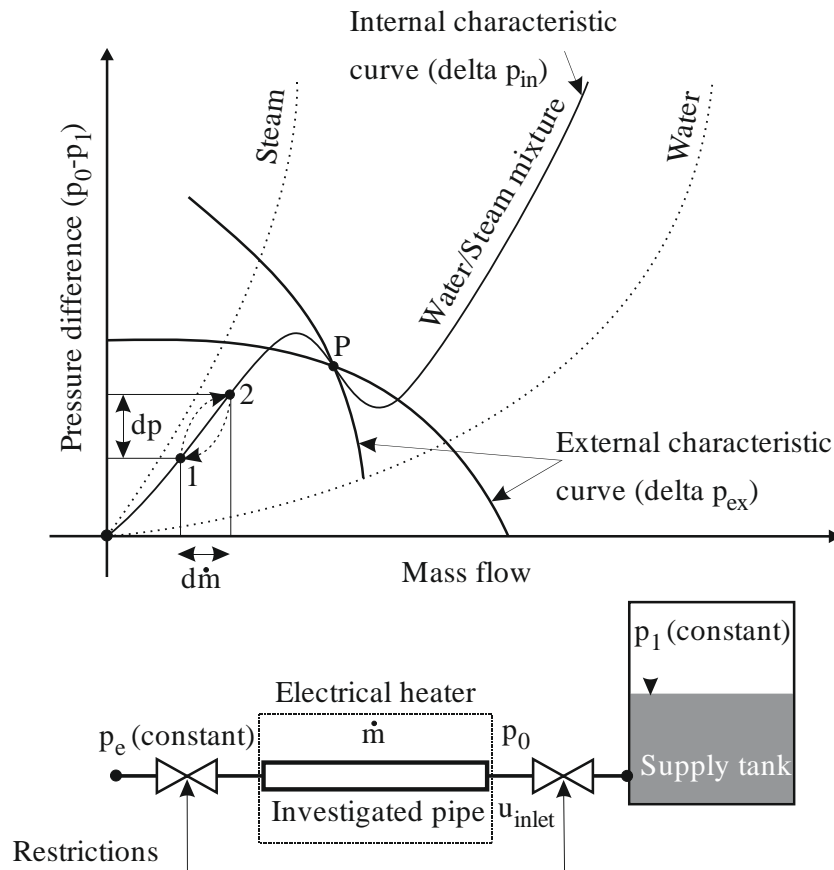


Figure 4.5 Density wave oscillations [106]

After the residence time, the time interval which is taken by a particle to cross from the inlet to the outlet of the evaporator, the increased internal pressure drop causes the inlet pressure (p_0) to increase since the exit pressure (p_e) is constant. According to the above equation, an increase in the inlet pressure (p_0) leads to a decrease in pressure drop ($p_1 - p_0$) and thus to a reduction in the inlet velocity (u_{in}); since (p_1) is constant. A reduction in the inlet velocity will result in mass flow rate reduction, from point 2 to point 1; as shown in the internal characteristic curve in **Figure 4.5**. As results, a less mass flow rate will enter the evaporator and thus the fluid has greater enthalpy as well as lower density when it reaches the outlet restriction. A lower inlet velocity causes a lesser pressure drop in the test tube ($p_0 - p_e$) and this starts the cycle again and so on which causes density oscillations in the evaporator tubes.

4.3.2 Pressure Drop Oscillations

The PDO can occur when the evaporator system has a compressible volume like a drum. Here, the fluid properties oscillate with lower frequencies compared to DWO. The same model is employed to understand the mechanism of PDOs but after adding a surge tank (as compressible volume) [109] as shown in **Figure 4.6**. The surge tank is located upstream of the evaporator (investigated tube). In this model, it is assumed that the pressure in the supply tank (p_1) and the pressure at the outlet of the evaporator (p_e) are constant and the steam generation is

constant in the test tube independent of mass flow rate, i.e. the heater should maintain a constant steam generation in case of mass flow rate variation.

The mechanism of PDOs can be explained using **Figure 4.6**. Suppose that at a time ($t = t_0$), the operation is on the negative slope portion of the internal characteristic curve (point A). The slight decrease in the surge tank pressure triggers the mass flow rate to enter the surge tank more than leaves it, note that p_1 and p_e are constant. Due to the accumulation of fluid in the surge tank, the pressure of the surge tank (p_2) will increase. As a sequence of this, the equilibrium point moves up until it reaches the peak (point B). Here, any higher pressure can only be obtained by a higher mass flow rate as given by the internal characteristic curve (point C). At point C, the amount of mass flow rate that leaves the surge tank (\dot{m}_2) is more than the amount of mass flow rate that enters the surge tank (\dot{m}_1). Due to the mass flow rate imbalance, the level in the surge tank will be decreased. This means that the surge tank pressure (p_2) will also reduce till reaches the operating point D. At point D (the lowest point of the internal characteristic curve), lower pressure can only be sustained if the mass flow rate decreases again to operation point A. At point A, the mass flow rate leaving the surge tank (\dot{m}_2) is less than the mass flow rate that enters it (\dot{m}_1). Hence, the pressure inside the surge tank (p_2) increases and causes a shift to operating point B. This starts cycling (ABCD) again and so on which causes pressure oscillations in the evaporator tubes.

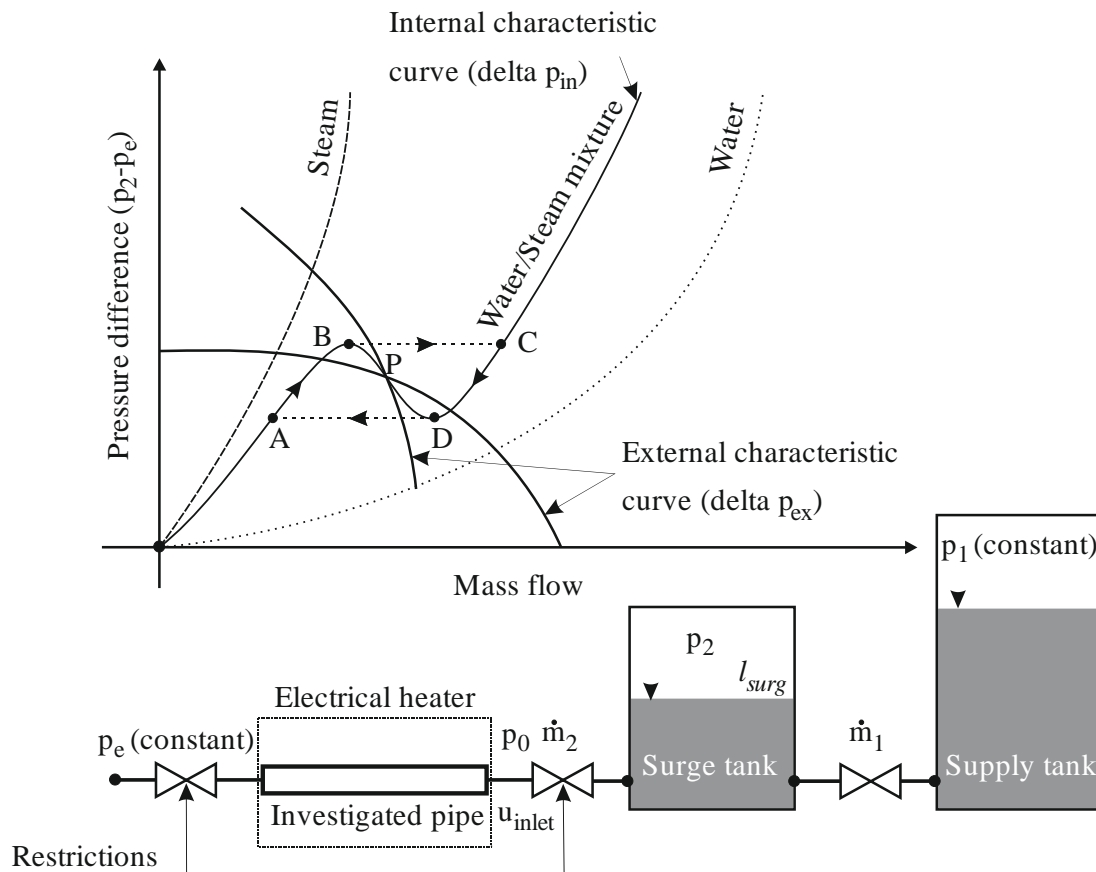


Figure 4.6 Pressure drop oscillations [106]

4.3.3 Thermal Oscillations

Thermal oscillations are a consequence of the mass flow rate oscillations that occurred in the evaporator tubes by the reason of previously explained density-wave and pressure-drop oscillations. The evaporator inlet fluid temperature and the heat input are usually constant at the steady-state operation of the power plant. The mass flow rate variations that occur in the evaporator tubes can lead to a variable thermal response of the heated wall due to the variable heat transfer coefficient. These variations cause different wall overheating in the tube due to inadequate cooling of the tube wall and that can get coupled with the DWO. This overheating of the tube walls leads to thermal failure, which usually manifests itself in the form of burnout of the wall.

The appearance of these thermal oscillations is highly undesirable specifically at the high temperatures of the HRSGs. These oscillations not only can degrade system performance but can also lead to early fatigue and control problems that can become devastating.

- Interaction of variable heat transfer coefficient with flow dynamics.
- Large fluctuations of the heated channel wall temperature.
- Thermal stresses on the heated tube.
- Burn-out of the heat transfer surface.

Thermal oscillations usually occur as a part of or result of other dynamic instabilities and are important in thermal management applications.

4.4 Characteristic Pressure Curves

To investigate the dynamic instabilities of two-phase flow in boiling systems such as the low pressure or high-pressure evaporators, the internal characteristic curves of these evaporators should be obtained. The reason for selecting the low-pressure evaporator ($p \leq 10$ bar) is that in the high-pressure evaporators the high pressures lead accordingly to damp the oscillations. Therefore, the flow instabilities in the low-pressure evaporators represent here the worst case and thus are analysed. At the previous operating inlet conditions, $p_{in} = 3.95$ bar, $T_{in} = 92$ ° C and $\dot{Q} = 6000$ W, in captures shown in **Figure 4.2**, the internal characteristic curve of the evaporator tube was obtained by A. Temraz et al. [106]. The measured pressure drop in [mbar] was plotted versus the mass flow rate in [kg/h], as shown in **Figure 4.7**.

The measurements show a change in the slope of the curve from positive to negative and back again to a positive slope, and this is known as the N-shape curve (behavior) as shown in **Figure 4.7**. For a mass flow rate of approx. ($\dot{m} \leq 25$ kg/h), the water enters the evaporator tube as a single phase, as a liquid, and leaves it again as a single phase in vapor as seen in **Figure 4.2**. From a mass flow rate of approx. ($\dot{m} \geq 75$ kg/h), the heat flow is not sufficient to heat the liquid until the state of saturation is reached so the water flows through the evaporator tube in one phase, as a liquid. So there is a region in the evaporator tube in which the water flows in two phases, as a liquid-vapor mixture.

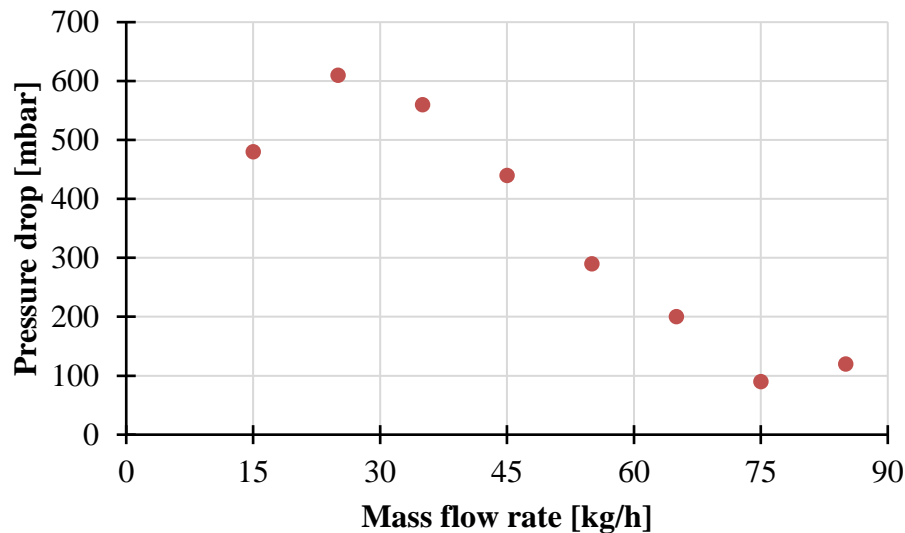


Figure 4.7 Measured pressure drop for water through the evaporator tube [106]

In **Figure 4.7**, the pressure drop through the evaporator tube increases with the increase of the mass flow rate in single-phase regions ($\dot{m} \leq 25$ kg/h, and $\dot{m} \geq 75$ kg/h). Between these two mass flow rates, i.e. in the area in which (25 kg/h $< \dot{m} < 75$ kg/h) applies, the fluid flows within the evaporator tube in two phases. So, the negative slope region in the internal characteristic curve of the evaporator tube is due to the existence of the two-phase flow within the evaporator tube in the area in which (25 kg/h $< \dot{m} < 75$ kg/h) applies, as shown in **Figure 4.7**. That may be due to the larger increase of the friction pressure drop in the two-phase flow compared with the liquid single-phase flow, the net effect is the increase in the pressure drop with the decrease of the mass flow rate [110].

The frictional pressure drop occurs when frictional forces reduce the velocity of the fluid and the decrease in the fluid velocity causes a decrease in the enthalpy, resulting in the pressure drop. In the two-phase flow, there is a slip between the liquid and the vapor phases and this slip increases the frictional pressure drop. The negative slope region in the internal characteristic curve of the evaporator tube is the main responsible for the occurrence of the dynamic instabilities in two-phase flow tube boiling [55], [104], [109]–[111].

4.5 Characterization of the Developed Test Rig

Modern HRSGs usually consist of three pressure levels (low-, medium- and high-pressure levels). This series of pressure levels is required to minimize the area between the flue gas and steam temperatures. Thus, the exhaust enthalpy can be used for more efficient steam generation. Each level consists of an economizer, evaporator and super-heater. As already mentioned in the introduction, the main focus of this experimental stand is on the vertical HRSGs with horizontal pipes. The evaporator tube of the test rig is a geometrically reduced version of a single low-pressure evaporator tube of a vertical HRSG, as will be explained in details later in this chapter.

As a sequence of the design process, basic and schematic concepts for the start-up process of a natural circulation in which the desired flow direction can be specified are involved. Based on these variants, a detailed design had been created in which the arrangement of valves, vessels,

pressure gauges, etc. was taken into account in the form of a P&ID circuit diagram as shown in **Figure 4.8**.

Finally, from the information provided by the P & ID as well as the data to be taken from the similarity scaling and the standards, a visualization of the test rig was created in the CAD program NX10.0 as shown in **Figure 4.9**.

Since the heated test tube was made of AISI 316 stainless steel and has electrical resistance, direct current can be applied directly to the pipe and generate heat, which can determine the heat supply via the current and the voltage. Teflon connections were used at both ends of the evaporator tube for electric insulation. For the heat to be transferred into the fluid, the heated test tube was adiabatically insulated. In conclusion, the evaporator tube gives off hardly any heat to the environment and the heat input into the working medium was almost identical to the electrical power.

To reduce the heat losses from the test rig to the environment, the pipelines, as well as the main supply tank (MST) and overflow tank (OFT), were insulated so that the heat required to reach the steady-state operation remained low.

The pressure at the inlet is adjusted by nitrogen, which is connected via pipes to the different water tanks. A flowmeter is mounted in front of the preheater and measures the mass flow rate that enters the evaporator tube. Besides, the mass flow rate at the entry of the evaporator tube is regulated by the inlet restriction (in the form of a needle valve). There is a sight glass at the outlet of the evaporator tube to observe the existing flow pattern and record it using a high-resolution camera.

The pressure drop in the preheater pipe can be varied via an exit restriction (needle valve). A needle valve is mounted at the outlet of the heated test tube, whereby it is possible to adjust the flow resistance and thus to analyze the resulting pressure drop. Also, the needle valve can be completely closed, allowing the pressure drop to be examined over a parallel line.

A nitrogen bottle is used to set the absolute pressure in the system as well as in the compressible volume. Thus, all containers can be filled independently. To prevent critical pressures in the system, two safety valves were connected in series with the preheater and the evaporator tube. The valves open at a pressure of 10 bar and there is no way to decouple them from the respective heated test tube.

As previously mentioned, PDOs only occur in systems with a sufficiently large compressible volume. The compressible volume is a physical material quantity that describes which direction independent pressure load is necessary to produce a given volume change. It is calculated from the volume, as well as the difference between an infinitesimal pressure change and an infinitesimal volume change. The compressible volume can be connected to or disconnected from the circuit by a ball valve. This depends on whether PDOs or DWOs are to be investigated.

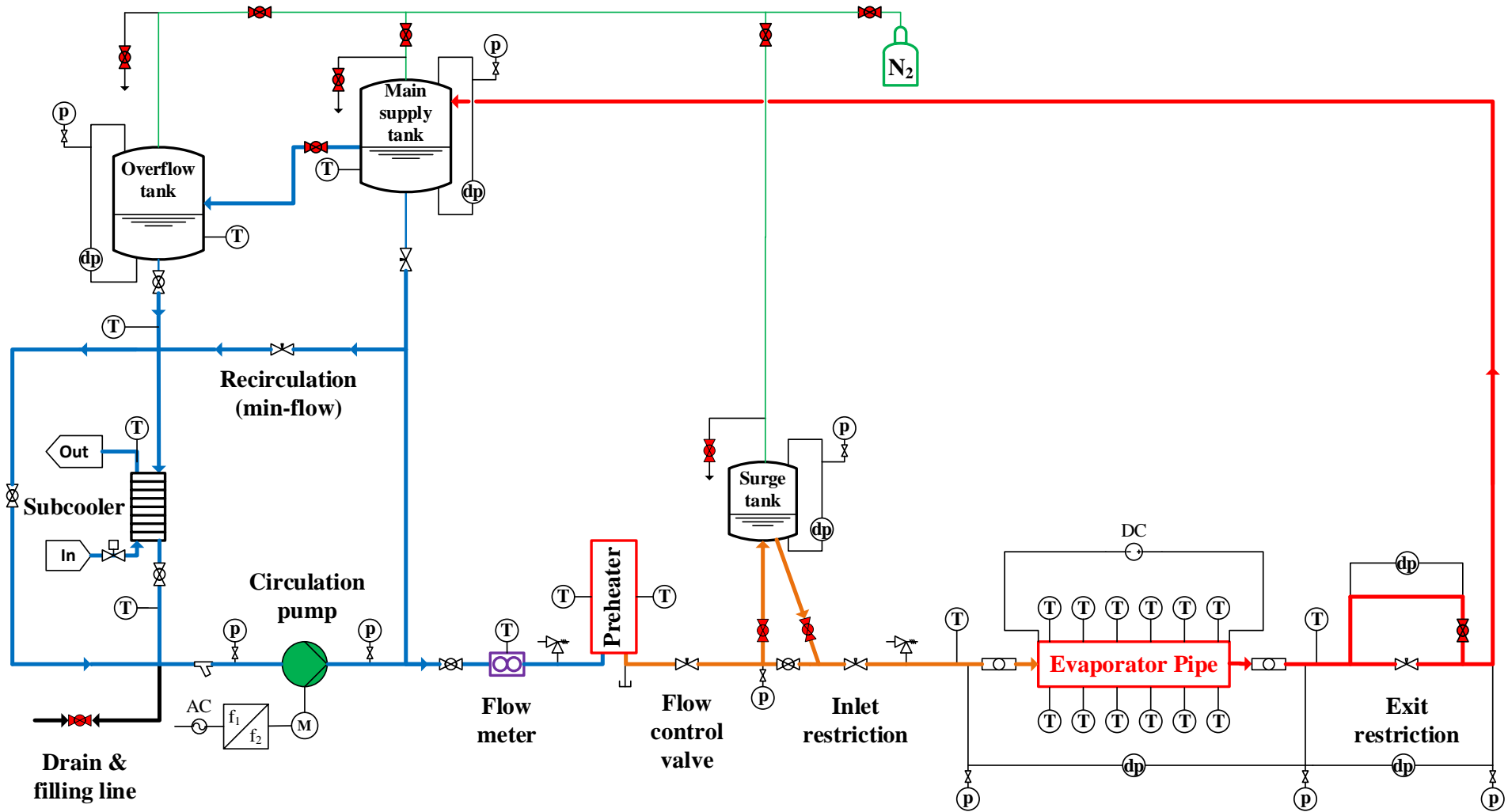


Figure 4.8 Process and instrumentation diagram of the developed test rig

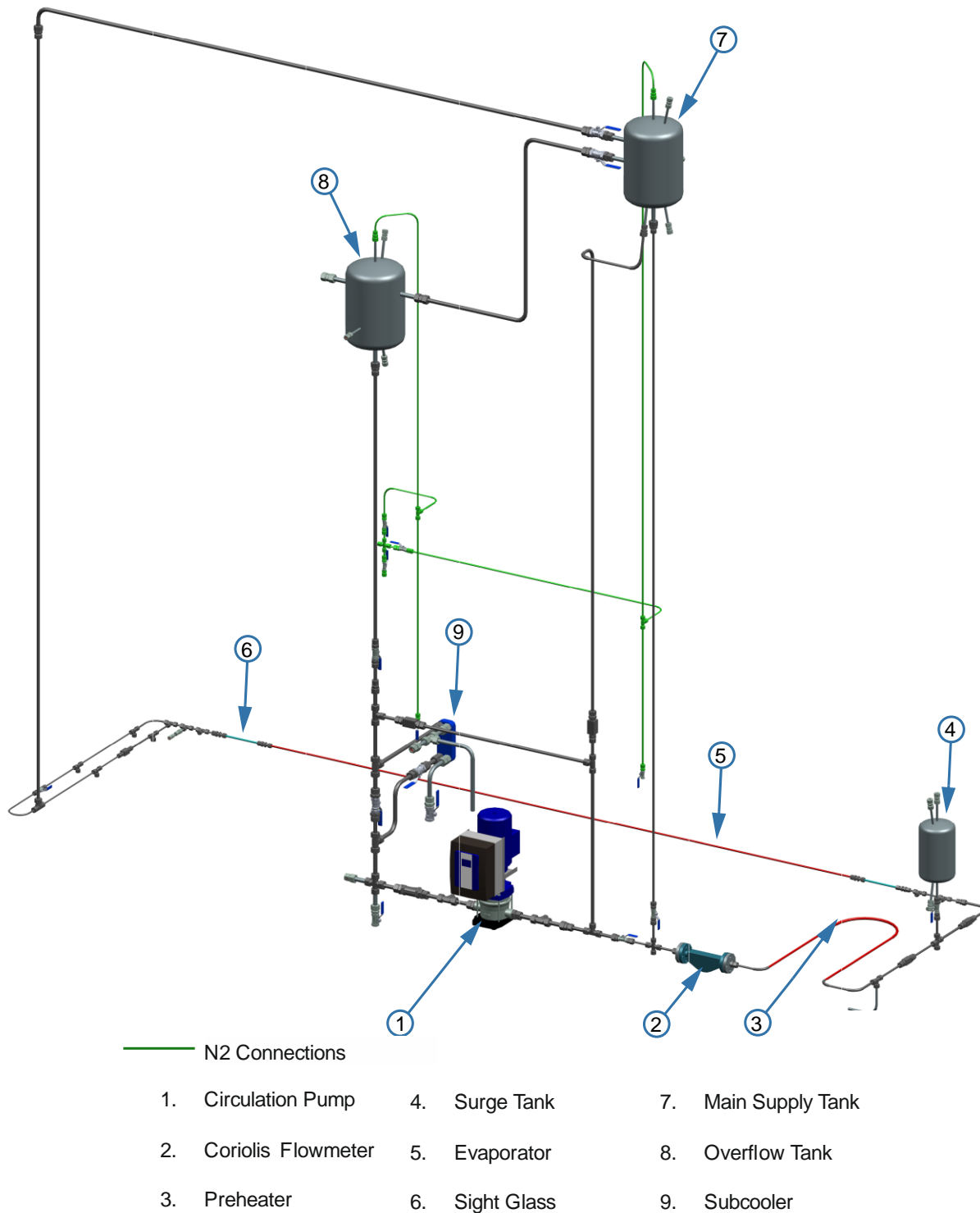


Figure 4.9 CAD model of the developed test rig

The instruments of the test rig are controlled and monitored with a graphical user interface (GUI) developed by the LabVIEW program, as shown in **Figure 4.10**. This program was established as a standard in the engineering and natural sciences, especially in the areas of measurement, control technology, simulation, and data acquisition, analysis and visualization. Another reason for choosing this program lies in the simplified programmability in contrast to conventional text-based programming languages. The principle is based on prefabricated and partially combinable graphic blocks, each having a specific source code. Thus, complex programs can be created in a clear block diagram. Besides, it is possible to create a GUI via a selection of different elements.

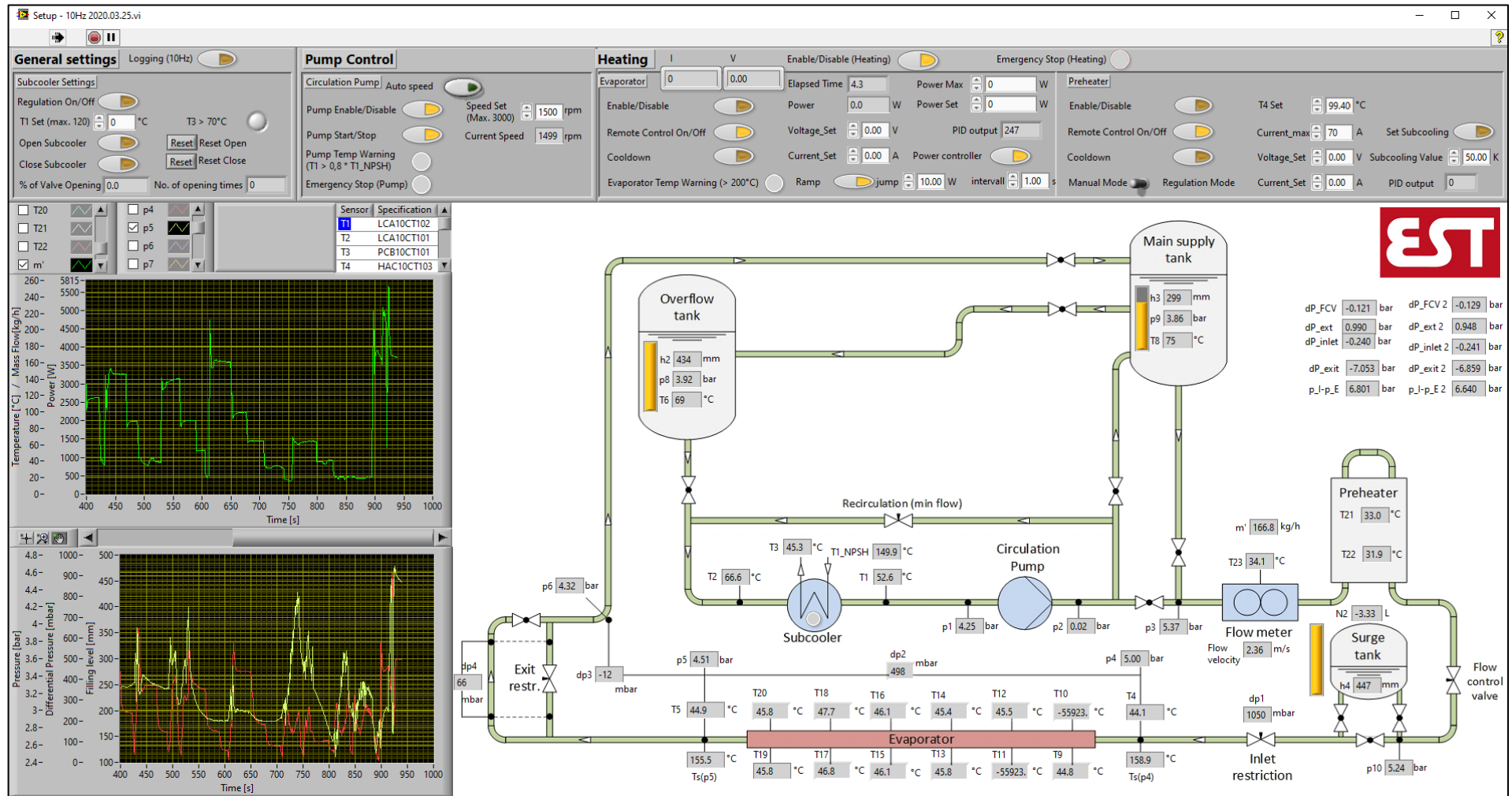


Figure 4.10 The GUI of the two-phase flow test rig developed by the LabVIEW program

4.5.1 Design of Evaporator Tube

To provide hydraulic consistency of the flow behavior of different systems, the similarity criteria are introduced. As a reference for the test rig constructed in this work, the HRSG from Doosan Heavy Industries and Construction in **Table 4.1** has been used.

Table 4.1 Data of the reference HRSG (provided to TU Darmstadt by Doosan)

Design parameters	Value	Units
Number of paths	4	[-]
Number of layers per path	7	[-]
Number of parallel tubes per layer	46	[-]
Inner tube diameter (D_i)	33.3	[mm]
Heated length of tubes (over one path)	20.5	[m]
Absorbed heat per tube over all paths	94200	[W]
The inlet pressure (first path)	5.73	[bar]
The inlet temperature (first path)	151	[°C]
The inlet mass flux (first path)	120.7	[kg/s·m ²]

By the similarity criteria, it was possible to design the heated test tube with reduced dimensions, but with thermohydraulic similar behaviour to the original large-scale evaporator. Similarity criteria have been obtained from conservation equations, boundary conditions, and geometry of a system, as described in detail in [112]. For two-phase flow, the similarity criteria have been derived from perturbation analysis based on the - dimensional drift-flux model. The system was calculated by using the dimensionless characteristic numbers, dynamic, kinematic, and energetic scaling.

To achieve a geometric similarity of different arrangements, the ratio of the inner diameter to the length of the pipe ($\frac{D_i}{L}$), for both pipes, must be equal.

The scaling of the subcooling over the evaporation temperature was made using the subcooling number (N_{sub}) which represents the ratio of sensible and latent heat. This is one of the fundamental parameters to be considered in the stability analysis.

$$N_{sub} = \frac{h_f - h_i}{h_{fg}} \frac{\rho_f - \rho_g}{\rho_g} \quad (4.2)$$

where h_f , h_i and h_{fg} are the specific enthalpy of liquid, the specific enthalpy of the fluid at the inlet of the test pipe and the specific enthalpy of vaporization, ρ_f and ρ_g are the density of the liquid and the vapor, respectively.

To achieve identical flow conditions and a similar turbulence behaviour in both arrangements, the Reynolds number (Re_i) at the inlet of the evaporator was calculated. An identical flow pattern is guaranteed by achieving the same Reynolds number in both evaporator tubes.

$$Re_i = \frac{\rho * u * D_i}{\mu} \quad (4.3)$$

where ρ is the density of the fluid, u is the flow velocity and μ is the dynamic viscosity of the fluid.

The last relevant number is the phase change number (N_{pch}). The phase change number (N_{pch}) describes the phase change of the working fluid due to the heat input. It gives significant hints in the description of the equilibrium points, as well as in the stability limits.

$$N_{pch} = \frac{\dot{Q}}{G * A_i * h_{fg}} \frac{\rho_f - \rho_g}{\rho_g} \quad (4.4)$$

where \dot{Q} is the rate of heat transfer, G is the mass flux and A_i is the inner cross-section area of the pipe.

Based on the data provided in **Table 4.1**, the similarity and scaling criteria were performed. In the calculation of these dimensionless numbers, the capillary forces are assumed that negligible. Furthermore, it was assumed that the flow is incompressible and therefore the dissipation forces were not considered in the energy conservation equation [112]. Besides, the influence of the friction heat is significantly small in comparison with the supplied heat.

Table 4.2 The values of the dimensionless numbers

Similarity criterion	Value	Units
Geometrical similarity	~600	[-]
Subcooling number (N_{sub})	3.7	[-]
Phase change number (N_{pch})	60.8	[-]
Reynolds number (Re_i)	23107	[-]

Based on the values of the dimensionless numbers shown in **Table 4.2**, the design of the test rig was carried out. The range of experimental parameters (pressure, temperature, heating power and mass flux) of the test rig are shown in **Table 4.3**. Furthermore, it is possible to change the inside diameter of the evaporator tube from 5 mm to 8 mm. Also, the length of the heated pipe in the test pipe is variable, so you can either install a 2 m or 3 m long pipe as needed.

Table 4.3 Characteristics of the developed test rig

Design and operational parameters	Value	Units
The hydraulic diameter of the evaporator tube	5	[mm]
Heated length of the evaporator tube	3	[m]
The inlet pressure of the evaporator tube	2 - 8	[bar]
Heating power	0 - 15000	[W]
Mass flux	0 - 2000	[kg/s·m ²]

4.5.2 The Orientation of the Heated Test Tube

Intending to further increase the versatility of the system, there is a pipe fitting just before the test pipe. This fitting makes it possible by a small effort to convert the evaporator tube from the

horizontal to a vertical orientation and vice versa. This offers the advantage that both horizontal HRSGs with vertical evaporator tubes and vertical HRSGs with horizontal evaporator tubes can be examined.

4.5.3 Modes of Operation

For using the test rig for a wide range of possible experiments with different external characteristics, it offers the possibility to vary between the natural circulation and the forced circulation, as a drive for circulating the water in the test loop. Thus, from the results of measurements obtained later, a balance can be mentioned between the influence of natural circulation and forced circulation on the dynamic instabilities of the two-phase flow.

4.5.3.1 Forced Circulation

In the forced circulation mode, the pump is permanently operated to circulation and specifies the flow direction and the mass flow rate of the entire system. During the selection of the pump, the typically used gear pump could not be chosen due to the high temperature of the test fluid (water) of about 170 °C. Because in the case of choosing the gear pump, it must be lubricated by the pumped medium but the viscosity of water is too low at these high temperatures. Even though the extra cooling would increase the viscosity of the water, but the fluid would need to be re-heated to a required subcooling temperature before entering the test section. In the design, a centrifugal pump was chosen that can circulate the water at higher temperatures. To avoid cavitation in the centrifugal pump, the temperature of the circulated water is reduced using the subcooler before the circulation pump. However, the water temperature shouldn't drop too much before the pump because it must be heated again in the preheater to the desired subcooling temperature at the evaporator tube. The control of the cooling capacity of the subcooler depends on the amount of tap water flowed through it. The tap water is controlled by a control valve at the inlet, together with the temperature measurements. The control is intended to prevent the evaporation of tap water in the subcooler to prevent the reduction of the cooling capacity of the subcooler. Besides, the pump has a self-cooling frequency inverter that enables continuously variable speed control that can be used to control the external characteristics of the system.

4.5.3.2 Natural Circulation

The second mode to operate the test rig is the natural circulation mode. The test rig is mainly constructed for the investigation of flow instabilities in vertical HRSG, which are driven by natural circulation. In general, flow instabilities occur more frequently in natural circulation steam cycles, since the available driving force is lower than the driving force generated by the pump during the forced circulation. For this reason, the physical mechanism of natural circulation is described in detail. The test rig consists mainly of the main supply tank (MST), a downcomer and a riser as shown in **Figure 4.9**. The MST acts as a drum in the natural circulation loop.

In the case of a vertical heated pipe, the density difference between the water-steam mixture in the riser and the water in the downcomer is sufficient to maintain a constant mass flow rate with the aid of gravity, which requires no pump. It is problematic when it comes to a vertical HRSG with horizontal tubes because the resulting water-steam mixture has no guaranteed flow direction due to a lack of gravity influence. Since the heated pipe in the test rig is arranged in a horizontal orientation, the steam has no preferred axial flow direction. The starting of the water circulation is

often a problem because of the horizontal orientation of the heated pipe. In the following, two different concepts are introduced in the test rig to solve this problem. The experiments can be started in the natural circulation mode of operation in two ways. The positive side effect of the design is a stabilization of the overall system by the pressure generated using the nitrogen. This nitrogen can be used to generate pressure in the main supply tank as the first concept. Furthermore, the start-up process with the pump is also represented in the system since the pump is also connected in natural circulation mode to supply the MST with feed water before starting the experiment. Also, the pump can be used at the beginning of the evaporation process, this can give the fluid a flow direction as the second concept.

4.5.4 The Test Rig Instrumentation

The inlet and outlet pressure of the test section is measured by two pressure transducers. The test rig is equipped with 9 pressure sensors and 6 pressure difference sensors that measure tank levels, pressure drops, and mass flow rate oscillations. It is also equipped with 22 thermocouples that measure the temperature of the water inside the tanks, the temperature distribution on the heated pipe (evaporator) and the temperatures of the water upstream and downstream the subcooler, the circulating pump, the preheater and the heated tube. The position of all measurement devices is illustrated in **Figure 4.8** and **Figure 4.10**. And for mass flow rate measurement, a Coriolis flowmeter is installed before the preheater. It also measures the density and temperature of the water. The accuracy of these measurement devices is presented in **Table 4.4**. Other variables such as volume flow can be calculated by using these parameters. All data such as the mass flow rate, the pressure drop across the test pipe and the temperatures are recorded during each experiment by a data acquisition (DAQ) system through measuring modules from National Instruments (NI 9208, NI 9211, and NI 9213).

Table 4.4 The accuracy of the test rig measurement devices

Parameter	Instrument	Uncertainty
Relative pressure	Pressure transducer	$\leq 0.5\%$
Differential pressure	Differential pressure transmitter	$\pm 0.04\%$
Temperature	Type T thermocouple	$\pm 0.5\text{ }^{\circ}\text{C}$ or $0.004 \times T\text{ }^{\circ}\text{C}$
Mass flow rate	Coriolis flowmeter	0.2%
Thermocouple input modules	NI 9211, NI 9213	0.16%
Pressure and mass flow input module	NI 9208	0.8%

4.6 Results and Discussion

The change of the pressure drop with the mass flow rate for the evaporator tube was obtained to help in the identification of the dynamic instabilities, the internal characteristic curves. **Figure 4.11** shows the internal characteristic curve of the evaporator tube for water entering the tube with a pressure of about 3 bar and inlet subcooled temperature of about $60\text{ }^{\circ}\text{C}$, with a constant uniform

heating power of 5000 W. The measurements show that the change in the slope of the curve from positive to negative occurred at the mass flow rate of 15 kg/h and back again to a positive slope at the mass flow rate of 65 kg/h.

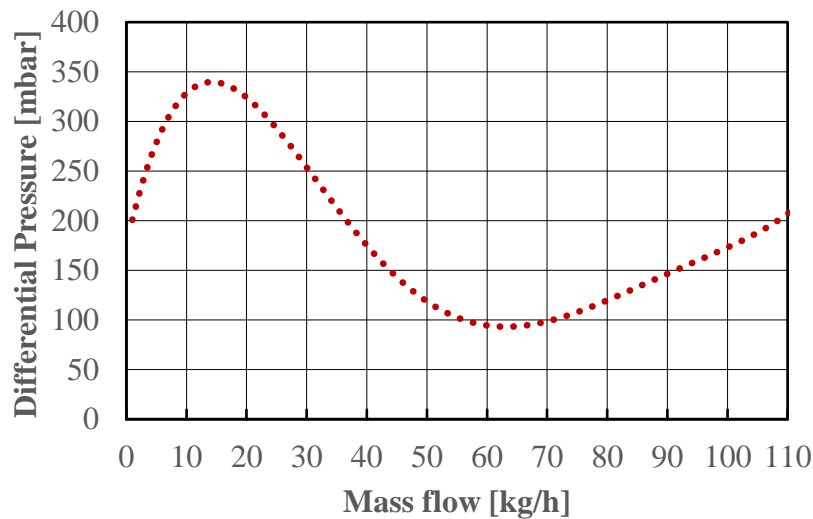


Figure 4.11 The internal characteristic curve of the evaporator tube

The experimental investigation of DWO, PWO, and thermal oscillation was carried out within two campaigns. The following sections present the experimental results of the first campaign, and the experimental results of the second campaign are provided in the Appendix A.

4.6.1 Density Wave Oscillation

The DWO was obtained at the operating conditions of inlet pressure and temperature of about 3 bar and 60 °C, respectively and heating power of 5000 W. **Figure 4.12** shows the histogram of the mass flow rate beside the oscillation of the mass flow rate in the time domain for the DWO. As shown in this figure, the mass flow rate started to oscillate between 1 kg/h and 7 kg/h with an amplitude of 6 kg/h then continued to oscillate with a lower amplitude of 2 kg/h.

The analysis of signals can often be described more simply and more clearly in the spectral domain (frequency domain). The time-domain chart reveals how the oscillations changes in time. The knowledge of the frequency or frequencies with which the signal changes is usually more interesting than simply observing the vibration curve in the time domain. Here, the signal is represented at different frequencies instead of representing the signal amplitude as a function of time. Frequency information is one of the most important pieces of information (along with amplitude) for evaluating the potential impact of different dynamic instability modes but is not a reliable method for classifying different instability modes. The form of representation in the frequency domain is the decomposition of periodic continuous signals into Fourier series. For most signals, the spectral characteristics can be obtained by applying a Fourier transform, as an example of the Fourier series. Fourier transform offers an alternate way of representing the results. Spectral analysis using a Fourier transform is often used to determine the frequency composition of unknown signals, periodic or non-periodic. Since the signals of the dynamic oscillations are aperiodic (non-periodic) signals, because they don't repeat themselves after a regular interval of time, the Fourier transform is used to present the frequency domain of the oscillation signals. **Figure 4.14** shows the Fourier spectrum of the mass flow rate oscillations during the DWO.

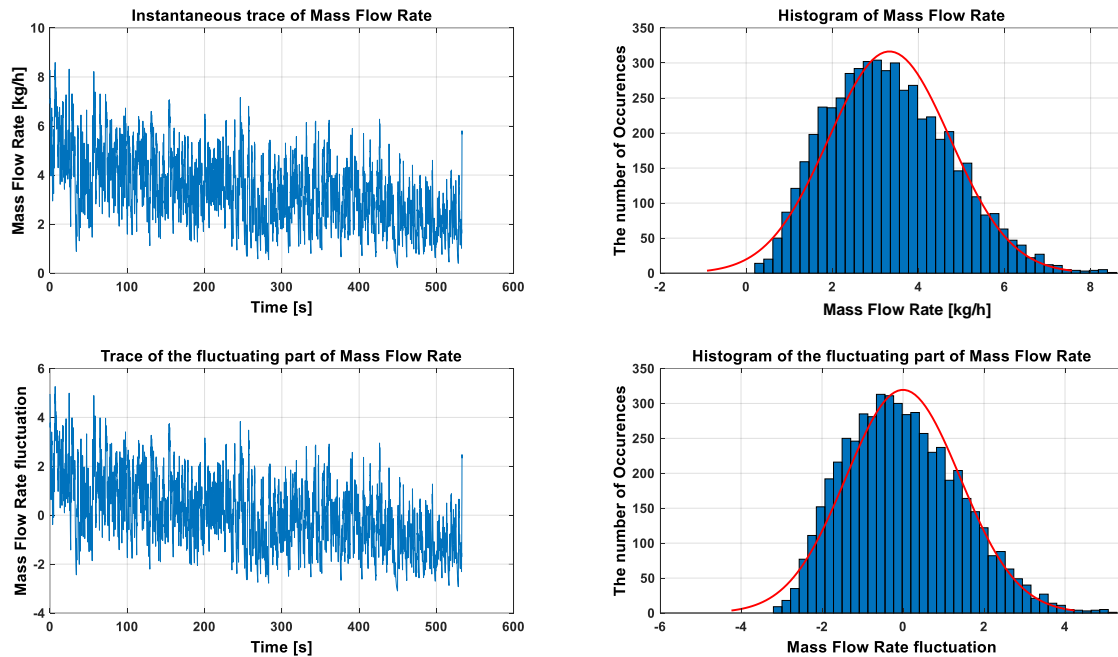


Figure 4.12 The variation of the inlet mass flow rate of the evaporator tube during the DWO

As shown in the **Figure 4.14** and **Figure 4.15**, the DWOs are compressed in the time domain and expand in the frequency domain which means that the DWO has low-frequency components as shown in the frequency domain chart because there is an inverse relationship between time and frequency domain. That means that the changing rate of the DWO is very high with frequencies between 0.04 and 0.1 Hz. This means that the main component cycle of the DWO takes from 10 to 25 sec to repeat itself. These oscillations can be identified as DWO while the surge tank, compressible volume, was not connected during the experiment and the evaporator tube is not very long ($L/D < 150$) [51], [113], [114].

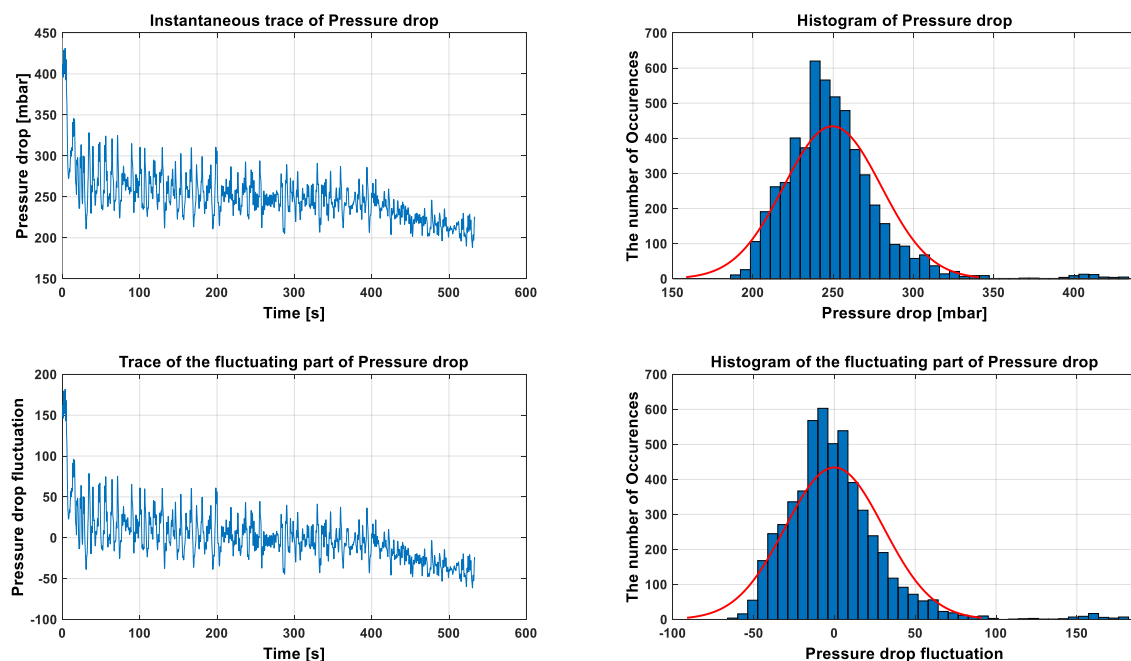


Figure 4.13 The variation of the pressure drop in the evaporator tube during the DWO

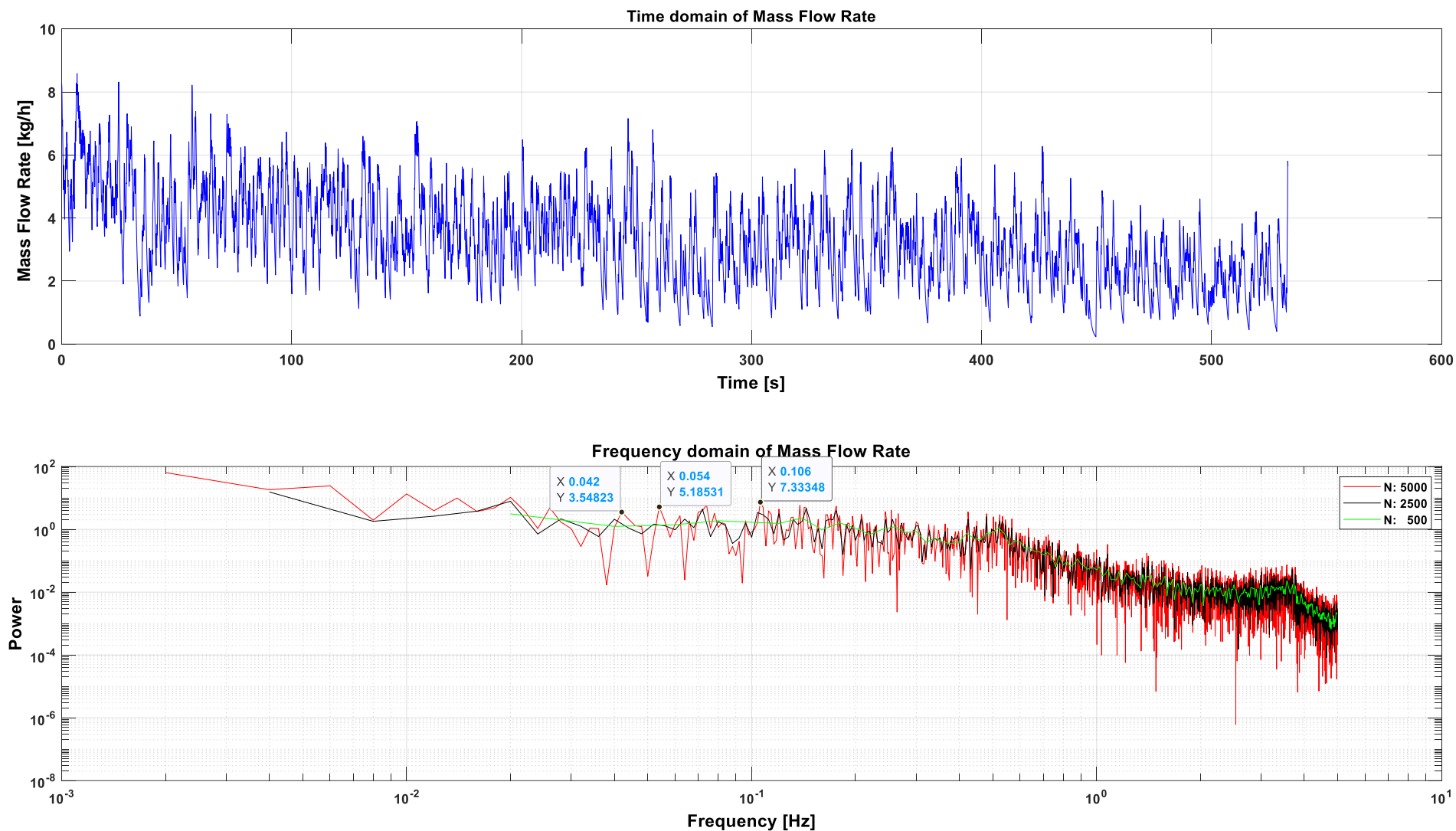


Figure 4.14 The variation of the inlet mass flow rate of the evaporator tube during the DWO in the frequency domain

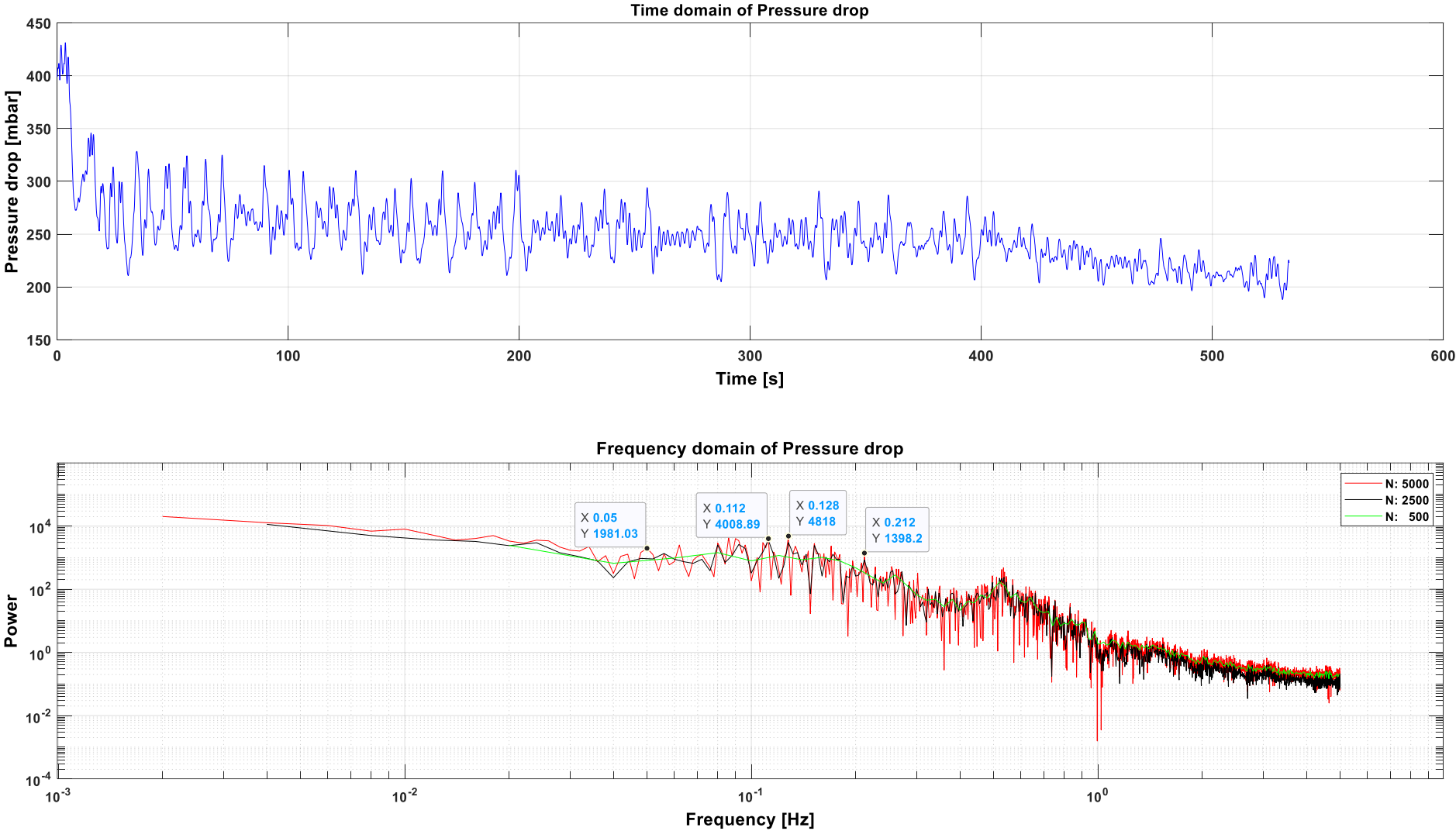


Figure 4.15 The variation of the pressure drop in the evaporator tube during the DWO in the frequency domain

The oscillation of the pressure drop in the evaporator tube during the DWO starts with an amplitude of 100 mbar and then decreases gradually, as shown in **Figure 4.13**. The histogram indicated that the pressure drop oscillated most of the time between about 230 and 270 mbar. The main component of the pressure drop oscillation during the DWO is in the frequencies range of about 0.05 to 0.12 Hz, as shown in **Figure 4.15**. This means that its oscillation has a period of about 8 to 20 sec.

4.6.2 Pressure Drop Oscillation

To study pressure-drop oscillations, a compressible volume is installed upstream of the evaporator tube. The surge tank can be connected to investigate the PDO and disconnected to investigate the DWO from the circuit via a ball valve. The compressible volume can be adjusted through different water levels in the tank. The surge tank was connected with a nitrogen bottle with pressure 200 bar. The nitrogen pressure was controlled using a pressure reduction valve connected to the bottle. The experimental investigation of the PDO started with a heating power of 5000 W. But due to the temperature oscillation associated with the PDO as a result of the mass flow rate fluctuation the temperature of two parts from the six part of the evaporator tube exceeded the maximum temperature limit of 200 °C. Thus, the heating power was reduced to avoid the shutdown of the heating system due to the high surface temperature of the evaporator tube.

The PDO was obtained at the operating conditions of inlet pressure and temperature of about 3 bar and 70 °C, respectively and heating power of 3000 W. The histogram of the pressure drop oscillations that occurred at these conditions is shown in **Figure 4.16**. The pressure drop started to oscillate between 10 mbar and 150 mbar with an amplitude of 140 mbar then it continued to oscillate with a lower amplitude of about 100 mbar. The signal in the time domain indicated that the PDO was interfered with another type of oscillation after the first ten minutes as shown in **Figure 4.16**. The signal after this type has two different frequencies and this repeated until the oscillation was damped by increasing the mass flow rate to avoid the burnout of the evaporator tube.

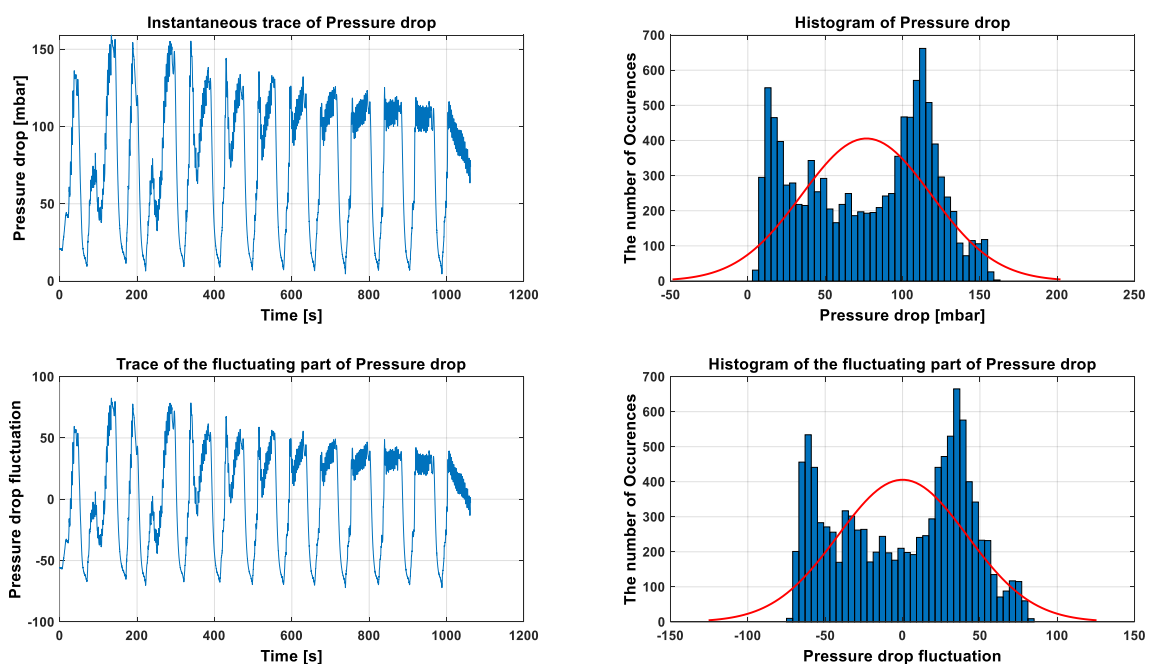


Figure 4.16 The variation of the pressure drop in the evaporator tube during the PDO

In **Figure 4.16**, the representation of these pressure drop oscillations in the frequency domain is shown. This figure shows that the frequencies range of these oscillations is between 0.012 and 0.024 Hz. That means that the cycle of the PWO takes 40 to 80 sec to repeat itself. This is also the same in the representation of the mass flow rate oscillations associated with this PDO in the frequency domain, as shown in **Figure 4.19**.

Figure 4.17 shows the histogram of the mass flow rate associated with these pressure drop oscillations beside its oscillations in the time domain. As shown in this figure, the mass flow rate started to oscillate between 20 kg/h and 24 kg/h with an amplitude of 4 kg/h then continued to oscillate with a lower amplitude of 2 kg/h. The PWO was clearly recognized by the fluctuation of the pressure drop in the evaporator tube, unlike the DWO. The fluctuation of the mass flow rate associated with the DWO was clearer recognized than the fluctuation of the pressure drop in the evaporator tube.

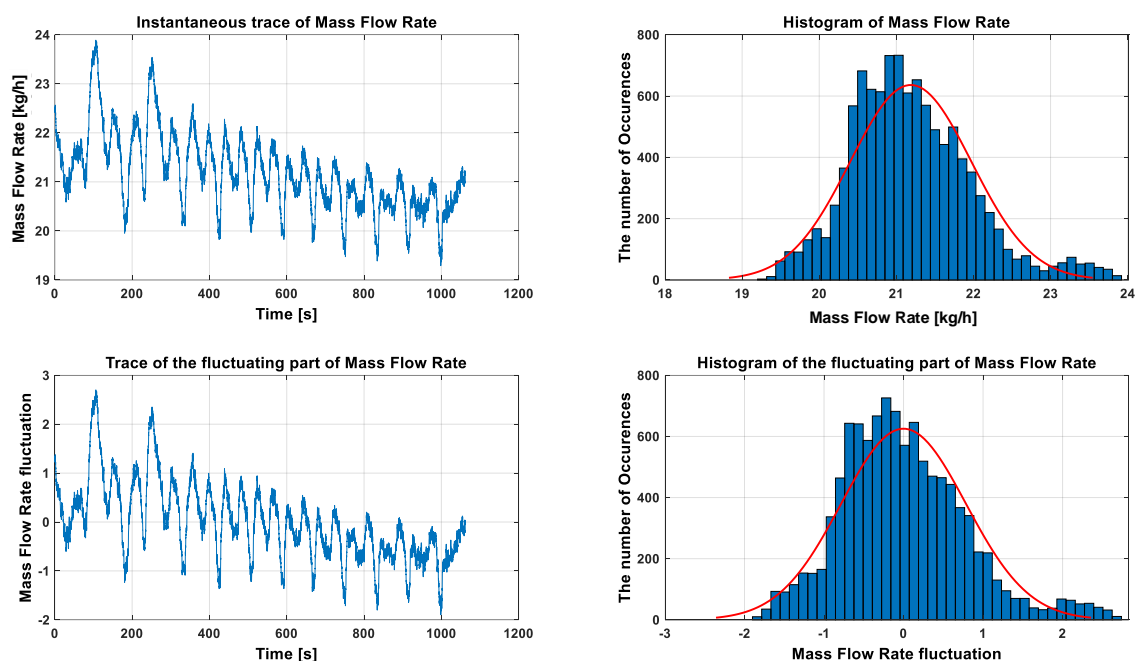


Figure 4.17 The variation of the inlet mass flow rate of the evaporator tube during the PDO

The onset of PDO was based on the zero slope of the internal characteristic curve [51] and these mass flow rate values in addition to the existence of the compressible volume, surge tank, indicate that these oscillations are PDOs. And as mentioned in the literature, the PDOs occur in the negative slope part of the internal characteristic curve, like the Ledinegg instability [113]. As shown in **Figure 4.17** and **Figure 4.19**, the system start to oscillate at mass flow rate of about 23 kg/h which was in the negative slope part of the internal characteristic curve of the evaporator tube. Unlike the DWO which started at a mass flow rate of about 10 kg/h that located in the positive slope part of the internal characteristic curve of the evaporator tube under investigation.

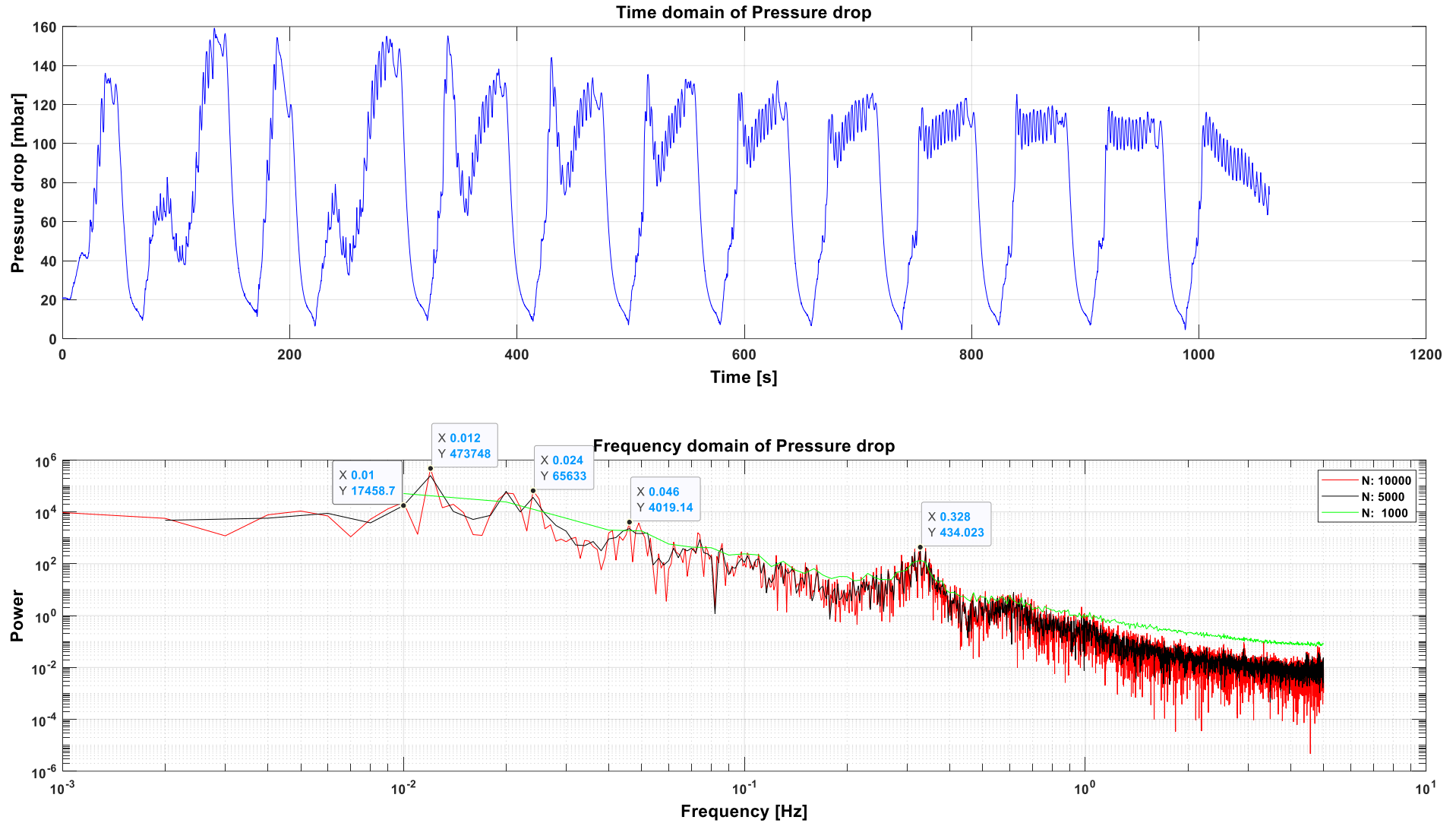


Figure 4.18 The variation of the pressure drop in the evaporator tube during the PDO in the frequency domain

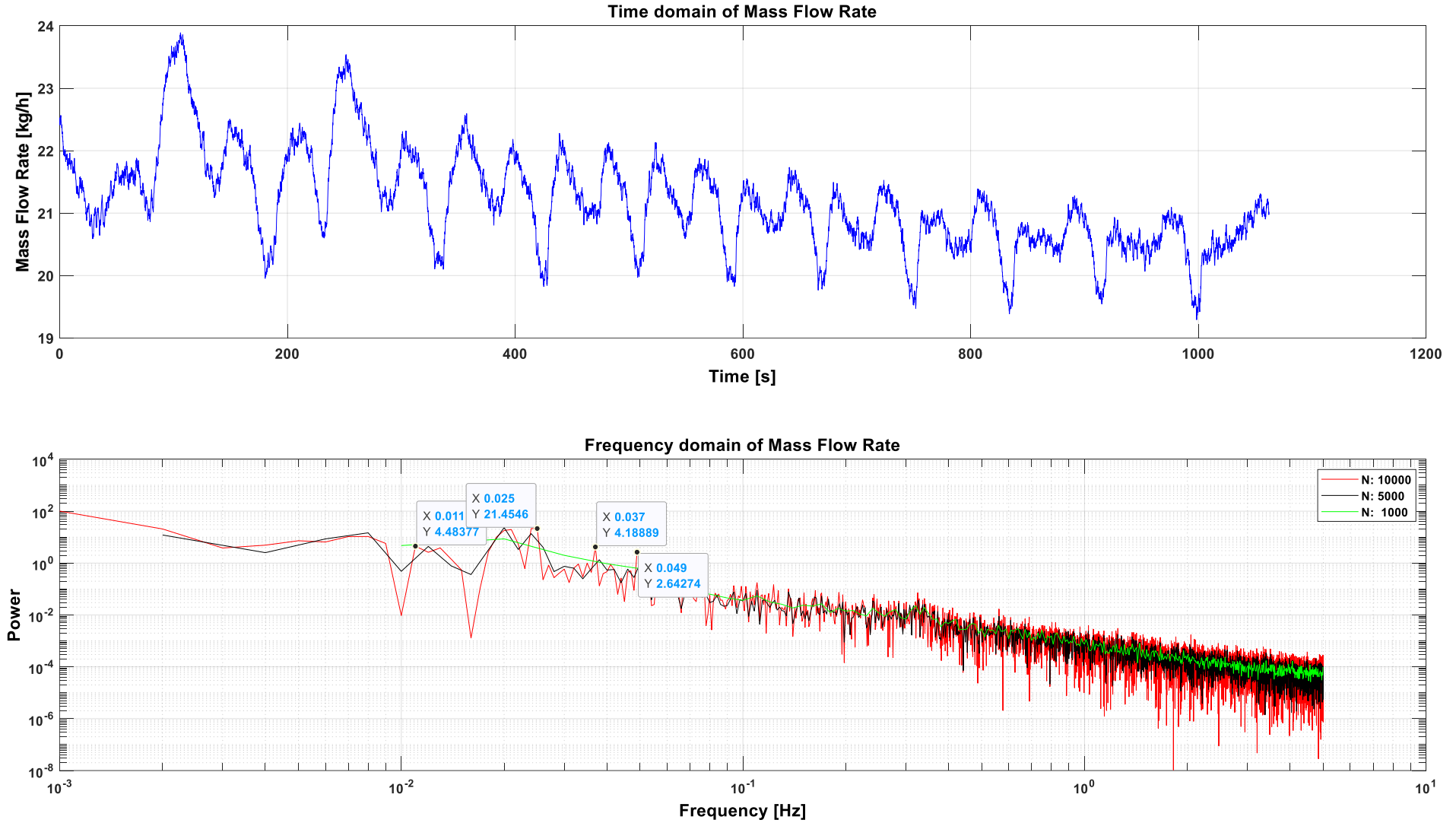


Figure 4.19 The variation of the inlet mass flow rate of the evaporator tube during the PDO in the frequency domain

The oscillations of the mass flow rate during this PDO are represented in the frequency domain as shown in **Figure 4.19**. The main component of the oscillation signal has a frequency between 0.011 and 0.025 Hz, almost the same frequencies as the pressure drop oscillations. The interference of the PDO with another type of oscillation wasn't manifest in the oscillation of the mass flow rate into the evaporator tube. This may be due to the existence of a compressible volume in the loop. This slow response due to the existence of the surge tank in the loop, as a compressible volume, allowed the system to adapt with the oscillation and produce a long PDO signal without producing a lot of steam and sharply increase the loop pressure as the case of the DWO.

4.6.3 Thermal Oscillation

The thermal oscillations are a consequence of the mass flow rate oscillations that occurred in the evaporator tubes by the reason of the density-wave and pressure-drop oscillations. The evaporator inlet fluid temperature and the heat input are almost constant during the experiment. The mass flow rate fluctuations that occur into the evaporator tube lead to a variable thermal response of the heated wall due to the variable heat transfer coefficient. These variations cause different wall overheating in the tube due to inadequate cooling of the tube wall and that can get coupled with the DWO. This overheating of the tube walls leads to thermal failure, which usually manifests itself in the form of burnout of the wall.

The surface temperature distribution along the evaporator tube during the DWOs and the PDOs are shown in **Figure 4.20** and **Figure 4.21**, respectively, concerning the thermocouples order in **Figure 4.10**. Where twelve thermocouples were installed on the surface of the evaporator tube at six locations, six parts of the evaporator tube, T10 at the beginning of the tube and T20 at the end.

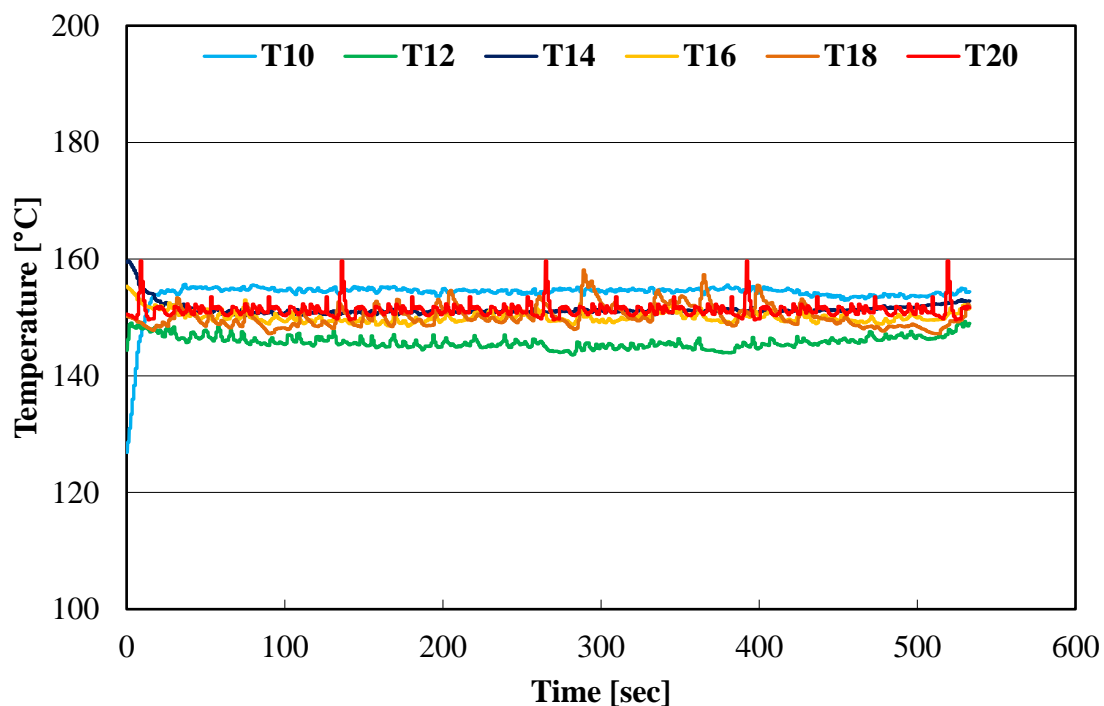


Figure 4.20 The variation of the surface temperature along the evaporator tube during the DWO

As revealed in **Figure 4.20**, the evaporation of the water starts at the end of the first third of the evaporator tube, at T12, because the high heat transfer coefficient of the evaporation decreased the surface temperature than before, at T10.

The thermal oscillations occur as a result of the mass flow rate oscillation due to the previous mentioned dynamic instabilities, DWO and PDO. **Figure 4.20** shows the surface temperature oscillation along the evaporator tube associated with the DWO. The high frequency of the mass flow rate oscillation during the DWO causes a small amplitude of surface temperature fluctuation.

In the case of fluctuating the mass flow rate with low frequency, like in the PDO, it is explicit that the amplitude of the temperature oscillation along the evaporator tube is high, reaches about 60 °C, as shown in **Figure 4.21**. That means that the influence of the PDOs on the surface temperature of the evaporator tube is higher than that of the DWOs.

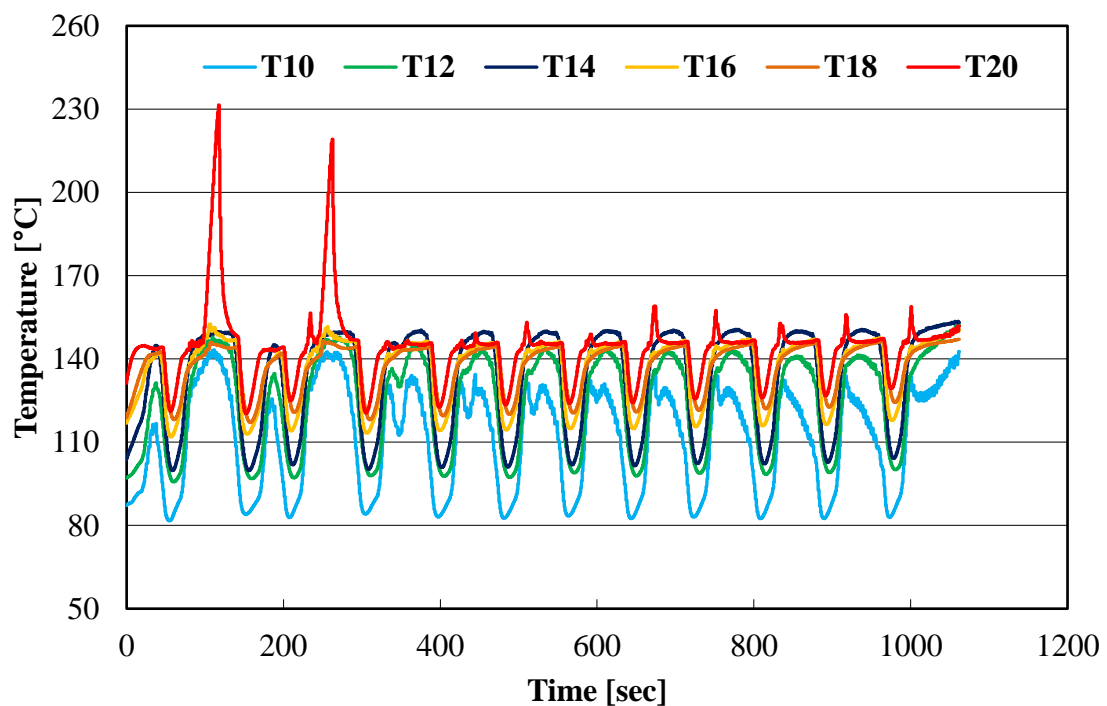


Figure 4.21 The variation of the surface temperature along the evaporator tube during the PDO. This temperature fluctuations with high amplitude leads to reduce the life time of the evaporator tube in the best cases but it also can cause the burnout of the tubes.

Chapter 5: Conclusion and Outlook

In this chapter, conclusions and recommendations resulting from this thesis, categorized by the methodology applied in this thesis, are summarized and an outlook for future research was mentioned.

5.1 Energy and Exergy Analysis

The objective of the energy and exergy analysis was to investigate the performance of an existing 135 MW ISCC power plant in Kuraymat. The plant was thermodynamically studied under Kuraymat climatic conditions. Energy and exergy analyses were performed for the plant as a whole at different ambient temperatures, 5, 20, and 35 °C, and different solar heat inputs, of 0, 50, 75 MW. Moreover, the exergy destruction and the exergetic efficiency for the main components of the ISCC power plant were calculated and investigated regarding the influence of the ambient temperature and the solar heat input to identify the causes and locations of the highest thermodynamic irreversibility. The integration of solar energy into a CCGT power plant was analyzed as a power-boosting mode.

The main conclusions of this study are as follows:

- The thermal output power of the solar field is directly proportional to the DNI.
- The solar field thermal power output decreasing with increasing the incidence angle (θ).
- The solar-to-electricity conversion efficiency of the ISCC solar field was calculated by two methods and it was to be about 16.8% as a solar radiation-to-electricity efficiency and about 41% as a solar thermal-to-electricity efficiency.
- The value of the solar energy-to-electricity conversion efficiency differs according to its definition (solar radiation-to-electricity efficiency or solar thermal-to-electricity efficiency) and it is believed that the first definition is more realistic than the second one as it represents the portion of the solar energy converted to electricity from the whole incident solar energy.
- The solar field has the lowest exergetic efficiency of 17.8% followed by the condenser with 42.2%, at ambient temperature 20 °C and solar heat input 50 MW.
- The exergy destruction in the solar field, 52.9%, is the largest part of the exergy destruction in the ISCC power plant at ambient temperature 20 °C and solar heat input 50 MW.
- The thermal efficiency and the exergetic efficiency of the ISCC decrease with increasing solar field thermal input, where it has its highest values, 51.14% and 49.18%, respectively, during the combined cycle regime and ambient temperature 5 °C.
- The thermal efficiency and the exergetic efficiency of both the ISCC and the combined cycle, at no solar field heat input, decrease with increasing ambient temperature at different solar heat inputs. This is due to the decrease of the exergetic efficiency of the gas turbine, the solar field, the condenser, and the HRSG with increasing ambient temperature.
- The integration of a solar field with a combined cycle reduced the thermal and exergetic efficiencies of the power plant under the combined cycle regime due to the low thermal and

exergetic efficiencies of the solar field because the cost of the solar energy was considered in this study.

Therefore, the target of the ISCC power plants is not to increase the overall thermal efficiency of the combined cycle, but to increase the economic feasibility of solar power plants. Elimination of the thermal storage system reduces the cost of the power plant [82]–[84], CSPPs are generally associated with thermal storage. By contrast, the integration of a solar field with a combined cycle is recommended regarding the given challenges for the electricity market with the continuing expansion of intermittent renewables.

5.2 Dynamic Process Simulation

In the dynamic process simulation study, a sophisticated dynamic process simulation model of the Kuraymat ISCC power plant was developed using APROS simulation software. The model was initialized and tuned using the operational design data from the reference plant. In addition, the main control mechanisms for the drums, control valves, and solar field have been implemented. The dynamic model represents reality with high accuracy and forms a good predictive capability for future dynamic simulations. All components including the solar field, the HRSG and the controlling structures were modelled with the actual specification data from the reference plant. Then, the dynamic simulation was performed for four different days and the simulation results are compared with the actual measurements. The simulation results of the heat absorption by the HTF in the solar field for four days were presented and compared with actual measurements. Then, the FW mass flow rate and the steam mass flow rate, pressure and temperature before the steam turbines were also simulated and compared with their actual measurements. Finally, the electrical power output from the steam turbines and the whole ISCC was calculated and compared with its calculation from the actual measurements for four days. The comparison study showed that the developed model reproduces accurately the most important parameters in the plant (pressure, temperature, mass flow rate, and electrical power output). The developed model was only tuned using the operational design data and no further tuning was considered during the dynamic simulation. The simulation environment was able to depict the behavior of an ISCC power plant very well and can be taken into account in future planning decisions. Finally, it should be mentioned here that the validated dynamic model is of high relevance for the design and operational flexibility of the ISCC power plant to guarantee an affordable and secure supply of electricity. The main conclusions of this study are as follows:

- Investigation of the operational flexibility of ISCC power plants was implemented through developing a detailed dynamic process model for an existing ISCC power plant using APROS software.
- Detailed dynamic validation of the developed model using actual measurements from the reference ISCC power plant was presented.
- For the first time in the literature, providing more confidence in the dynamic simulation for the design and optimization of ISCC power plants by validating the developed model with actual measurements of different four days.
- actual measurements for the ISCC power plants along with the strategy of model build-up and its control circuits was provided to form a cornerstone for future studies in this topic.

5.3 Experimental Investigation of the Two-phase Flow Dynamic Instabilities in the HRSG

In this study, the technical fundamentals of two-phase flow and dynamic instabilities in two-phase flow were briefly clarified. From the literature, there is no experimental study regarding the dynamic instabilities of the two-phase flow in the vertical HRSGs. In this work, the experiments are differentiated from previous research by different parameters, using demineralized water as a test fluid and the direction of the evaporator tube is horizontal. Then, the design of the two-phase test rig that used to perform the experiments in this research is presented.

The two-phase flow dynamic instabilities that may occur in the HRSG were experimentally investigated. The main conclusions of this study are as follows:

- The DWO has high-frequency components compare with the PDO.
- The main component of the DWO was in a frequencies range of about 0.04 to 0.1 Hz.
- The DWO has a period of oscillation that varies from about 10 to 25 sec.
- The main component of the PDO was in between a range of about 0.012 to 0.024 Hz.
- The PDO has a period of oscillation that varies from about 40 to 80 sec.
- The frequency values of the DWOs are higher than these of the PDOs.
- The DWOs occur in the positive slope part of the internal characteristic curve at very low mass flow rates.
- The PDOs occur in the negative slope part of the internal characteristic curve at relatively high mass flow rates compared with the DWOs.
- The thermal oscillations associated with the PDOs have higher amplitudes, reach about 60 °C, unlike those associated with the DWOs.

5.4 Outlook

Energy and Exergy Analysis:

The optimization of the Kuraymat ISCC power plant need to be performed through optimizing:

- The area of the solar field to acquire more DNI and decrease the out of operation hours for the troughs.
- The number of the loops in the solar field, e.g. from 40 to 60 loops.
- The HRSG by replacing it with a supercritical once-through HRSG that has higher operation pressures and temperatures.

Dynamic Process Simulation:

The following suggestions can contribute to a future optimization of the simulation environment:

- Iteratively adjusting of the heat exchangers: the behavior of the simulation was validated using static data. By iteratively adjusting the efficiencies in the heat exchangers, currently existing temperature differences can be improved.
- Improving the control systems: the control mechanisms of an ISCC power plant are very complex. In the simulation environment, the main control mechanisms for the drums, control

valves and solar field have been implemented. These can be further refined to better approximate the experimental data. In addition, it is useful to implement a control for DNI induced control of the solar field area. Through this, the constant solar field outlet temperature can be controlled more precisely.

- Improving the heat losses' mechanism: in the simulation, heat losses through components were assumed to be constant or neglected. By adjusting material properties and activating heat losses, the simulation can be adjusted even closer to reality.

Experimental Investigation of the Two-phase Flow Dynamic Instabilities:

In order to extend the knowledge of the occurrence of two-phase flow instability phenomena in power plants through experimental investigation, more measurement campaigns can be carried out using the existing two-phase flow test rig like changing:

- The mode of operation from forced circulation to natural circulation.
- The orientation of the evaporator tube from a horizontal to a vertical orientation.
- The length to diameter ratio of the evaporator tube.
- The position and the level of the surge tank, which represent the compressible volume in the loop to investigate the PDO.

Appendix A

DWOs and PDOs are obtained two times at the same previous operating conditions.

A.1 The Experimental Results of the Second DWO

The DWO was obtained again at almost the same operating conditions of inlet pressure and temperature of about 3 bar and 60 °C, respectively and heating power of 5000 W. **Figure A.1** shows the histogram of the mass flow rate beside the oscillation of the mass flow rate in the time domain for the second DWO. As shown in this figure, the mass flow rate started to oscillate between 6 kg/h and 12 kg/h with an amplitude of 6 kg/h then continued to oscillate with a higher amplitude of about 10 kg/h.

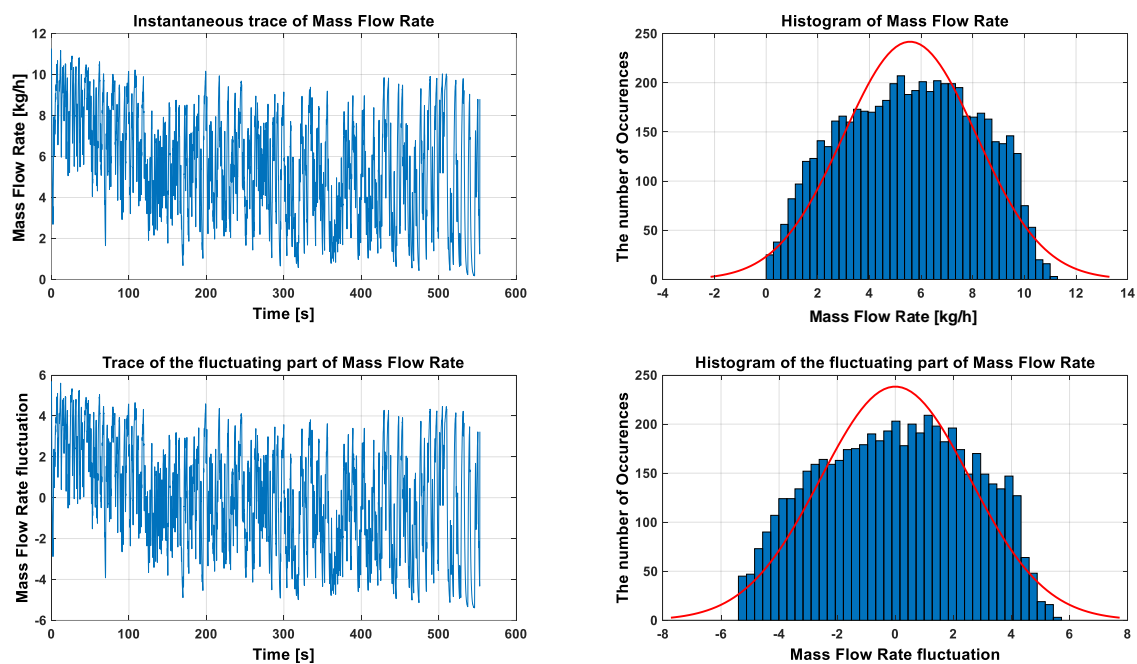


Figure A.1 The variation of the inlet mass flow rate of the evaporator tube during the second DWO

The Fourier spectrum of the mass flow rate oscillations during the second DWO is shown in **Figure A.3**. And the Fourier spectrum of the oscillations of the pressure drop in the evaporator tube during the same DWO was shown in **Figure A.4**. As shown in the **Figure A.3** and **Figure A.4**, the DWOs are compressed in the time domain and expand in the frequency domain which means that the DWO has low-frequency components as shown in the frequency domain chart because there is an inverse relationship between time and frequency domain. That means that the changing rate of the DWO is very high, with frequencies between about 0.035 to 0.088 Hz for the mass flow rate into the evaporator tube and about 0.058 to 0.16 Hz for the pressure drop in the evaporator tube. This means that the main component cycle of the DWO takes from about 6 to 28 sec to repeat itself. These oscillations can be identified as DWO while the surge tank, compressible volume, was not connected during the experiment and the evaporator tube is not very long ($L/D < 150$) [51], [113], [114].

The oscillation of the pressure drop in the evaporator tube during the DWO starts with an amplitude of 100 mbar and then decreases gradually, as shown in **Figure A.2**. The histogram indicated that the pressure drop oscillated most of the time between about 170 and 320 mbar. The main component of the pressure drop fluctuation during the DWO is in the frequencies range of about 0.058 to 0.16 Hz, as shown in **Figure A.4**. This means that its oscillation has a period of about 6.25 to 17 sec.

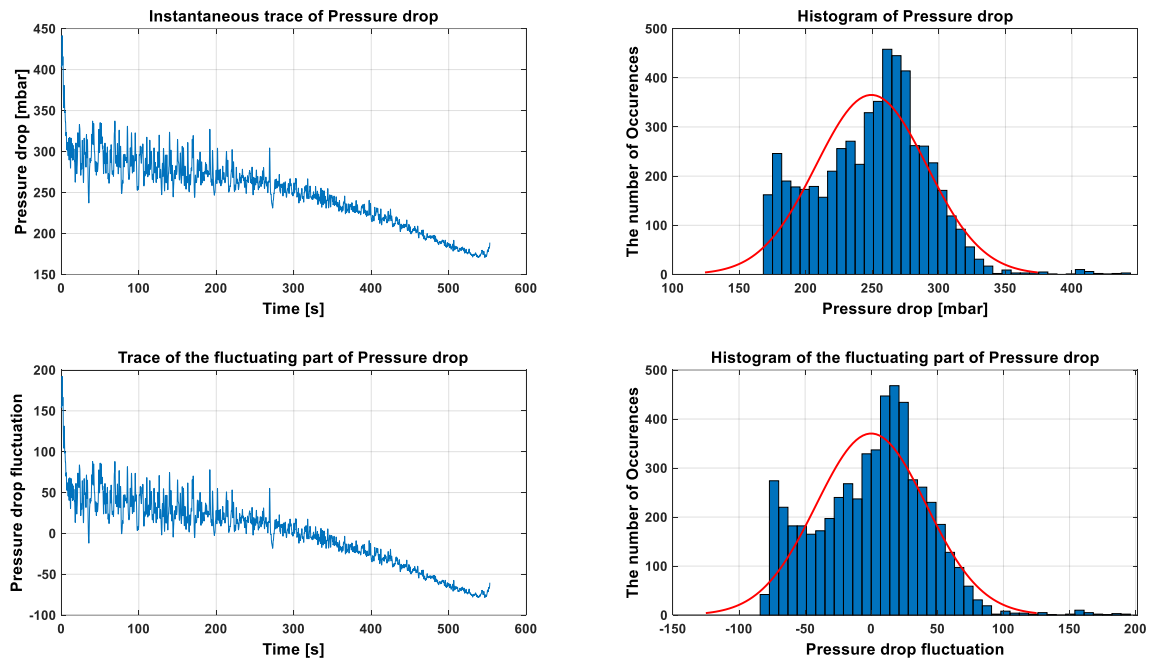


Figure A.2 The variation of the pressure drop in the evaporator tube during the second DWO

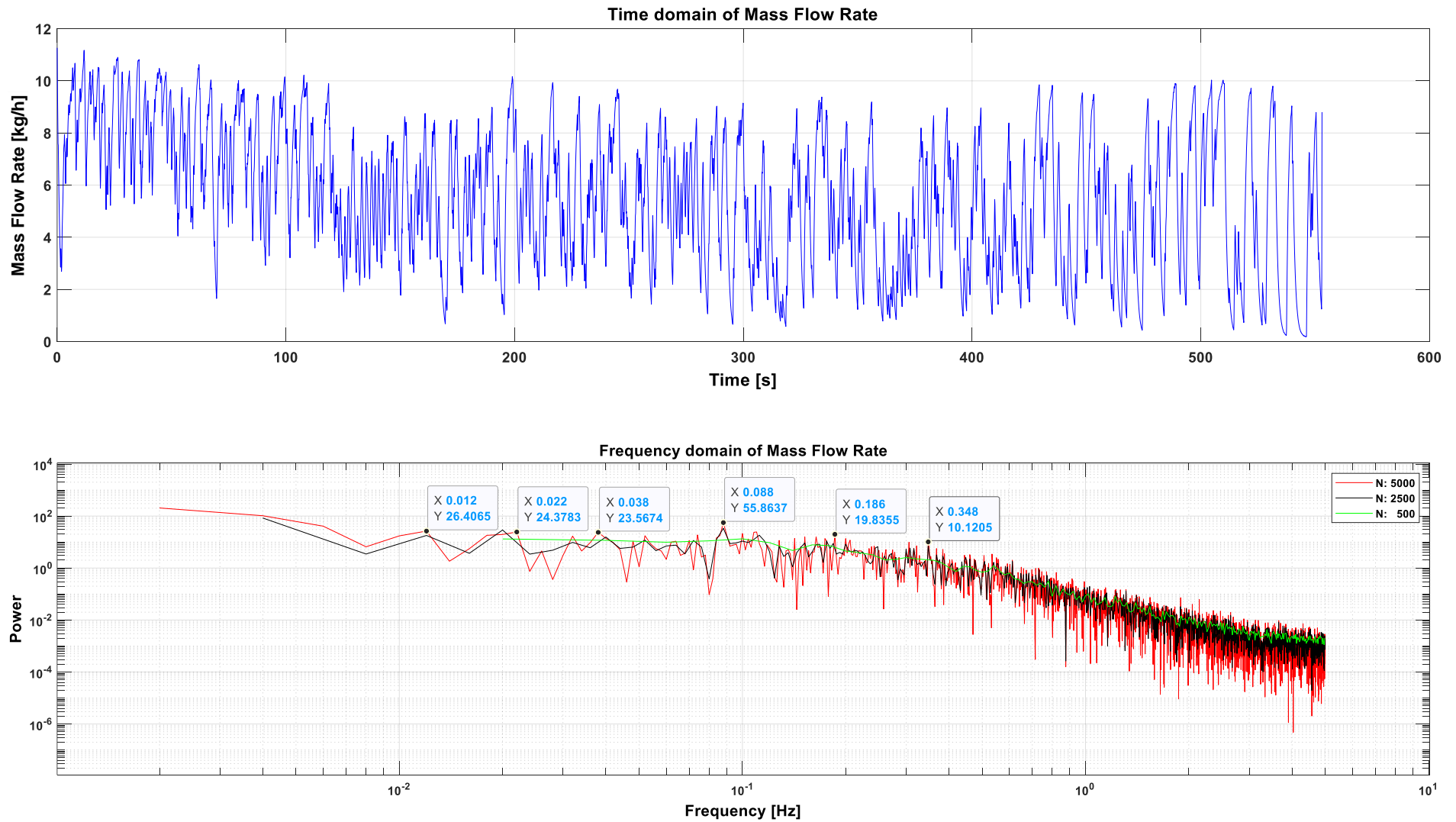


Figure A.3 The variation of the inlet mass flow rate of the evaporator tube during the second DWO in the frequency domain

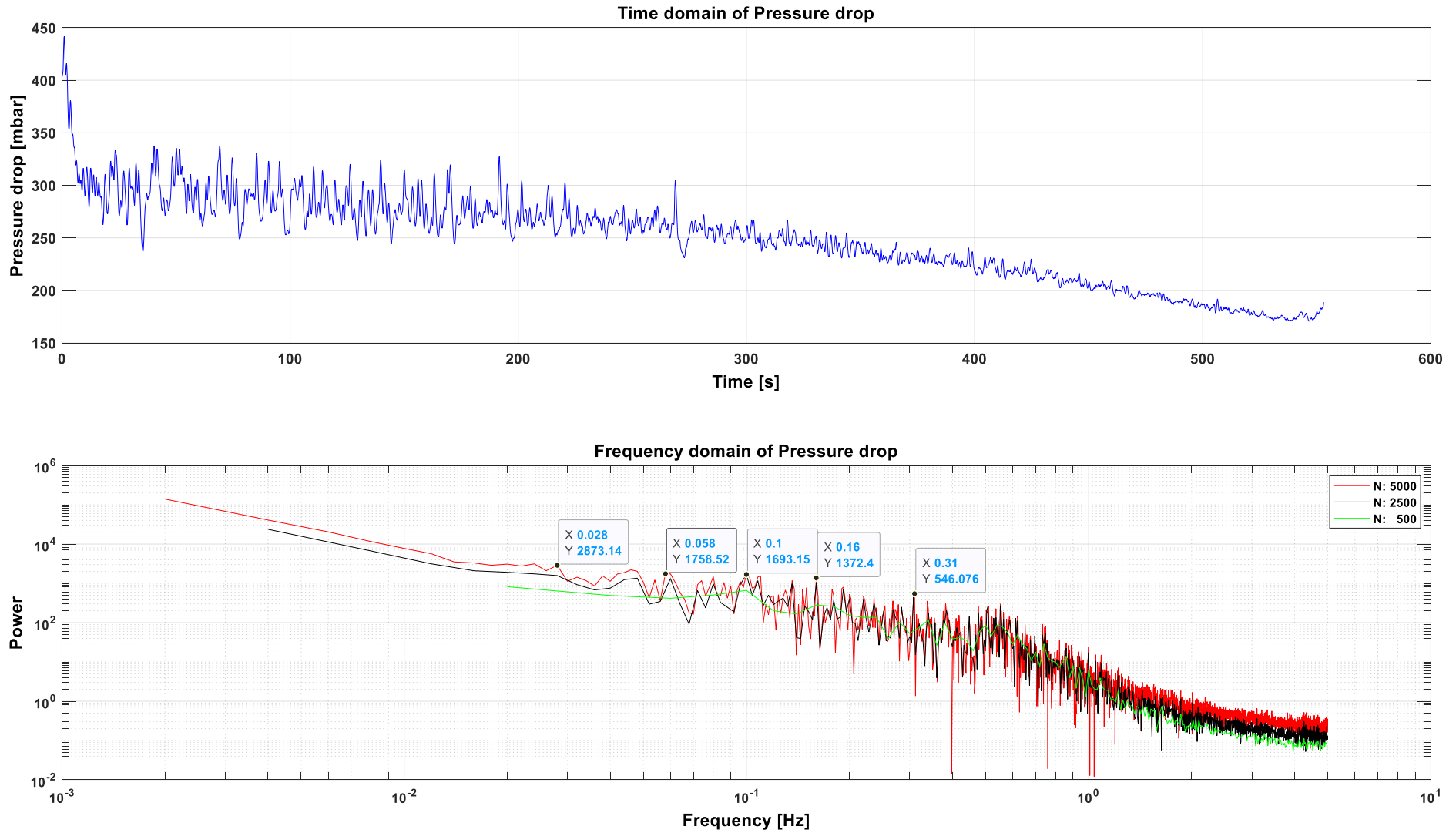


Figure A.4 The variation of the pressure drop in the evaporator tube during the second DWO in the frequency domain

A.2 The Experimental Results of the Second PDO

The PDO was obtained again at almost the same operating conditions of inlet pressure and temperature of about 3 bar and 70 °C, respectively and heating power of 3000 W. The histogram of the pressure drop oscillations that occurred at these conditions is shown in **Figure A.6**. The pressure drop started to oscillate between 10 mbar and 190 mbar with an amplitude of about 180 mbar then it continued to oscillate with a lower amplitude of about 150 mbar. The signal in the time domain indicated that the PDO was slightly interfered with another type of oscillation after the first five minutes, as shown in **Figure A.6** and **Figure A.8**, but from time to time not like the first PDO. This repeated until the oscillation was damped by increasing the mass flow rate to avoid the burnout of the evaporator tube.

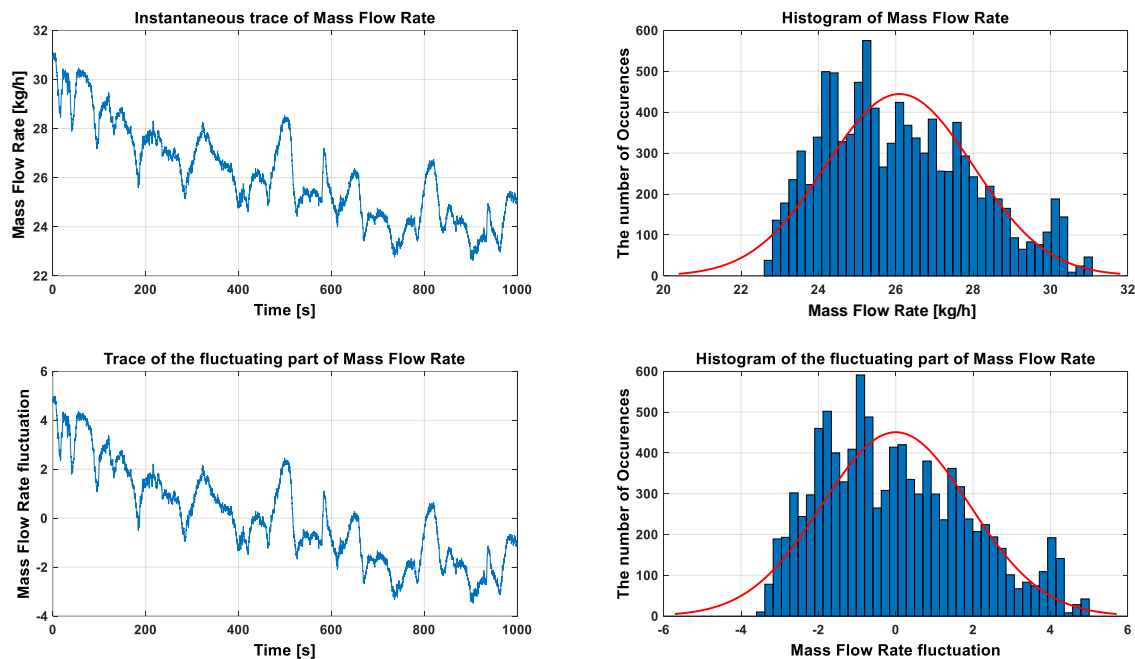


Figure A.5 The variation of the inlet mass flow rate of the evaporator tube during the second PDO

Figure A.5 shows the histogram of the mass flow rate associated with these pressure drop oscillations beside its oscillations in the time domain. As shown in this figure, the mass flow rate started to oscillate between 28 kg/h and 31 kg/h with an amplitude of 3 kg/h then continued to oscillate with a different amplitudes between about of 2 and 4 kg/h. The second PWO was clearly recognized by the fluctuation of the pressure drop in the evaporator tube, unlike the second DWO. The fluctuation of the mass flow rate associated with the second DWO was clearer recognized than the fluctuation of the pressure drop in the evaporator tube.

The onset of the second PDO was based on the zero slope of the internal characteristic curve [51] and these mass flow rate values in addition to the existence of the compressible volume, surge tank, indicate that these oscillations are PDOs. And as mentioned in the literature, the second PDOs occur in the negative slope part of the internal characteristic curve, like the Ledinegg instability [113]. As shown in **Figure A.5** and **Figure A.7**, the system start to oscillate at mass flow rate of about 28 kg/h which was in the negative slope part of the internal characteristic curve of the evaporator tube. Unlike the second DWO which started at a mass flow rate of about 6 kg/h

that located in the positive slope part of the internal characteristic curve of the evaporator tube under investigation.

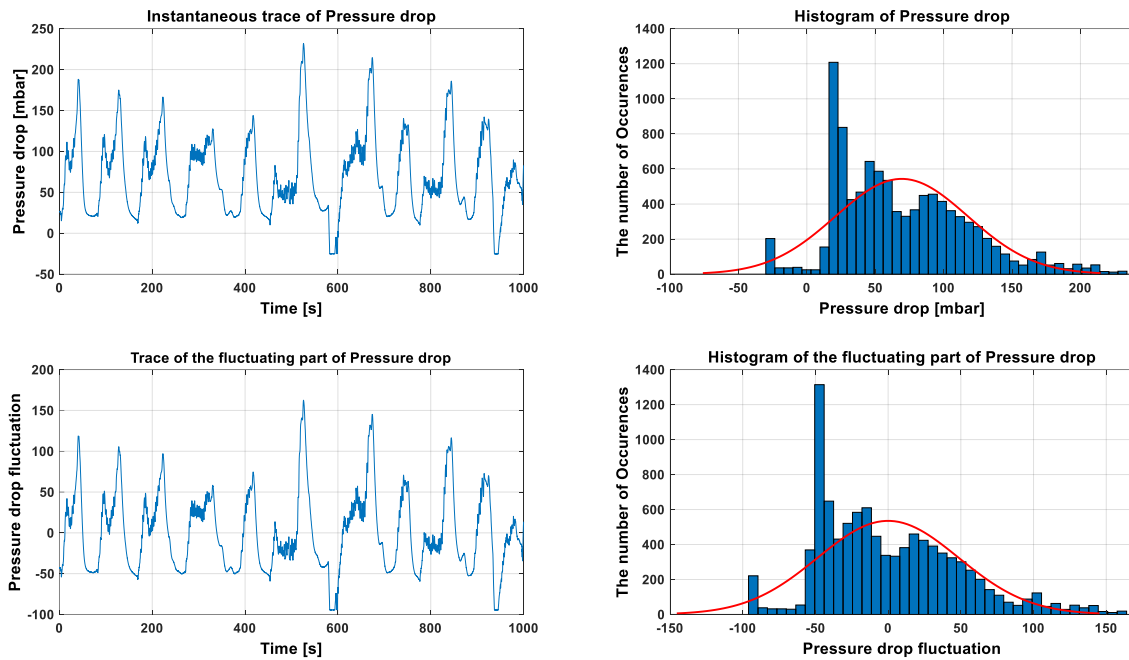


Figure A.6 The variation of the pressure drop in the evaporator tube during the second PDO

In **Figure A.8**, the representation of these pressure drop oscillations in the frequency domain is shown. This figure shows that the frequencies range of these oscillations is between 0.01 and 0.035 Hz. That means that the cycle of the second PWO takes 29 to 100 sec to repeat itself. This is also the same in the representation of the mass flow rate oscillations associated with this PDO in the frequency domain, as shown in **Figure A.7**.

The oscillations of the mass flow rate during this PDO are represented in the frequency domain as shown in **Figure A.7**. The main component of the oscillation signal has a frequency between 0.009 and 0.034 Hz, almost the same frequencies as the pressure drop oscillations. This low frequencies may be due to the existence of a compressible volume in the loop. This slow response due to the existence of the surge tank in the loop, as a compressible volume, allowed the system to adapt with the oscillation and produce a long PDO signal without producing a lot of steam and sharply increase the loop pressure as the case of the DWO.

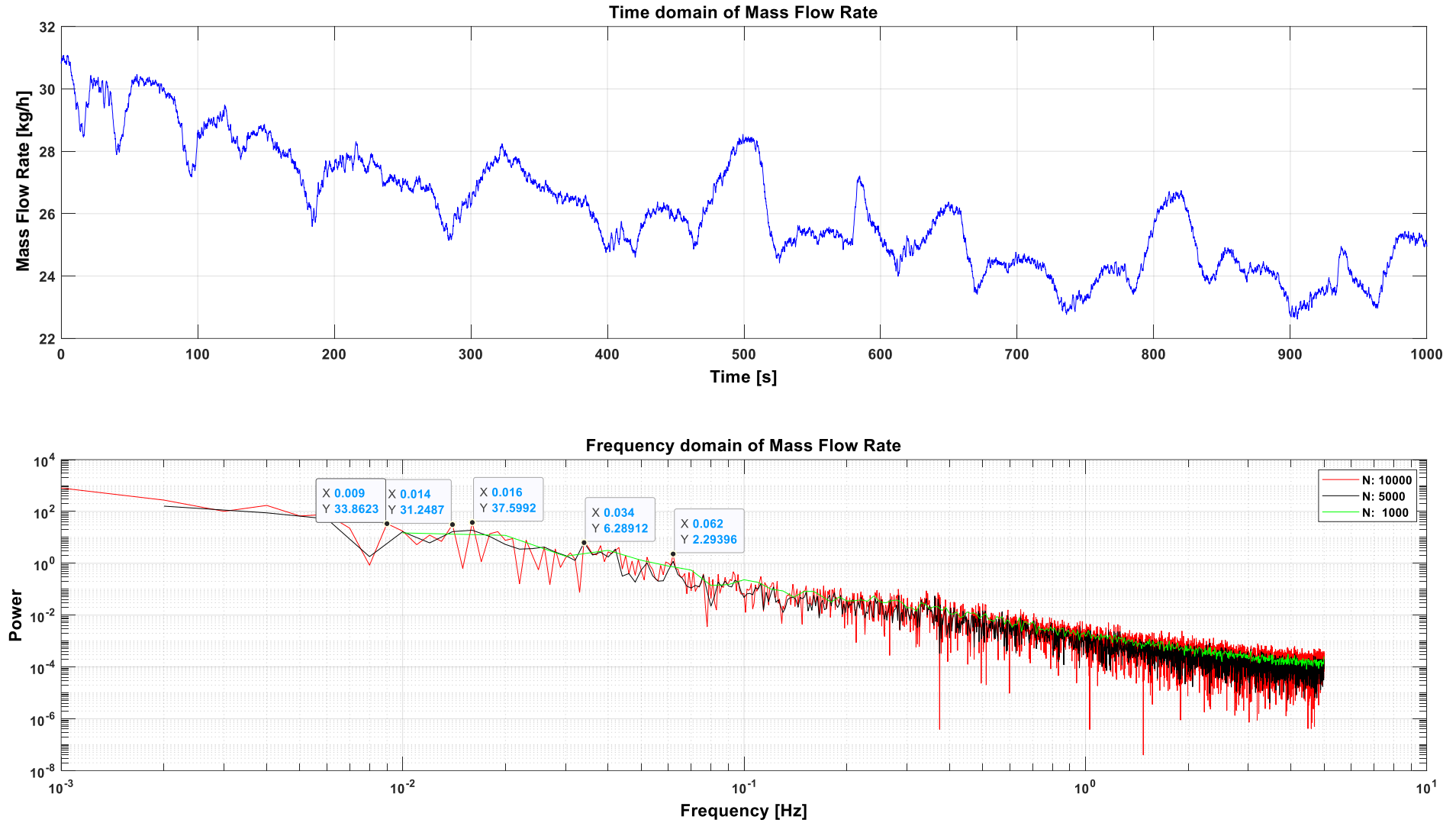


Figure A.7 The variation of the inlet mass flow rate of the evaporator tube during the second PDO in the frequency domain

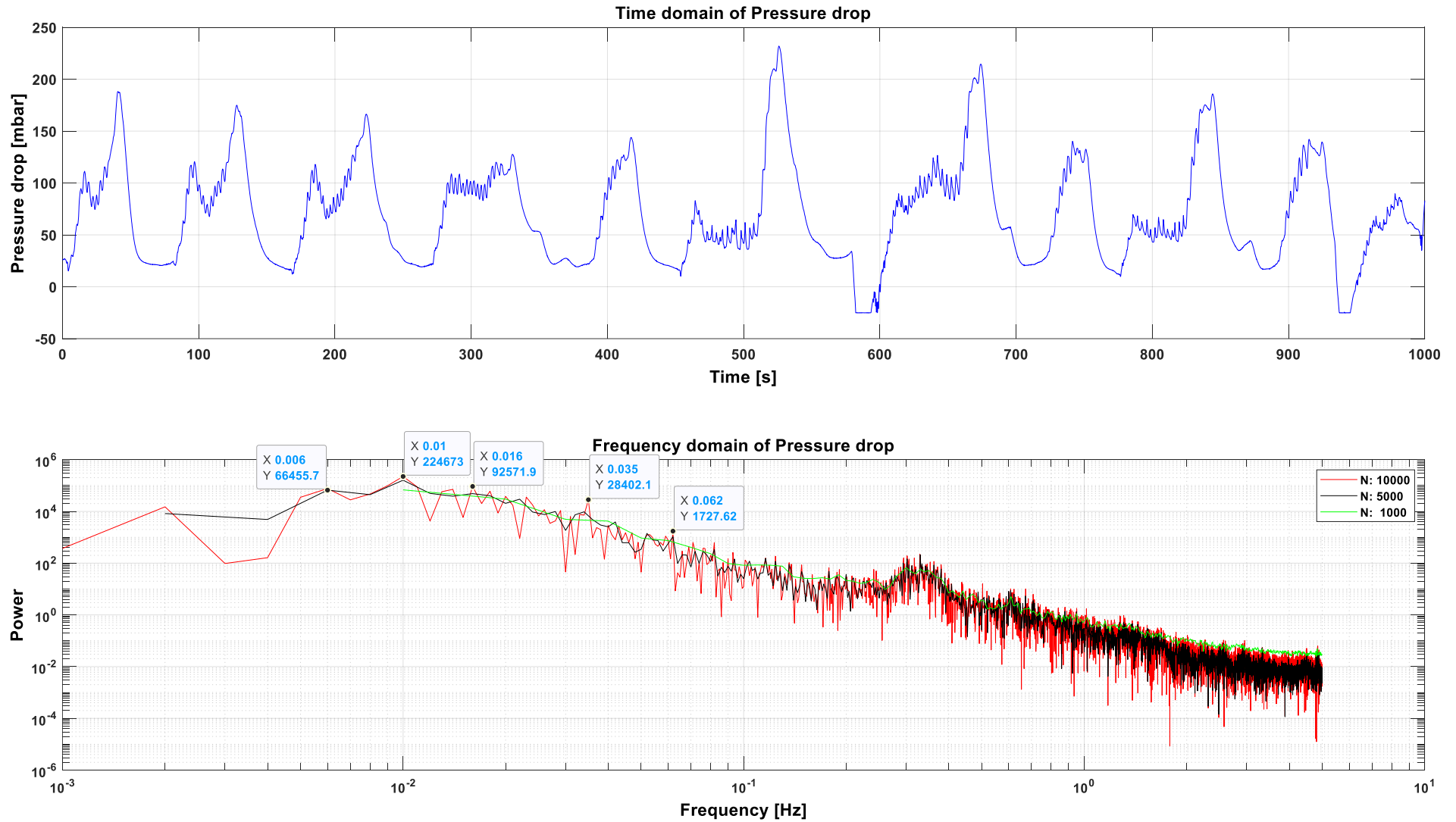


Figure A.8 The variation of the pressure drop in the evaporator tube during the second PDO in the frequency domain

A.3 The Experimental Results of the Second Thermal Oscillation

The thermal oscillations are a consequence of the mass flow rate oscillations that occurred in the evaporator tubes by the reason of the density-wave and pressure-drop oscillations. The evaporator inlet fluid temperature and the heat input are almost constant during the experiment. The mass flow rate fluctuations that occur into the evaporator tube lead to a variable thermal response of the heated wall due to the variable heat transfer coefficient. These variations cause different wall overheating in the tube due to inadequate cooling of the tube wall and that can get coupled with the DWO. This overheating of the tube walls leads to thermal failure, which usually manifests itself in the form of burnout of the wall.

The surface temperature distribution along the evaporator tube during the second DWOs and the second PDOs are shown in **Figure A.9** and **Figure A.10**, respectively, concerning the thermocouples order in **Figure 4.10**. Where twelve thermocouples were installed on the surface of the evaporator tube at six locations, six parts of the evaporator tube, T10 at the beginning of the tube and T20 at the end.

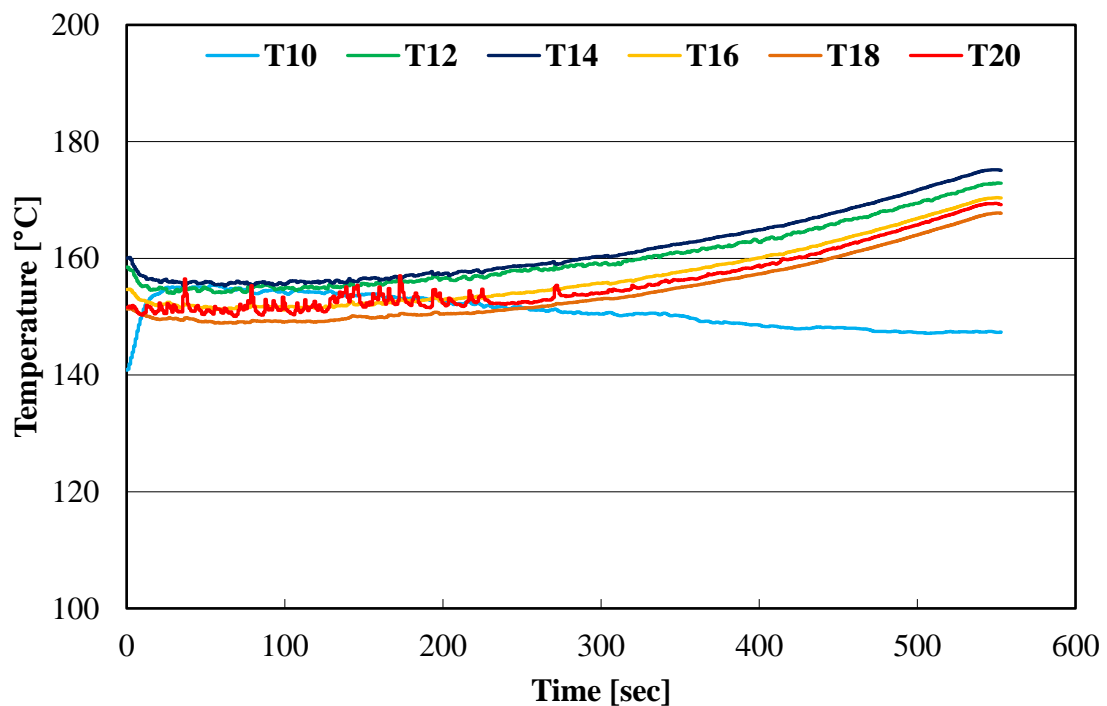


Figure A.9 The variation of the surface temperature along the evaporator tube during the second DWO

As revealed in **Figure A.9**, the evaporation of the water starts at the end of the last third part of the evaporator tube, at T18, because the high heat transfer coefficient of the evaporation decreased the surface temperature than after, at T16.

The thermal oscillations occur as a result of the mass flow rate oscillation due to the previous mentioned dynamic instabilities, DWO and PDO. **Figure A.9** shows the surface temperature oscillation along the evaporator tube associated with the second DWO. The high frequency of the mass flow rate oscillation during the second DWO causes a small amplitude of surface temperature fluctuation.

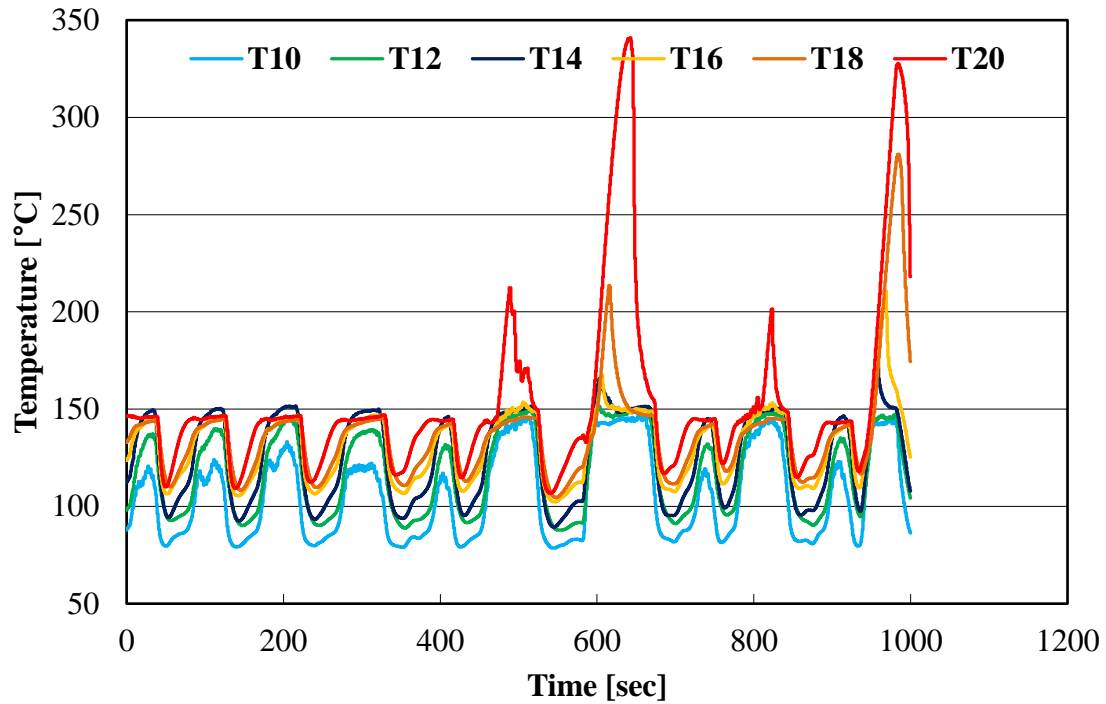


Figure A.10 The variation of the surface temperature along the evaporator tube during the second PDO

In the case of fluctuating the mass flow rate with low frequency, like in the second PDO, it is explicit that the amplitude of the temperature oscillation along the evaporator tube is high, reaches about 60 °C, as shown in **Figure A.10**. That means that the influence of the second PDOs on the surface temperature of the evaporator tube is higher than that of the second DWOs.

Bibliography

- [1] IEA (2020), “Key World Energy Statistics 2020,” OECD Publishing, Paris, 2020. doi: <https://doi.org/https://doi.org/10.1787/295f00f5-en>.
- [2] European Commission, “Climate Action - Building a world we like, with a climate we like,” 2014. doi: 10.2775/83031.
- [3] UNFCCC, “Adoption of the Paris Agreement,” Paris, 2015.
- [4] H. L. Zhang *et al.*, “Concentrated solar power plants: Review and design methodology,” *Renew. Sustain. Energy Rev.*, vol. 22, pp. 466–481, Jun. 2013, doi: 10.1016/j.rser.2013.01.032.
- [5] D. Mills, “Advances in solar thermal electricity technology,” *Sol. Energy*, vol. 76, no. 1–3, pp. 19–31, 2004, doi: 10.1016/S0038-092X(03)00102-6.
- [6] O. Behar, A. Khellaf, K. Mohammedi, and S. Ait-kaci, “A review of integrated solar combined cycle system (ISCCS) with a parabolic trough technology,” *Renew. Sustain. Energy Rev.*, vol. 39, pp. 223–250, Nov. 2014, doi: 10.1016/j.rser.2014.07.066.
- [7] A. Rovira, M. J. Montes, F. Varela, and M. Gil, “Comparison of Heat Transfer Fluid and Direct Steam Generation technologies for Integrated Solar Combined Cycles,” *Appl. Therm. Eng.*, vol. 52, no. 2, pp. 264–274, 2013, doi: 10.1016/j.applthermaleng.2012.12.008.
- [8] J. Dersch *et al.*, “Trough integration into power plants—a study on the performance and economy of integrated solar combined cycle systems,” *Energy*, vol. 29, no. 5–6, pp. 947–959, Apr. 2004, doi: 10.1016/s0360-5442(03)00199-3.
- [9] J. Mariyappan and D. Anderson, “Thematic Review of GEF-Financed Solar Thermal Projects,” 2001.
- [10] The World Bank, “Implementation Completion and Results Report (TF-91289) on A Grand in The Amount of US\$ 49.80 Million to the Arab Republic of Egypt for the Kureimat Solar Thermal Hybrid Project,” 2012.
- [11] S. Heide *et al.*, “Design and operational aspects of gas and steam turbines for the novel solar hybrid combined cycle SHCC®,” in *ASME Turbo Expo 2010: Power for Land, Sea, and Air*, 2010, pp. 465–474.
- [12] M. A. H. El-Sayed, “Solar supported steam production for power generation in Egypt,” *Energy Policy*, vol. 33, no. 10, pp. 1251–1259, Jul. 2005, doi: 10.1016/j.enpol.2003.11.021.
- [13] O. Behar, A. Kellaf, K. Mohamedi, and M. Belhamel, “Instantaneous performance of the first Integrated Solar Combined Cycle System in Algeria,” *Energy Procedia*, vol. 6, pp. 185–193, 2011, doi: 10.1016/j.egypro.2011.05.022.
- [14] E. Pihl, J. Spelling, and F. Johnsson, “Thermo-Economic Optimization of Hybridization Options for Solar Retrofitting of Combined-Cycle Power Plants,” *J. Sol. Energy Eng.*, vol. 136, no. 2, pp. 1–9, May 2013, doi: 10.1115/1.4024922.
- [15] B. Kelly, U. Herrmann, and M. J. Hale, “Optimization studies for integrated solar combined cycle systems,” in *Proceedings of Solar Forum 2001 Solar Energy: The Power to Choose*, 2001, no. April, pp. 393–398.
- [16] M. Horn, H. Führung, and J. Rheinländer, “Economic analysis of integrated solar combined cycle power plants,” *Energy*, vol. 29, no. 5–6, pp. 935–945, Apr. 2004, doi: doi:

- 10.1016/s0360-5442(03)00198-1.
- [17] A. M. Patnode, "Simulation and performance evaluation of parabolic trough solar power plants," WISCONSIN-MADISON, 2006.
- [18] Y. USTA, "Simulations of A Large Scale Solar Thermal Power Plant in Turkey Using Concentrating Parabolic Trough Collectors," Middle East Technical University, 2010.
- [19] G. C. Bakos and D. Parsa, "Technoeconomic assessment of an integrated solar combined cycle power plant in Greece using line-focus parabolic trough collectors," *Renew. Energy*, vol. 60, pp. 598–603, Dec. 2013, doi: 10.1016/j.renene.2013.05.025.
- [20] H. Derbal-Mokrane, S. Bouaichaoui, N. E. Gharbi, M. Belhamel, and A. Benzaoui, "Modeling and numerical simulation of an Integrated Solar Combined Cycle System in Algeria," *Procedia Eng.*, vol. 33, no. 20112, pp. 199–208, 2012, doi: 10.1016/j.proeng.2012.01.1194.
- [21] A. Baghernejad and M. Yaghoubi, "Exergoeconomic analysis and optimization of an Integrated Solar Combined Cycle System (ISCCS) using genetic algorithm," *Energy Convers. Manag.*, vol. 52, no. 5, pp. 2193–2203, May 2011, doi: 10.1016/j.enconman.2010.12.019.
- [22] M. J. Montes *et al.*, "Performance analysis of an Integrated Solar Combined Cycle using Direct Steam Generation in parabolic trough collectors," *Appl. Energy*, vol. 88, no. 9, pp. 3228–3238, Sep. 2011, doi: 10.1016/j.apenergy.2011.03.038.
- [23] G. Bonforte, J. Buchgeister, G. Manfrida, and K. Petela, "Exergoeconomic and exergoenvironmental analysis of an integrated solar gas turbine/combined cycle power plant," *Energy*, vol. 156, pp. 352–359, Aug. 2018, doi: 10.1016/j.energy.2018.05.080.
- [24] P. Iora, G. P. Beretta, and A. F. Ghoniem, "Exergy loss based allocation method for hybrid renewable-fossil power plants applied to an integrated solar combined cycle," *Energy*, vol. 173, pp. 893–901, Apr. 2019, doi: 10.1016/j.energy.2019.02.095.
- [25] M. Mehrpooya, E. Tosang, and A. Dadak, "Investigation of a combined cycle power plant coupled with a parabolic trough solar field and high temperature energy storage system," *Energy Convers. Manag.*, vol. 171, pp. 1662–1674, Sep. 2018, doi: 10.1016/j.enconman.2018.07.001.
- [26] A. Baghernejad and M. Yaghoubi, "Exergy analysis of an integrated solar combined cycle system," *Renew. Energy*, vol. 35, no. 10, pp. 2157–2164, Oct. 2010, doi: 10.1016/j.renene.2010.02.021.
- [27] S. Wang, Z. Fu, G. Zhang, and T. Zhang, "Advanced Thermodynamic Analysis Applied to an Integrated Solar Combined Cycle System," *Energies*, vol. 11, no. 6, p. 1574, Jun. 2018, doi: 10.3390/en11061574.
- [28] L. Duan and Z. Wang, "Performance study of a novel integrated solar combined cycle system," *Energies*, vol. 11, no. 12, p. 3400, Dec. 2018, doi: 10.3390/en1123400.
- [29] S. Wang and Z. Fu, "Thermodynamic investigation of an integrated solar combined cycle with an ORC system," *Entropy*, vol. 21, no. 4, p. 428, Apr. 2019, doi: 10.3390/e21040428.
- [30] D. Liqiang, L. Zhipeng, and W. Zhen, "Study on a new solar thermal energy complementary power generation system based on gas-steam combined cycle," in *American Society of Mechanical Engineers, Power Division (Publication) POWER*, Dec. 2019, vol. 2019-July, doi: 10.1115/POWER2019-1814.
- [31] G. Wang, S. Wang, J. Lin, and Z. Chen, "Exergic Analysis of an ISCC System for Power Generation and Refrigeration," *Int. J. Thermophys.*, 2021, doi: 10.1007/s10765-021-02852-

- 7.
- [32] J. Spelling, D. Favrat, A. Martin, and G. Augsburger, “Thermoeconomic optimization of a combined-cycle solar tower power plant,” *Energy*, vol. 41, no. 1, pp. 113–120, May 2012, doi: 10.1016/j.energy.2011.03.073.
- [33] G. Franchini, A. Perdichizzi, S. Ravelli, and G. Barigozzi, “A comparative study between parabolic trough and solar tower technologies in Solar Rankine Cycle and Integrated Solar Combined Cycle plants,” *Sol. Energy*, vol. 98, pp. 302–314, Dec. 2013, doi: 10.1016/j.solener.2013.09.033.
- [34] C. V. Ponce *et al.*, “Dynamic simulator and model predictive control of an integrated solar combined cycle plant,” *Energy*, vol. 109, pp. 974–986, Aug. 2016, doi: 10.1016/j.energy.2016.04.129.
- [35] E.F. Camacho, M. Berenguel, and F.R. Rubio, *Advanced Control of Solar Plants*. London: Springer, 1997.
- [36] D. Sáez, A. Cipriano, and A. W. Ordys, *Optimisation of Industrial Processes at Supervisory Level*, 1st ed. London: Springer London, 2002.
- [37] F. Calise, M. D. D’Accadia, L. Libertini, and M. Vicidomini, “Thermoeconomic analysis of an integrated solar combined cycle power plant,” *Energy Convers. Manag.*, vol. 171, pp. 1038–1051, 2018, doi: 10.1016/j.enconman.2018.06.005.
- [38] B. El Hefni, “Dynamic modeling of a hybrid solar-combined cycle power plant (ISCC) using a solar field based on parabolic trough solar collector - Start-up and shutdown of the solar field,” in *AIP Conference Proceedings*, Nov. 2018, vol. 2033, doi: 10.1063/1.5067177.
- [39] K. Rashid, S. M. Safdarnejad, K. Ellingwood, and K. M. Powell, “Techno-economic evaluation of different hybridization schemes for a solar thermal/gas power plant,” *Energy*, vol. 181, pp. 91–106, Aug. 2019, doi: 10.1016/j.energy.2019.05.130.
- [40] L. Duan, Z. Wang, and Y. Guo, “Off-design performance characteristics study on ISCC system with solar direct steam generation system,” *Energy*, vol. 205, p. 118044, Aug. 2020, doi: 10.1016/j.energy.2020.118044.
- [41] Z. Wang and L. Duan, “Study on integrated solar combined cycle system with a new operation strategy of changeable integration mode under different Direct Normal Irradiance (DNI) conditions,” *Energy Sci. Eng.*, vol. 8, no. 8, pp. 2907–2921, May 2020, doi: 10.1002/ese3.711.
- [42] N. Abdelhafidi, İ. H. Yılmaz, and N. E. I. Bachari, “An innovative dynamic model for an integrated solar combined cycle power plant under off-design conditions,” *Energy Convers. Manag.*, vol. 220, p. 113066, Sep. 2020, doi: 10.1016/j.enconman.2020.113066.
- [43] N. Zhang *et al.*, “Operation strategy and dynamic performance study of integrated solar combined-cycle system,” *Energy Convers. Manag.*, p. 113716, Dec. 2020, doi: 10.1016/j.enconman.2020.113716.
- [44] M. Kaichiro, N. Hiedeaki, and M. Itaru, “Boiling burnout and flow instabilities for water flowing in a round tube under atmospheric pressure,” *Int. J. Heat Mass Transf.*, vol. 28, no. 6, pp. 1115–1129, 1985, doi: 10.1016/0017-9310(85)90120-6.
- [45] Q. Wang, X. J. J. Chen, S. Kakaç, and Y. Ding, “An experimental investigation of density-wave-type oscillations in a convective boiling upflow system,” *Int. J. Heat Fluid Flow*, vol. 15, no. 3, pp. 241–246, Jun. 1994, doi: 10.1016/0142-727X(94)90044-2.

- [46] K. C. Jain, M. Petrick, D. Miller, and S. G. Bankoff, "Self-sustained hydrodynamic oscillations in a natural-circulation boiling water loop," *Nucl. Eng. Des.*, vol. 4, no. 3, pp. 233–252, 1966, doi: 10.1016/0029-5493(66)90049-5.
- [47] D. Delmastro and A. Clausse, "Experimental phase trajectories in boiling flow oscillations," *Exp. Therm. Fluid Sci.*, vol. 9, no. 1, pp. 47–52, 1994, doi: 10.1016/0894-1777(94)90007-8.
- [48] J. M. Kim and S. Y. Lee, "Experimental observation of flow instability in a semi-closed two-phase natural circulation loop," *Nucl. Eng. Des.*, vol. 196, no. 3, pp. 359–367, 2000, doi: 10.1016/S0029-5493(99)00296-4.
- [49] S. Guanghui, J. Dounan, K. Fukuda, and G. Yujun, "Theoretical and experimental study on density wave oscillation of two-phase natural circulation of low equilibrium quality," *Nucl. Eng. Des.*, vol. 215, no. 3, pp. 187–198, Jun. 2002, doi: 10.1016/S0029-5493(01)00456-3.
- [50] A. Baars and A. Delgado, "Multiple modes of a natural circulation evaporator," *Int. J. Heat Mass Transf.*, vol. 49, no. 13–14, pp. 2304–2314, Jul. 2006, doi: 10.1016/j.ijheatmasstransfer.2005.10.046.
- [51] J. S. Maulbetsch and P. Griffith, "A Study of System-Induced Instabilities in Forced-Convection Flows with Subcooled Boiling," Cambridge, 1965.
- [52] S. Karsli, M. Yilmaz, and O. Comakli, "The effect of internal surface modification on flow instabilities in forced convection boiling in a horizontal tube," *Int. J. Heat Fluid Flow*, vol. 23, no. 6, pp. 776–791, Dec. 2002, doi: 10.1016/S0142-727X(02)00147-9.
- [53] H. Yüncü, "An experimental and theoretical study of density wave and pressure drop oscillations," *Heat Transf. Eng.*, vol. 11, no. 3, pp. 45–56, 1990, doi: 10.1080/01457639008939734.
- [54] Ö. Çomaklı, S. Karşlı, and M. Yılmaz, "Experimental investigation of two-phase flow instabilities in a horizontal in-tube boiling system," *Energy Convers. Manag.*, vol. 43, no. 2, pp. 249–268, Jan. 2002, doi: 10.1016/S0196-8904(01)00021-8.
- [55] S. Kakaç and L. Cao, "Analysis of convective two-phase flow instabilities in vertical and horizontal in-tube boiling systems," *Int. J. Heat Mass Transf.*, vol. 52, no. 17–18, pp. 3984–3993, Aug. 2009, doi: 10.1016/j.ijheatmasstransfer.2009.03.025.
- [56] N. Liang, S. Shuangquan, C. Tian, and Y. Y. Yan, "Two-phase flow instabilities in horizontal straight tube evaporator," *Appl. Therm. Eng.*, vol. 31, no. 2–3, pp. 181–187, Feb. 2011, doi: 10.1016/J.APPLTHERMALENG.2010.08.029.
- [57] C. A. Dorao, "Effect of inlet pressure and temperature on density wave oscillations in a horizontal channel," *Chem. Eng. Sci.*, vol. 134, pp. 767–773, Sep. 2015, doi: 10.1016/J.CES.2015.03.040.
- [58] M. Sørum and C. A. Dorao, "Experimental study of the heat transfer coefficient deterioration during density wave oscillations," *Chem. Eng. Sci.*, vol. 132, pp. 178–185, Aug. 2015, doi: 10.1016/j.ces.2015.03.039.
- [59] L. Zhang, Y. Wang, and Z. Yu, "Experimental study of flow boiling instabilities in horizontal tubes under gas-liquid stratification condition: Effects of heat flux and inlet subcooling degree," *Int. J. Heat Mass Transf.*, vol. 118, pp. 1040–1045, Mar. 2018, doi: 10.1016/j.ijheatmasstransfer.2017.11.032.
- [60] I. W. Park, M. Fernandino, and C. A. Dorao, "Experimental study on the characteristics of pressure drop oscillations and their interaction with short-period oscillation in a horizontal tube," *Int. J. Refrig.*, vol. 91, pp. 246–253, Jul. 2018, doi: 10.1016/j.ijrefrig.2018.05.008.

- [61] L. Zhang, Y. Wang, and Z. Yu, "Regulation of gas-liquid stratified flow boiling dynamic instabilities in horizontal tube: Effects of heat load distribution and wall thermal capacity," *Int. J. Heat Mass Transf.*, vol. 127, pp. 426–436, Dec. 2018, doi: 10.1016/j.ijheatmasstransfer.2018.07.083.
- [62] I. W. Park, M. Fernandino, and C. A. Dorao, "On the occurrence of superimposed density wave oscillations on pressure drop oscillations and the influence of a compressible volume," *AIP Adv.*, vol. 8, no. 7, Jul. 2018, doi: 10.1063/1.5040113.
- [63] NREA, "New & Renewable Energy Authority (NREA): Annual Report 2008/2009. Arab Republic of Egypt: Ministry of Electricity & Energy," 2010.
- [64] Inger Anderson, C. D. A. D. Craig, J. A. Kamal, P. Veevers-Carter, C. Govindarajalu, and F. Hassan, "Report No : ICR2173 Implementation Completion and Results Report on a Grant In The Amount of Us\$ 49.80 Million to the Arab Republic of Egypt for the Kureimat Solar Thermal Hybrid Project," 2012.
- [65] G. Brakmann, F. A. Mohammad, M. Dolejsi, and M. Wiemann, "Construction of the ISCC Kuraymat," in *International SolarPACES Conference*, 2009, no. 5, pp. 15–18.
- [66] A. Temraz, A. Rashad, A. Elweteedy, F. Alobaid, and B. Epple, "Energy and Exergy Analyses of an Existing Solar-Assisted Combined Cycle Power Plant," *Appl. Sci.*, vol. 10, no. 14, p. 4980, Jul. 2020, doi: 10.3390/app10144980.
- [67] A. Temraz, A. Rashad, A. Elweteedy, and K. Elshazly, "Thermal Analysis of the ISCC Power Plant in Kuraymat, Egypt," in *18th International Conference on Applied Mechanics and Mechanical Engineering (AMME 18)*, 2018, vol. 18, no. 18, pp. 3–5, doi: 10.21608/AMME.2018.34995.
- [68] A. Rashad, A. Elweteedy, A. Temraz, and A. Gomaa, "Investigating an Integrated Solar Combined Cycle Power Plant," *Glob. J. Eng. Sci. - GJES*, vol. 7, no. 1, pp. 1–14, 2021, doi: 10.33552/GJES.2021.07.000652.
- [69] S. D. Sheet, "Therminol 66 Heat Transfer Fluid 54578-28-8," in *Sax's Dangerous Properties of Industrial Materials*, 2012, pp. 1–13.
- [70] Eastman, "Selection Guide High-performance fluids for precise temperature control." p. 10.
- [71] FLAGOL GMBH, "Solar Field Assembly Line - SKAL-ET Collector," 2007.
- [72] V. Siva Reddy, S. C. Kaushik, K. R. Ranjan, and S. K. Tyagi, "State-of-the-art of solar thermal power plants—A review," *Renew. Sustain. Energy Rev.*, vol. 27, pp. 258–273, Nov. 2013, doi: 10.1016/j.rser.2013.06.037.
- [73] "Operating Instructions for HTF System and Solar Field, ISCC KURAYMAT Operation Manual," 2013.
- [74] Eastman Chemical Company, "Technical data sheet Therminol® VP1 Heat Transfer Fluid," vol. 123, no. May. Eastman Chemical Company, pp. 98–99, 2021.
- [75] J. Ramachandran and M. C. Conway, "MS6001FA – An Advanced-Technology 70-MW Class 50/60 Hz Gas Turbine," *Tech. Doc. GER-3765B GE Power Syst. Schenectady, NY*, p. 14, 1996.
- [76] J. A. Duffie and W. A. Beckman, *Solar Engineering of Thermal Processes: Fourth Edition*. 2013.
- [77] T. A. Stuetzle, "Automatic Control of the 30MWe SEGS VI Parabolic Trough Plant," University of Wisconsin – Madison, 2002.

- [78] R. Forristall, "Heat Transfer Analysis and Modeling of a Parabolic Trough Solar Receiver Implemented in Engineering Equation Solver," 2003. doi: NREL/TP-550-34169.
- [79] G. Manente, S. Rech, and A. Lazzaretto, "Optimum choice and placement of concentrating solar power technologies in integrated solar combined cycle systems," *Renew. Energy*, vol. 96, pp. 172–189, Oct. 2016.
- [80] T. J. Kotas, *The Exergy Method of Thermal Plant Analysis*, 1st ed. London, UK: Anchor Brendon Ltd, Tiptree, Essex, 1985.
- [81] A. Temraz, A. Rashad, A. Alweteedy, and K. Elshazly, "Seasonal Performance Evaluation of ISCCS Solar Field in Kureimat, Egypt," in *6th Annual International Conference on Sustainable Energy and Environmental Sciences (SEES 2017)*, Mar. 2017, no. March, pp. 91–98, doi: 10.5176/2251-189X_SEES17.38.
- [82] G. Zhu, T. Neises, C. Turchi, and R. Bedilion, "Thermodynamic evaluation of solar integration into a natural gas combined cycle power plant," *Renew. Energy*, vol. 74, pp. 815–824, Feb. 2015, doi: 10.1016/j.renene.2014.08.073.
- [83] A. E. Elmohlawy, V. F. Ochkov, and B. I. Kazandzhan, "Thermal performance analysis of a concentrated solar power system (CSP) integrated with natural gas combined cycle (NGCC) power plant," *Case Stud. Therm. Eng.*, vol. 14, no. February, p. 100458, 2019, doi: 10.1016/j.csite.2019.100458.
- [84] A. Rovira, R. Abbas, C. Sánchez, and M. Muñoz, "Proposal and analysis of an integrated solar combined cycle with partial recuperation," *Energy*, vol. 198, p. 117379, May 2020, doi: 10.1016/j.energy.2020.117379.
- [85] R. V. Padilla, A. Fontalvo, G. Demirkaya, A. Martinez, and A. G. Quiroga, "Exergy analysis of parabolic trough solar receiver," *Appl. Therm. Eng.*, vol. 67, no. 1–2, pp. 579–586, Jun. 2014, doi: 10.1016/j.applthermaleng.2014.03.053.
- [86] W. R. DUNBAR and N. LIOR, "Sources of Combustion Irreversibility," *combust. Sci. Tech.*, vol. 103, pp. 41–61, 1994.
- [87] H. Athari, S. Soltani, M. A. Rosen, S. M. Seyed Mahmoudi, and T. Morosuk, "Comparative exergoeconomic analyses of gas turbine steam injection cycles with and without fogging inlet cooling," *Sustain.*, vol. 7, no. 9, pp. 12236–12257, 2015, doi: 10.3390/su70912236.
- [88] M. Anheden, "Analysis of gas turbine systems for sustainable energy conversion," Royal Institute of Technology, 2000.
- [89] R. L. Cornelissen and G. G. Hirs, "Exergetic optimisation of a heat exchanger," *Energy Convers. Manag.*, vol. 38, no. 15–17, pp. 1567–1576, 1997, doi: 10.1016/S0196-8904(96)00218-X.
- [90] S. D. Pandey and V. K. Nema, "An experimental investigation of exergy loss reduction in corrugated plate heat exchanger," *Energy*, vol. 36, no. 5, pp. 2997–3001, 2011, doi: 10.1016/j.energy.2011.02.043.
- [91] C. Dodson, A. Razani, and T. Roberts, "A Model for Exergy Efficiency and Analysis of Regenerators," in *Cryocoolers 15*, 2009, vol. 15, no. 1, pp. 353–361.
- [92] I. Paniagua, J. Martín, C. Fernandez, Á. Alvaro, and R. Carlier, "A New Simple Method for Estimating Exergy Destruction in Heat Exchangers," *Entropy*, vol. 15, no. 2, pp. 474–489, 2013, doi: 10.3390/e15020474.
- [93] A. GALOVIĆ, M. ŽIVIĆ, and M. KOKANOVIĆ, "Analysis of Exergy Destruction of an Evaporator or/and a Condenser," *Strojarstvo*, vol. 51, no. 1, pp. 73–78, 2009.

- [94] F. Alobaid, N. Mertens, R. Starkloff, T. Lanz, C. Heinze, and B. Epple, "Progress in dynamic simulation of thermal power plants," *Prog. Energy Combust. Sci.*, vol. 59, pp. 79–162, 2017, doi: 10.1016/j.pecs.2016.11.001.
- [95] F. Alobaid *et al.*, "Modeling and investigation start-up procedures of a combined cycle power plant," *Appl. Energy*, vol. 85, no. 12, pp. 1173–1189, Dec. 2008, doi: 10.1016/j.apenergy.2008.03.003.
- [96] A. Bany Ata, F. Alobaid, C. Heinze, A. Almoslh, A. Sanfeliu, and B. Epple, "Comparison and validation of three process simulation programs during warm start-up procedure of a combined cycle power plant," *Energy Convers. Manag.*, vol. 207, p. 112547, 2020, doi: 10.1016/j.enconman.2020.112547.
- [97] M. Angerer, S. Kahlert, and H. Spliethoff, "Transient simulation and fatigue evaluation of fast gas turbine startups and shutdowns in a combined cycle plant with an innovative thermal buffer storage," *Energy*, vol. 130, pp. 246–257, Jul. 2017, doi: 10.1016/j.energy.2017.04.104.
- [98] N. J. Mertens, F. Alobaid, B. Epple, and H. G. Kim, "Combined-cycle start-up procedures: Dynamic simulation and measurement," in *Proceedings of the ASME 2016 Power Conference (POWER2016)*, 2016, doi: 10.1115/POWER2016-59286.
- [99] N. Mertens, F. Alobaid, T. Lanz, B. Epple, and H. G. Kim, "Dynamic simulation of a triple-pressure combined-cycle plant: Hot start-up and shutdown," *Fuel*, vol. 167, pp. 135–148, Mar. 2016, doi: 10.1016/j.fuel.2015.11.055.
- [100] W. A. K. Al-Maliki, F. Alobaid, V. Kez, and B. Epple, "Modelling and dynamic simulation of a parabolic trough power plant," *J. Process Control*, vol. 39, pp. 123–138, Mar. 2016, doi: 10.1016/j.jprocont.2016.01.002.
- [101] T. Henrion, K. Ponweiser, D. Band, and T. Telgen, "Dynamic simulation of a solar power plant steam generation system," *Simul. Model. Pract. Theory*, vol. 33, pp. 2–17, Apr. 2013, doi: 10.1016/j.simpat.2011.12.009.
- [102] W. A. K. Al-Maliki, F. Alobaid, R. Starkloff, V. Kez, and B. Epple, "Investigation on the dynamic behaviour of a parabolic trough power plant during strongly cloudy days," *Appl. Therm. Eng.*, vol. 99, pp. 114–132, Apr. 2016, doi: 10.1016/j.applthermaleng.2015.11.104.
- [103] F. Alobaid, *Numerical Simulation for Next Generation Thermal Power Plants*. Cham: Springer International Publishing, 2018.
- [104] J. A. A. Boure, A. E. E. Bergles, and L. S. S. Tong, "Review of two-phase flow instability," *Nucl. Eng. Des.*, vol. 25, no. 2, pp. 165–192, Jul. 1973, doi: 10.1016/0029-5493(73)90043-5.
- [105] H. Walter and B. Epple, *Numerical Simulation of Power Plants and Firing Systems*. Springer Verlag, 2017.
- [106] A. Temraz, F. Alobaid, T. Lanz, A. Elweteedy, and B. Epple, "Operational Flexibility of Two-Phase Flow Test Rig for Investigating the Dynamic Instabilities in Tube Boiling Systems," *Front. Energy Res.*, vol. 8, p. 222, Sep. 2020, doi: 10.3389/fenrg.2020.517740.
- [107] Y. Taitel and A. E. Dukler, "A model for predicting flow regime transitions in horizontal and near horizontal gas-liquid flow," *AIChE J.*, vol. 22, no. 1, pp. 47–55, Jan. 1976, doi: 10.1109/ICORR.2013.6650504.
- [108] L. E. O'Neill, "Experimental Investigation and Modeling of Key Design Parameters in Flow

Boiling and Condensation,” Purdue University, 2019.

- [109] S. Kakac and B. Bon, “A Review of two-phase flow dynamic instabilities in tube boiling systems,” *Int. J. Heat Mass Transf.*, vol. 51, no. 3–4, pp. 399–433, Feb. 2008, doi: 10.1016/j.ijheatmasstransfer.2007.09.026.
- [110] E. M. Chiapero, M. Fernandino, and C. A. Dorao, “Parametric study of the pressure characteristic curve in a boiling channel,” *Comput. Therm. Sci.*, vol. 3, no. 2, pp. 157–168, 2011, doi: 10.1615/ComputThermalScien.v3.i2.70.
- [111] L. C. Ruspini, C. P. Marcel, and A. Clause, “Two-phase flow instabilities: A review,” *Int. J. Heat Mass Transf.*, vol. 71, pp. 521–548, Apr. 2014, doi: 10.1016/j.ijheatmasstransfer.2013.12.047.
- [112] M. Ishii, “Thermally induced flow instabilities in two-phase mixtures in thermal equilibrium,” Georgia Institute of Technology, 1971.
- [113] G. Yadigaroglu and A. E. Bergles, “An experimental and theoretical study of density-wave phenomena oscillations in two-phase flow,” Cambridge, 1969.
- [114] A. K. Nayak and P. K. Vijayan, “Flow Instabilities in Boiling Two-Phase Natural Circulation Systems: A Review,” *Sci. Technol. Nucl. Install.*, vol. 2008, pp. 1–15, Jun. 2008, doi: 10.1155/2008/573192.